ACADEMIC
ACADEMIC PUBLISHING PTE LTD

Energy Storage and Conversion

https://ojs.acad-pub.com/index.php/esc

2024 VOLUME 2 ISSUE 3
ISSN: 3029-2778 (Online)

3

Editorial Team

Editor-in-Chief

Associate Editor

Editorial Board Members

Ahmed Al Salaymeh
The University of Jordan
Jordan

Shazia Hasan
Birla Institute of Technology & Science
United Arab Emirates

Hitesh Panchal
Gujarat Technological University
India

Hu Shi
Xi'an Jiaotong Univerisy
China

Wenxiu Que
Xi'an Jiaotong University
China

Arul Manuel Stephan
CSIR-Central Electrochemical Research Institute
India

Yunxiao Wang
University of Wollongong
Australia

Liang Li
Soochow University
China

Jun Wei Lim
Universiti Teknologi PETRONAS
Malaysia

Kriti Tyagi
CSIR-National Physical Laboratory
India

Hamid Reza Rahbari
DTU Construct
Denmark

Byoung-Suhk Kim
Jeonbuk National University
Korea

Ahmed Kadhim Hussein
University of Babylon
Iraq

Zhiyu Li
Shandong University of Technology
China

Masoud Darvish Ganji
Korea Institute of Ceramic Engineering and Technology
Korea

Dumitru Tsiulyanu
Technical University of Moldova
Moldova

Xiaohong Han
Zhejiang University
China

Wael Al-Kouz
University of North Alabama
USA

Mingzhe Yuan
Guangzhou Institute of Industrial Intelligence
China

Hesham A. Hegazi
German University in Cairo
Egypt

Jing Ding
Nanjing Technology University
China

Aman Bhardwaj
Regional Institute of Education
India

Florina Scarlatache
Technical University Gheorghe Asachi of Iasi
Romania

Ahmed Mezrhab
Université Mohammed Premier
Morocco

Muhammad Shahzad Nazir
Huaiyin Institute of Technology
China

Rahim Zahedi
University of Tehran
Iran

Yong Wang
Shanghai University
China

Volume 2 Issue 3 • 2024

Energy Storage and Conversion

Editor-in-Chief

Prof. Xiaohu Yang

Xi'an Jiaotong University, China

ACADEMIC
ACADEMIC PUBLISHING PTE LTD

2024 | Volume 2 | Issue 3

Energy Storage and Conversion

https://ojs.acad-pub.com/index.php/esc

Contents

Articles

Reviews

Energy Storage and Conversion 2024, 2(3), 1431.
https://doi.org/10.59400/esc.v2i3.1431

Article

Performance evaluation of dewatering systems for bio-digestate for developing countries

Ajay Kumar Jha[1,*], Sujan Jojiju[1], Hari Darlami[1], Bijay Basnet[2]

[1] Department of Mechanical and Aerospace Engineering, Pulchowk Campus, Institute of Engineering, Tribhuvan University, Kathmandu 44600, Nepal

[2] Department of Mechanical Engineering, Kathmandu University, Dhulikhel 45210, Nepal

*** Corresponding author:** Ajay Kumar Jha, ajaykumarjhaphd@gmail.com

CITATION

Jha AK, Jojiju S, Darlami H, Basnet B. Performance evaluation of dewatering systems for bio-digestate for developing countries. Energy Storage and Conversion. 2024; 2(3): 1431. https://doi.org/10.59400/esc.v2i3.1431

ARTICLE INFO

Received: 5 June 2024
Accepted: 8 July 2024
Available online: 19 July 2024

Abstract: The performance evaluation of a screw type dewatering system for bio-digestate in Nepal demonstrates significant potential for improving the usability and efficiency of bio-digestate as a fertilizer. Remarkable modifications in the previous include a 5 HP motor running at 1440 RPM with a gear reduction ratio of 1:40, a spring assembly system at the outlet, and a fine sieve. Testing and performance analysis at different operating speeds using a variable frequency drive revealed an optimal performance at 8 RPM, where the system achieved a liquid yield of 92.02% and an extraction efficiency of 73.12%. The installation cost of the machine was NPR 384,000, with a payback period of 2 years, six months, and two days. The internal rate of return (IRR) was calculated at 28.53%, while the net present value (NPV) was NPR 179,006.35. This study indicates that operating the dewatering system at lower speeds may improve efficiency and effectiveness in the dewatering process. This makes the machine a viable option for producing organic fertilizer and addressing Nepal's significant need for fertilizer.

Keywords: screw type dewatering system; bio-digestate; performance evaluation; liquid yield; extraction efficiency

1. Introduction

Anaerobic digestion of organic waste results in the production of biogas. Anaerobic digestion is the treatment method in which the waste with high organic content is breakdown to produce biogas [1]. The biogas plants are based on the phenomenon of biological decomposition of organic materials in the absence of air. For biogas production, main inputs are manure and sew bio digestate from biogas plants, a nutrient-dense residue, often requires dewatering to enhance its usability as a fertilizer by reducing moisture content. This process ensures improved handling, transportation, and effective application in agricultural practices. The slurry from biogas plants, rich in moisture content, poses challenges in handling, management, and transportation. In this research, a SolidWorks-designed screw-type dewatering system is employed to extract liquid from the slurry· making it viable for commercial use. Testing and performance analysis are conducted at different operating speeds using a variable frequency drive. The evaluation indicates a production capacity of 79.9 kg/h for the dewatering system, with liquid yield, extraction efficiency, and extraction loss at 92.02%, 73.12%, and 27.60%, respectively age, straw, households and industrial organic waste, maize and grass silage. The byproduct of the biogas plant is called slurry which can be used as a high nutrient fertilizer [2]. Biogas slurry has high water content of almost 90%, which arises the concern of dewatering and drying before using in agriculture.

According to WECS 2021, Nepal has built 433,173 small-scale and 343 large-scale biogas plants across the nation [3]. The Terai region of Nepal has the largest share of 51.99% of the installed domestic biogas plant and Bagmati province has the highest installed share of 25.88%. The fifteen periodic plans of the Government of Nepal have targeted to install further 200,000 domestic biogas plants and 500 large size biogas plant [4]. These biogas systems have the potential to generate a significant amount of nutrient-rich slurry. The valuable nutrients in the slurry can greatly benefit crop growth without harming the environment [5]. Moreover, using slurry can reduce the need for costly imported fertilizers, contributing to the profitability of the agricultural sector. By incorporating slurry into farming practices, biogas technology becomes a sustainable source of rural energy. This not only saves traditional fuel resources but also decreases the reliance on chemical fertilizers, thereby having a positive impact on agriculture.

The application of biogas slurry as a fertilizer offers significant environmental benefits, particularly in reducing greenhouse gas emissions. By capturing methane during the anaerobic digestion process and converting it to biogas, the potential release of methane—a potent greenhouse gas—is significantly reduced. Additionally, biogas slurry reduces dependence on synthetic fertilizers, which are energy-intensive to produce and often result in the emission of nitrous oxide, another potent greenhouse gas. The organic matter in biogas slurry can also enhance soil carbon sequestration, further reducing atmospheric carbon dioxide levels. Beyond mitigating greenhouse gas emissions, biogas slurry improves soil health due to its rich content of essential nutrients such as nitrogen, phosphorus, and potassium, which are vital for crop growth. Its application enhances soil fertility, leading to better crop yields. The organic matter in the slurry improves soil structure, increasing its water retention capacity and reducing erosion. Moreover, the addition of organic material from the slurry stimulates microbial activity in the soil, promoting nutrient cycling and overall soil health.

Furthermore, using biogas slurry as a fertilizer can significantly reduce water pollution caused by runoff from synthetic fertilizers. The organic nature of the slurry ensures a slower release of nutrients, reducing the risk of nutrient leaching into water bodies and preventing eutrophication. This combination of environmental benefits makes biogas slurry an effective and sustainable alternative to synthetic fertilizers, supporting both agricultural productivity and environmental conservation [6].

Dewatering is the treatment process to reduce the moisture content in the slurry output [7]. Dewatered slurry can be handled as. a solid material, rather than as a liquid material, and hence can be easily transported, stored, managed and used. Among various dewatering technologies such as centrifugal press, belt filter, screw press dewatering technology is widely used for high and low concentration sludge. The dewatering technology separates the moisture content in the slurry and hence improves the utilization of the bio slurry along with making it commercially viable as the organic fertilizer. The advantages of dewatering of the slurry are: dewatering decreases the volume, lowers the storage and the transportation cost; produces a material which helps in composting; and removes ponding and runoff [8].

The slurry generated from biogas plants poses a formidable challenge due to its inherently high moisture content, complicating its handling, management, and transportation. The current limitations in dewatering technology constrain the utilization of slurry to the immediate vicinity of the biogas plant, contributing to a degradation in its overall quality even within this constrained scope. Notably, the absence of efficient dewatering methods necessitates resorting to traditional approaches, characterized by prolonged processing times and a demand for substantial storage space. Consequently, these drawbacks render the slurry impractical for commercial applications, underscoring the pressing need for advancements in dewatering technologies to enhance the viability and utility of biogas plant by-products. The aim of this research is to conduct performance evaluation of screw type dewatering system for bio-digestate.

Limitations

The study focuses on dewatering and slurry obtained from anaerobic digestion of organic waste. It does not consider the effect and segregation of inorganic waste like plastics, glass etc. in the biogas digester.

2. Literature review

2.1. Biogas slurry

Biogas slurry, the byproduct of anaerobic digestion in a biogas plant, is a nutrient-rich organic fertilizer with around 93% water and 7% dry matter. The dry matter consists of 4.5% organic and 2.5% inorganic content [9]. It contains phosphorus, potassium, zinc, iron, manganese, copper, 1.6% nitrogen,1.55% phosphorous, and 1.00% potassium [10]. When combined with organic fertilizers, the slurry enhances the carbon/nitrogen ratio, resulting in increased yields of cotton, wheat, maize, and rice by 6.5%, 8.9%, 15.2%, and 15.9%, respectively [9]. Biogas slurry serves as an environmentally safe organic fertilizer, producing macro and micro nutrients while having lower levels of heavy metals compared to synthetic fertilizers. It can reduce chemical fertilizer use by 15% to 25%, promoting bio-pesticide activities, beneficial microbe growth, biochemical levels in plants, and maintaining soil physio-chemical properties, ultimately improving plant health.

2.2. Dewatering technology

Dewatering technology is essential for enhancing the utility and commercial viability of bio slurry as organic fertilizer. By effectively reducing moisture content, it significantly decreases the volume of the slurry, leading to lowered storage and transportation costs. This process also facilitates composting, contributing to the organic fertilizer’s effectiveness. Additionally, dewatering eliminates ponding and runoff issues, creating a more sustainable approach. It optimizes the air-drying process, ensuring the bio slurry achieves an ideal consistency for efficient utilization as organic fertilizer. These advantages highlight the importance of incorporating dewatering technology into our processes, aligning with our commitment to cost-effectiveness, environmental sustainability, and optimized resource utilization.

2.3. Types of dewatering technology [11]

Dewatering methods for slurry can be categorized into natural and mechanical approaches, each offering unique advantages. Natural dewatering relies on gravity settling and porous surfaces, as seen in sludge drying beds where liquid evaporates gradually. Mechanical dehydration, on the other hand, uses machinery and processes to remove moisture efficiently. This includes the use of centrifugal presses, which employ centrifugal force to separate moisture from the slurry, enhancing the drying process. Belt filter presses utilize continuous filtration with a belt, effectively removing moisture from the slurry. Rotary drum filters leverage rotation to separate moisture, setting the stage for subsequent drying processes. These methods improve the dewatering efficiency of slurry, leading to better drying outcomes and increased utility as organic fertilizer. **Table 1** shows the comparison of six different types of dewatering system based on various criteria.

Table 1. Comparison of different types of dewatering system [12].

Type	**Cake dryness**	**Solid recovery**	**Process/drying time**	**Operating cost**	**Capital cost**	**Chemical**
	% solid	% solid capture	Time (measurement)			Usage
Vacuum filters	16–45	85–95	Fast (minutes or hours)	High	Moderate	Moderate
Filter presses	40–60	80–95	Very fast (minutes or months)	High	High	High
Centrifugal press	20–35	85–90	Fast (minutes or hour)	Moderate	Low	High
Drying beds	25–60	90–100	Slow (weeks or months)	Very low	Low	Low
Sludge lagoons	20–40	90–100	Very slow (months or years)	None	Very low	None
Gravity/low pressure	10–50	90–96	Moderate (days or weeks)	Low	Moderate	

2.4. Selection of dewatering technology

The characteristics of the dewatering technology vary according to different attributes such as cake dryness, solid recovery, drying time, operating cost, maintenance required, and so on. The comparison of different dewatering technologies is mentioned in. **Figure 1** shows the comparison of various artificial technologies on the basis of total solid content.

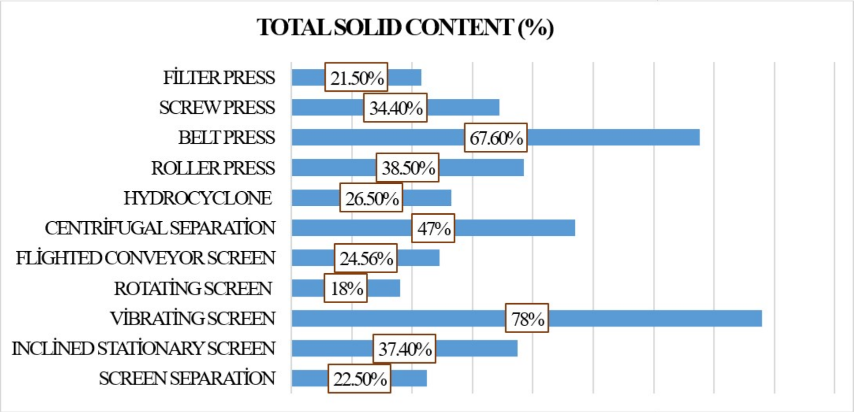

Figure 1. Comparison of different dewatering technologies.

Screw presses are adept at effective dewatering, making them suitable for a variety of production processes where the separation of particles from liquids is crucial [13]. These dewatering devices consume less energy compared to alternative types, resulting in reduced overall operating costs over their lifespan [14]. Screw press technology is advantageous for sludge dewatering in comparison with others for the following reasons**.** Recent advancements in screw press technology have significantly improved efficiency, surpassing their earlier counterparts. These modern screw presses excel in the dewatering of sludge with elevated solids content, leading to the formation of a more concentrated sludge cake and a substantial volume reduction. This heightened efficiency directly translates into cost savings for wastewater treatment plants. Moreover, the operational expenses associated with screw press technology are notably reduced compared to centrifuges, as it requires less energy and produces minimal noise and vibration. This diminished operational impact reduces the need for additional measures such as soundproofing and vibration isolation. Notably, screw presses can achieve higher solids content in dewatered sludge compared to centrifuges, resulting in a more concentrated sludge cake and a decreased volume of waste for disposal. Furthermore, the lower number of moving parts in screw presses translates to lower maintenance requirements compared to centrifuges [15].

Table 2 shows the performed structural and computational fluid dynamics simulation for different type of screws for screw press technology.

Table 2. Comparison of different types of screw.

Types of screw and shaft	**Deformation (mm)**	**Equivalent stress (MPa)**		**Equivalent strain (mm/mm)**	
	Max	**Max**	**Min**	**Max**	**Min**
Constant pitch screw with straight shaft	0.2129	46.19	0.0046493	0.00024385	3.6288×10^{-8}
Variable pitch screw with straight shaft	0.21344	45.035	0.0083044	0.00022607	7.1824×10^{-8}
Constant pitch screw with tapered shaft	0.17151	43.941	0.0259	0.00022244	4.1637×10^{-7}
Variable pitch screw with tapered shaft	0.17116	46.285	0.048465	0.00023649	3.1202×10^{-7}

According to the findings, the constant pitch screw with the tapered shaft shows the least amount of distortion, indicating that it has better structural integrity overall.

3. Materials and methodology

A comprehensive and well-structured methodology was developed, covering all essential steps for the study. The research commenced with a review of existing literature and assessments, followed by the design and modeling of the technology. The detailed sequence of the methodology is depicted with a **Figure 2**.

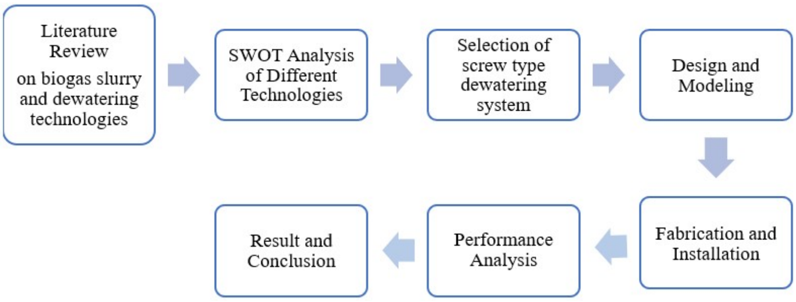

Figure 2. Methodological flowchart.

3.1. Design and modeling

Detail design and drawing of dewatering technology considering the size of the biogas plant, byproduct of the biogas plant, waste input in the biogas plant, proportion of organic waste, etc. was done in this phase. The drawing of plant layout and schematic drawing indicating different parts of the dewatering system and their specifications was developed in this phase. The rough specification for the dewatering technology for the biogas plant is indicated in **Table 3**.

Table 3. Rough specification for the dewatering system.

S.N.	Parameter	Specification
1	Name	Dewatering system
2	Application	Organic waste dewatering work
3	Feed capacity	0.5 to 1 ton/day
5	Mechanism	Belt filter press rotary drum filter, screw press
6	Electric motor	Chopper: 2 kW, squeezer: 5kW
7	Chopper type	Multi blade/double screw
8	Squeezer type	Single conical
9	Screen type	Perforated
10	Screen size	2 mm
11	Material used	Mild steel

The screw-type dewatering system was designed using SolidWorks, employing its advanced features for precise modeling. This facilitated the creation of a detailed and optimized representation of the machine’s structure as shown in **Table 4**.

After the assembly simulation was performed to test the performance and reliability of the system in different load and performance conditions.

The **Figure 3** is the conceptual design of the dewatering system that was designed in SolidWorks software and **Figure 4** shows the detailed design of the system.

Table 4. Modelling of parts.

Modeled part	Description
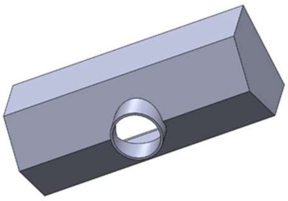	**Collector** After the water has been sorted from the solids that have been dried, it is collected by a collector. It guarantees effective drainage and makes water removal easier. Design and placement of the collector are essential for efficient water and output products management.

Table 4. (*Continued*).

Modeled part	Description
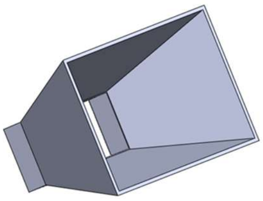	**Hopper** A hopper is where material that is fed into a machine. Upon entering the hopper, the material is directed toward the machine's screw. It is an essential component since it makes loading efficient.
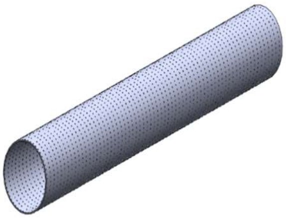	**Sieve** A sieve or screen is used to separate the particles from the liquids during the dewatering stage of a screw press machine. With the help of a wire mesh, the sieve is designed to capture solid particles while allowing water to pass through it. The design of the model is presented here in the figure.
	**Frame** The frame of a screw press machine provides a sturdy structure to hold the numerous components of the machine and withstand the stresses generated during use. The frame is typically built out of steel or other robust materials that are strong, resilient, and deformation-resistant.
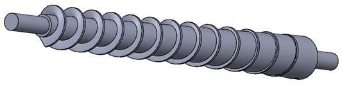	**Screw** A screw featuring a constant pitch and a gradually tapering shaft ensures uniform thread spacing. With the capacity to handle fluctuating flow rates and efficiently transport materials from one end to the other, this design enhances the conveyance of materials.
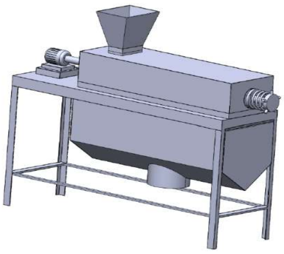	**Assembled final model** Figure here shows the final model with all the individual components assembled into a single and complete model. It mainly represents the visual form of real machine used as dewatering system.

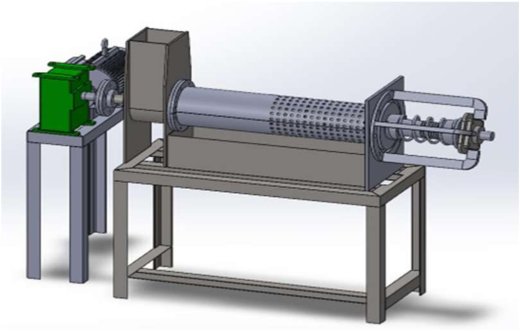

Figure 3. Conceptual model of the system.

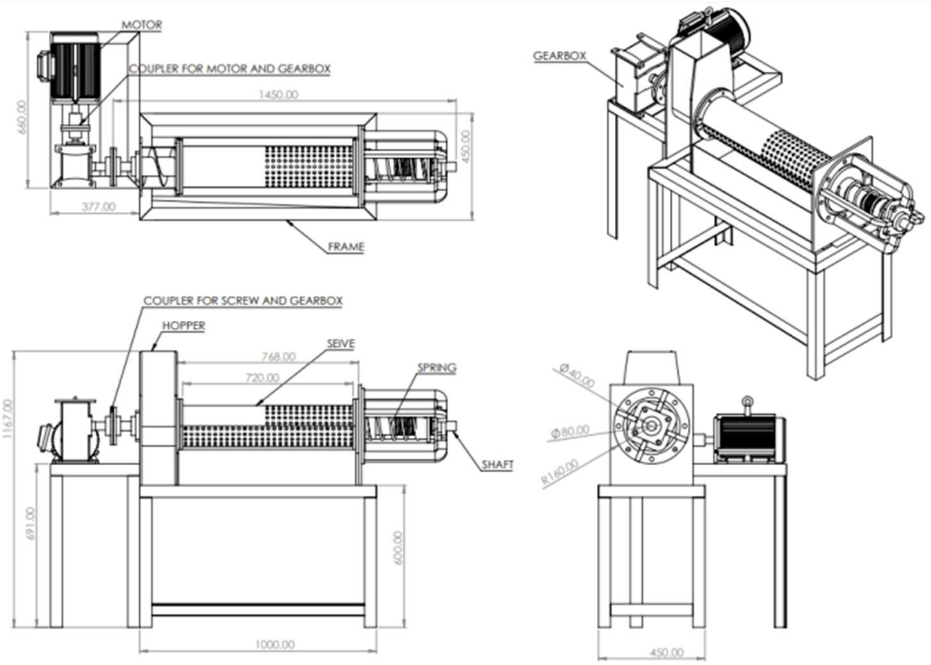

Figure 4. Detailed design of the system.

Table 5 shows the detailed design and formula for designing the system.

Table 5. Detailed design.

Power requirement	
To Overcome the inertia of shaft and screw	• The volume of hollow tapered cylinder section; volume, $V = \pi r^2 l$ • The net volume of flight $V_{\text{net}} = \text{volume of flights} - \text{Volume of hollow shaft}$ • Power to overcome this mass = Weight × Mean Peripheral velocity (v_m) • $v_m = T_m \times N/60$ where, T_m is the mean lead of the screw, and N is the rpm of the screw.
Convey the biogas effluent slurry	• capacity of the screw press is $Q\left(\frac{kg}{hr}\right) = 15\pi d^2 t_m N \psi \rho_{S1} c$ [16] D = screw diameter (160 mm) t_m = screw lead (69 mm) N = rotational speed (10 rpm) c = correction factor based on the angle of inclination (0.7), ψ = filling coefficient of the screw cross section (0.125 for high abrasive materials) ρ_{S1} = density of biogas slurry (1100 kg/m^3) Power required to convey the slurry is $P_2 = \frac{QL\rho_{S1}F_{mt}}{168547}$ [17] where, Q is the conveying capacity L is the projected length of the screw conveyor (0.92 m) F_{mt} is the material factor per Kw.
To press and separate slurry	• Power to separate slurry, $P = FV_m$ where, F = Force required to separate the slurry V_m = Mean velocity F = Pressure × Total surface area $V_m = t_m N/60$ where t_m is pitch of the screw
To overcome friction and other losses	• Frictional force, $F = \mu \times N_{fr} = 0.35 \times 31.0068 \times \cos 30 = 9.3984$ kN Considering other losses as 10% of frictional loss, then $P_4 = 0.10808 \times 1.1 = 0.11888$ kW
Overall power required	• $P = P_1 + P_2 + P_3 + P_4$ $P = 1.13128hp$

3.1.1. Power required to overcome the inertia of the shaft and screw

The design of the shaft is tapered and it is a hollow shaft. The **Figure 5** is the drawing of the screw with dimensions.

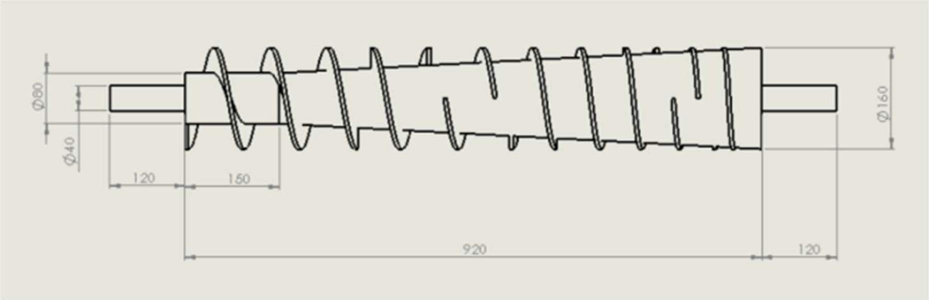

Figure 5. Dimension of screw press.

The assessment outlines the calculations for the mass and power requirements of a hollow tapered shaft within a screw press system. The total volume and mass of the shaft and flights were calculated to assess the system's weight. Combined, they amount to a total mass of approximately 34.526 kg. Using this mass, and accounting for the mean peripheral velocity, the power required to overcome the system's weight was estimated to be about 0.0039 kW. This power requirement is crucial for ensuring the efficient operation of the screw press.

3.1.2. Power required to convey the biogas effluent slurry

The analysis focuses on the power required to convey biogas effluent slurry using a screw press system. The throughput capacity of the screw press is determined by factors such as screw diameter, screw lead, rotational speed, and the density of the biogas slurry. The system's capacity was calculated to be approximately 79.9 kg/h. The power needed to convey the slurry is estimated based on the conveying capacity, the projected length of the screw conveyor, and other factors such as material factor and density. This leads to a calculated power requirement of around 0.29 kW. In summary, the analysis identifies the necessary power to effectively convey the biogas slurry through the screw press system, ensuring efficient operation. The low power requirement demonstrates the system's efficiency in managing the biogas effluent slurry.

3.1.3. Power required to press and separate slurry

The optimum pressure to separate biogas effluent slurry into solid and liquid constituents is approximately 1.74 MPa [18]. The examination focuses on the power required to press and separate biogas effluent slurry using a screw press system. The optimum pressure for separation is around 1.74 MPa, but the analysis uses 60% of the optimum, equating to 0.696 MPa. The force required to separate the slurry is calculated as the product of the compression pressure and the total effective area of 0.04455 m^2, resulting in a total force of approximately 31.01 kN. The mean velocity of the screw press is calculated using the screw pitch and rotational speed, resulting in a mean velocity of 0.0115 m/s. The power required to press and separate the slurry is then calculated as the product of the force and mean velocity, leading to a power requirement of approximately 0.36 kW. This power estimation is crucial for the efficient operation of the screw press in separating biogas effluent slurry into its solid and liquid constituents. Ensuring the system operates within this power range will facilitate the effective separation process and contribute to optimal system performance.

3.1.4. Overall power required

Therefore, the power of the motor shall be greater than 1.13128 hp i.e., 2 horsepower electric motor is considered. The evaluation assesses the power required to overcome friction and other losses in a screw press system. The frictional force is calculated using the friction coefficient, resulting in approximately 9.4 kN. The power needed to overcome this friction is calculated to be 0.10808 kW. Accounting for other losses (10% of frictional loss), the total power required increases to 0.11888 kW. The overall power required for the screw press operation is calculated as the sum of the power required for mass, slurry conveyance, pressing and separating slurry, and frictional losses, totaling 0.7672232 kW (1.02844 hp). Including a 10% additional compensation for safety, the final power requirement is approximately 1.13 hp. Therefore, a motor with a rating of at least 2 horsepower is recommended to ensure efficient and reliable operation of the screw press system.

3.2. Fabrication and installation

Based on the specifications developed, a bill of quantities of goods and accessories was prepared and hence goods available within the country and outside the country were procured by proper channels during this phase. While procuring the goods, the quality of the accessories was checked to verify that they match the specifications developed along with after-sales service of the accessories. **Table 6** shows the list of fabricated components that are used to fabricate dewatering system.

Table 6. List of fabricated components.

S.N.	Fabricated parts/components
1	Screw (Constant pitch, tapered shaft)
2	Sieve and cage
3	Covering
4	Stand/frame
5	Collector
6	Gearbox

The various technologies that were fabricated are dewatering technology as well as coupling system. The fabrication/installation was done with standard processes and procedures in the workshop at the Pulchowk campus, IOE, Nepal as shown in **Figure 6**.

Figure 6. Fabrication of system.

Some of the parts such as motor and pump required for the operation were purchased and integrated to the system. The system as a whole is integrated of different sub systems and components. Each system and component have their own function, so they were fabricated separately and assembled together.

The assembly of these part was carried out to get the fully functioning plant. The fabricated system is connected to a currently operating biogas plant. The outputs of the dewatering system i.e., dry slurry was evaluated. The dewatering technology was rigorously tested for strength and weakness in various parts. The weak part of the system had to be replaced so that the technology can perform reliably and durably throughout its lifetime.

3.3. Performance analysis

First the power requirement for the operation of the plant considering all the forces and inertia that come into play during operation was calculated. This included power required to overcome the inertia of the shaft and screw, power required to convey the biogas effluent slurry, power required to press and separate slurry, power required to overcome friction and other losses and overall power required.

Physical and chemical parameters associated with the dry, wet slurry, and liquid discharge have been evaluated, and based on that the effectiveness of the system has been determined. The various parameters associated with the dewatering plant such as liquid yield, liquid discharge, extraction efficiency, extraction loss, and liquid extracted was evaluated.

4. Results and discussion

The evaluation of the machine was carried out using the expression given below:

$$L_y = \frac{100 \times W_{le}\%}{W_{le} + W_{rw}}$$

$$L_e = \frac{100 \times W_{le}\%}{x\, W_{fs}}$$

$$E_1 = \frac{100 \times \left[W_{fs} - (W_{le} + W_{rw})\%\right]}{W_{fs}}$$

where,

W_{le} = liquid extracted (in kg)
W_{rw} = residual liquid in output cake (in kg)
W_{fs} = feed sample (in kg)
L_y = liquid yield (%)
L_e = extraction efficiency (%)
E_1 = extraction loss (%).

Table 7 shows the result of the test carried out on the dewatering system.

Table 7. Test results.

Test No.	Feed sample W_{fs} (kg)	RPM	Weight of cake W_c (kg)	Liquid extracted W_{le} (kg)	Weight of liquid in cake W_{rw} (kg)
1	10	36	1.82	6.1	1.14
2	10	25	1.76	6.37	0.92
3	10	18	1.61	6.48	0.84
4	10	12	1.38	6.61	0.74
5	10	10	1.25	6.69	0.68
6	10	8	1.12	6.8	0.59

4.1. Performance analysis

From the plant, the performance analysis was done by taking different parameters under consideration. At the different speed (RPM), liquid yield, extraction efficiency and extraction loss are calculated. The data of the weight of cake, weight of liquid in cake, and liquid extracted was taken from the table above. The biogas slurry samples, after undergoing a pre-treatment process of sun-drying for 24 h, have been subjected to dewatering, with an initial weight of 10 kg consistently maintained for feeding at machine. As the RPM settings decreases from 36 to 8, several key trends emerge which are listed in the **Table 8**.

Table 8. Performance analysis.

Test No.	RPM	Liquid yield, L_y (%)	Extraction efficiency, L_e (%)	Extraction loss E_1 (%)
1	36	84.25	65.59	27.60
2	25	87.38	68.49	27.10
3	18	88.52	69.68	26.80
4	12	89.93	71.08	26.50
5	10	90.77	71.94	26.30
6	8	92.02	73.12	26.10

It shows that as the speed decreases the Liquid yield percentage increases, along with the extraction efficiency. The value of extraction efficiency reaches a maximum value of 73.12% at 8 RPM. Further, the value of extraction loss decreases as we decrease the speed. This shows the lower RPM setting increases the overall efficiency of the plant.

4.1.1. Liquid yield

As shown in the **Figure 7**, the liquid yield decreased with the increase in the speed of the shaft. The highest liquid yield was observed to be 92.16% at 8 rpm whereas the lowest liquid yield was 87.02% at 36 rpm. The decrease in liquid yield with increase in rpm is due to the result of splashing liquid to the wall of the machine.

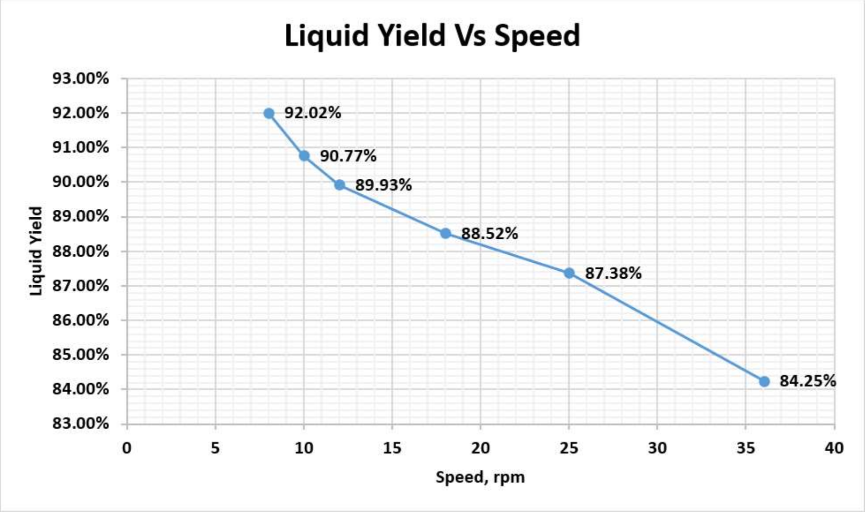

Figure 7. Liquid yield.

4.1.2. Extraction efficiency

The extraction efficiency of the dewatering system decreased with the increase in the speed of the shaft. The highest extraction efficiency was observed to be 73.12% at 8 rpm whereas the lowest 65.59% was observed at 36 rpm. As shown in **Figure 8.** It is evident that extraction efficiency is greater at a low RPM setting.

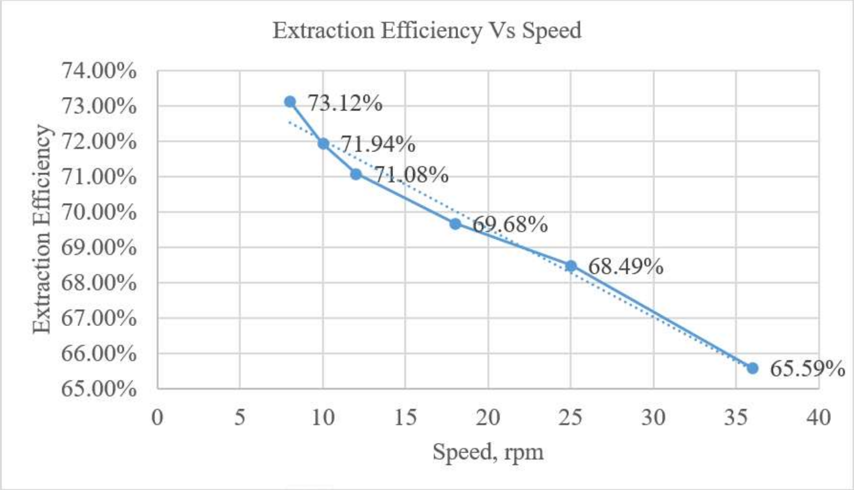

Figure 8. Extraction efficiency.

4.1.3. Extraction loss

The extraction loss has increased with the increase of speed. The highest loss was found to be 27.60% at 36 rpm whereas the lowest was 26.10% at 8 rpm as shown in **Figure 9**. The graph shows the trend between Extraction loss and speed (rpm). The extraction loss increased with the increase in speed, which indicates that once speed increases, the slurry moves fast and vibration occurs.

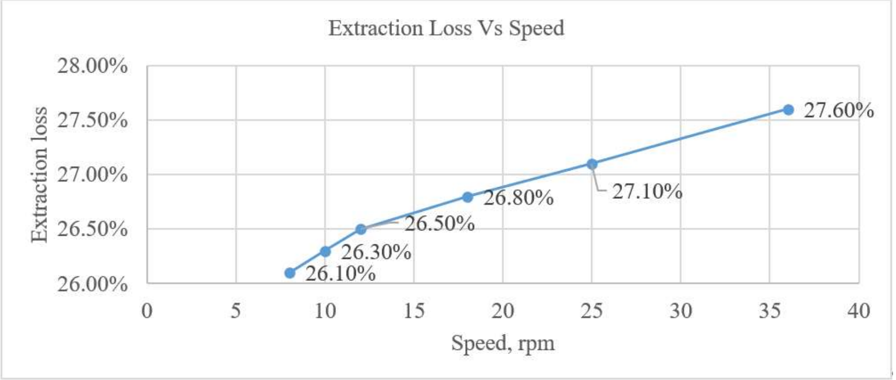

Figure 9. Extraction loss.

4.2. Financial analysis

The cost of the dewatering machine for the consumer will be NRs 384,000. Three laborers will be required for operating the machine and packing the fertilizer, with a monthly wage of NRs 19,000 per laborer, including salary and benefits. This sums up to a total annual labor cost of NRs 684,000. Assuming the dewatering machine operates for 300 days annually, the operation of the machine involves a 5 HP motor and a 1 HP slurry pump, running for 7 h per day. The cost of electricity for operating the machine is estimated to be NRs 93,958.2 annually. Additionally, the annual maintenance cost of the dewatering machine is assumed to be 10% of the total cost, amounting to NRs 38,400 as shown in **Table 9**.

Table 9. Cash flow.

S. No.	Cash flow (annual)	Amount (NRs)
1	Initial cost	384,000
2	Operating cost	93,958.2
3	Labor cost	684,000
4	Maintenance cost	38,400
5	Interest @ 10% annually	38,400
6	Income	1,008,000

If we consider a biogas plant of 30 m^3, then the output of the plant would be 1200 kg/day. The compression ratio of the machine by weight is 7, then the output will be 171 kg per day. With the efficiency of 70% the output per day will be 120 kg per day. Market value of 1 kg organic fertilizer is Rs 25.

The payback period is the required number of years to gain the original capital where annual income = 1,008,000.

Annual expenses = Operating cost + Labor cost + Maintenance cost + Annual interest on investment = 93,958.2 + 68,4000 + 38,400 + 38,400 = 854,758.2

Now,

$$\text{Net annual profit} = \text{Net annual income} - \text{Annual expenses} = 1{,}008{,}000 - 854{,}758.2 = 153{,}241.8$$

Therefore,

$$\text{Payback period} = \frac{\text{Investment}}{\text{Annual profit}} = \frac{384{,}000}{153{,}241.8} = 2.505844\ \text{years}$$
$$= 2\ \text{years}\ 6\ \text{month}\ 2\ \text{days}$$

5. Conclusion

The study assessed a screw-type dewatering system for biogas digestate to improve the commercial viability of bio slurry as an organic fertilizer. The system showed a production capacity of 79.9 kg/h, with a liquid yield of 92.02%, extraction efficiency of 73.12%, and extraction loss of 27.60%. Results from the study demonstrated that as the speed of the screw decreased, the overall efficiency of the dewatering system increased. Lower RPM settings resulted in higher liquid yield and extraction efficiency, while reducing extraction loss. The optimal performance was observed at 8 RPM, providing the highest extraction efficiency and lowest extraction loss.

In conclusion, the screw-type dewatering system shows promising potential for enhancing the utility and commercial viability of bio slurry as an organic fertilizer. By effectively reducing the moisture content in biogas digestate, the system can improve handling, storage, and transportation, making bio slurry more accessible for agricultural use. The study's findings suggest that implementing this technology in biogas plants could offer significant environmental and economic benefits, supporting sustainable energy and agricultural practices.

Author contributions: Conceptualization, AKJ and SJ; methodology, HD; software, BB; validation, AKJ, HD and SJ; formal analysis, BB; data curation, BB; writing—original draft preparation, BB; writing—review and editing, BB; supervision, AKJ and BB; funding acquisition, AKJ and HD. All authors have read and agreed to the published version of the manuscript.

Funding: The authors would like to thank University Grant Commission, Bhaktapur, Nepal for granting us with Faculty Research Grant (Award No. FRG-78/79- Engg-01) along with providing the necessary fund for this study. The authors would also like to thank Energize Nepal and Center for Pollution Studies (CPS), Institute of Engineering, Lalitpur, Nepal for providing the necessary supports.

Conflict of interest: The authors declare no conflict of interest.

Abbreviations

WECS	Water and Energy Commission Secretariat
CPS	Center for Pollution Studies
kW	Kilowatt

kN	Kilonewton
NPC	National Planning Commission
IOE	Institute of Engineering
RPM	Revolutions per minute

References

1. Gregor DZ, Viktor G. Anaerobic Treatment and Bio digestion from organic waste 2012. Available online: https://cdn.intechopen.com/pdfs/27154/InTech-Anaerobic_treatment_and_biogas_production_from_organic_waste.pdf (accessed on 7 May 2024).
2. Karunanithi A. System analysis of de-watering process for treating biogas digestate. Research Gate; 2014.
3. WECS. Nepal Energy Sector Synopsis Report 2022. WECS; 2022.
4. National Planning Commission. The Fifteenth Plan Fiscal Year. National Planning Commission; 2020.
5. Bonten L, Zwart K, Rietra R, et al. Bioslurry as a fertilizer. Research Gate; 2014.
6. Kabeyi MJB, Olanrewaju OA. Biogas Production and Applications in the Sustainable Energy Transition. Journal of Energy. 2022; 2022: 1–43. doi: 10.1155/2022/8750221
7. Mangone F, Ferreira J, Ferrari A, et al. Modelling and optimization of a geotextile dewatering tubes process. 28th European Symposium on Computer Aided Process Engineering. 2018; 1371–1376. doi: 10.1016/b978-0-444-64235-6.50240-0
8. Gateway Structure SDN BHD. What is Sludge Dewatering and Its Usages & Benefits. Available online: https://gssb.com.my/what-sludge-dewatering-usages-benefits (accessed on 7 May 2024).
9. Malav L, Kumar M, Khan SA, Kumar S. Biogas Slurry: Source of Nutrients for Eco-friendly Agriculture. Research Gate; 2015.
10. Karki AB. Country Report on the Use of Bio-slurry in Nepal. In: Bibalex. Netherlands Development Organisation; 2006.
11. Machinery L. Longzhong Machinery. Available online: https://www.lzzgchina.com/solutions/project-case/sludge-dewatering-methods.html#:~:text=There%20are%20various%20technologies%20for,presses%2C%20centrifuging%2C%20and%20geomembranes (accessed on 7 May 2024).
12. GlobalSpec. Dewatering Equipment Selection Guide. Available online: https://www.globalspec.com/learnmore/manufacturing_process_equipment/filtration_separation_products/dewatering_equipment. (accessed on 7 May 2024).
13. Ford M, Fleming R. Mechanical Solid-Liquid Separation of Livestock Manure. International Food Safety. 2002.
14. EPA U. Emerging Technologies for Biosolids Management. US EPA; 2006.
15. Australia WE. Advancement In Screw Press Technology And Advantages For Sludge Dewatering. Waterman Engineer Australia; 2023.
16. Okafor B. Development of Palm Oil Extraction System. Research Gate; 2015.
17. Yadav S, Jha AK, Darlami HB. Design and Improvement of Dewatering System Implemented for Biogas Slurry. International Journal for Multidisciplinary Research. 2023.
18. Mudryk K, Frączek J, Jewiarz M, et al. Analysis of Mechanical Dewatering of Digestate. Agricultural Engineering. 2016; 20(4): 157-166. doi: 10.1515/agriceng-2016-0073

Energy Storage and Conversion 2024, 2(3), 1515.
https://doi.org/10.59400/esc.v2i3.1515

Article

Optimal micro-pump-storage system for the average Greek hotel with PV generation

Dimitrios K. Kosmopoulos, Admitos A. Bideris-Davos, Panagis N. Vovos*

Laboratory of Power Systems, Renewable and Distributed Generation, Department of Electrical and Computer Engineering, University of Patras, 26504 Rion, Greece

*** Corresponding author:** Panagis N. Vovos, panagis@upatras.gr

CITATION

Kosmopoulos DK, Bideris-Davos AA, Vovos PN. Optimal micro-pump-storage system for the average Greek hotel with PV generation. Energy Storage and Conversion. 2024; 2(3): 1515. https://doi.org/10.59400/esc.v2i3.1515

ARTICLE INFO

Received: 10 July 2024
Accepted: 14 August 2024
Available online: 5 September 2024

Abstract: In this paper, a modern micro-scale pumped hydro storage system that is specifically designed to operate in coordination with photovoltaics installed at the roof of an average Greek hotel is presented. The fictitious hotel chosen as a case study, displays the energy profile of an average sea-side hotel around the Mediterranean Sea, while photovoltaics' energy generation is assumed to follow the typical production profile of such sites. Pumped hydro storage and photovoltaic generation, size and cost have been appropriately modeled so that they realistically simulate their operational scheme, while also considering the spatial and technical characteristics and limitations of such projects. Results derived from the implementation of such a scheme into the Average Greek hotel demonstrated significant monetary benefits, accompanied with a substantial net annual profit and low payback period of the investment.

Keywords: pumped storage hydropower; pump as turbine; photovoltaics; renewable energy sources; average Greek hotel; levelized cost of energy; payback period

1. Introduction

Significant steps have already been taken in the last decades in the direction of developing RES as a replacement for energy production from fossil fuels. Even though fossil fuels are responsible for air pollution and greenhouse gas emissions, a substantial part of the total production still relies on them. This is because RES, such as wind power and photovoltaics, depend on the prevailing weather conditions, the time of the day and the season of the year. These elements render RES highly associated with uncertainty and unpredictability. These two major disadvantages of RES for the generation of electricity could be mitigated with storage, working as a buffer for generation-load imbalances: excess RES generation could be stored for consumption at a later time when demand is higher than generation. However, storage is still quite expensive [1], making conventional power plants still necessary for power balancing and for ensuring stability and reliability in the grid.

The necessity of energy storage is imperative in order to increase the level of independence of power systems from fossil fuels through the higher penetration of RES. The global pumped storage hydropower capacity increased by more than 30% in roughly a decade, from some 100 gigawatts in 2010 to more than 139.9 gigawatts in 2023, accounting for 90% of total electrical energy storage capacity. Pure pumped storage hydropower capacity worldwide from 2010 to 2023 [2,3]. These systems aim to overcome the problems deriving from the further penetration of RES to the power system, as effectively as possible. However, small-scale energy storage is dominated by batteries. Their modularity allows them to reach significant capacity (in the order of tens of MWh) at a lower total initial cost, mainly because PHS systems of the same scale still face spatial limitations and immense civil-work costs. However, even if the development of battery storage has made significant steps, their cost per kWh is at least 3 times greater than PHS [4]. Indeed, according to Li et al. [5], the LCOS of batteries typically ranges between 30 and 40 US$/kWh, while Smallbone et al. [6] reports that LCOS for PHS is estimated between 10 and 15 US$/kWh. Furthermore, there is still an ongoing debate whether batteries are environmentally safe or really recyclable at a reasonable cost [7,8]. Additionally, unlike batteries, the number of cycles of charging and discharging for PHS, does not shorten its operational lifespan of the system or impact its efficiency [9]. Finally, there are concerns regarding the future availability of raw materials that are used during the manufacturing of batteries and the impact of rising prices on battery production costs [8].

The most common turbine technology employed in pico-hydro projects is the pump used as turbine (PAT), mainly due to its low purchase cost resulting from the wide commercial availability of pumps (wide variety between 1.7 kW and 160 kW range). According to Bideris Davos and Vovos [10], the purchase cost of PATs is on average 5 times lower than conventional turbines, and only tends to become comparable (2 times lower) for outputs greater than 40 kW. However, PAT technology is not as well documented as turbines, the determination of their BEP when operating as turbines still presents a major challenge.

PATs are effective mainly when used in locations with controllable water flow variation [11] since they do not possess an adjustable guide vane mechanism and thus their adaptability in fluctuating flow rates and head is rather limited. In practice, in order to improve their operational flexibility the combined employment of hydraulic and electrical regulation is required [12]. Pérez-Sánchez et al. [13] performed a thorough review regarding the various empirical methods employed to predict the BEP of a PAT and proposed an improved approach to both BEP prediction and the construction of the characteristic curves. A numerical model to predict the BEP of PATs when the actual pump characteristics from catalogues are available is established in Barbarelli et al. [14]. The results demonstrated high accuracy when the detailed geometrical parameters of the pumps were provided. In the study of Venturini et al. [15], a physics-based simulation model was developed that utilizes the performance curve of pumps in order to predict the performance curves of PATs. In Pugliese and Giugni [12], an operative framework is developed under which the preliminary selection of PATs from a manufacturer's database is optimized in terms of energy production and payback periods. Fecarotta and McNabola [16] and Nguyen et al. [17] aim at the optimal location of PATs. However, they simulate them as simple head losses rather than real machines and disregard their feasible region by assuming constant efficiency. Finally, they ignore the rotational speed variations that fluctuating operating conditions create on the runner.

Very few micro-scale PHS systems have been implemented. They can be found in commercial and residential buildings. In combination with a renewable energy source, they are used to store the excess of generated electrical energy and return it back to the consumption later, when the RES cannot cover the demand.

The first completed micro-scale PHS system was constructed in the Goudemand apartment building complex in the Arras region of France, counting 240 apartments and housing approximately 700 people. At one of the buildings, 2.16 kWp of PV panels, 2 small vertical-axis wind turbines with a total power of 1000 W and a hybrid storage system consisting of a PHS system and a stack of lead-acid batteries have been installed [18]. When the electrical energy production from RES exceeds the energy demand, the excess energy charges the batteries. When the batteries are fully charged, pumping of water starts. Conversely, when the energy demand exceeds the production, batteries start providing energy to the building and when fully discharged, energy production from the PHS unit begins. The PHS system uses the 30-meter height of the building to store water in the appropriately sealed 60 m^3 upper reservoir placed on the roof. The lower reservoir is located in the building's basement consisting of 5 rectangular plastic tanks, 10 m^3 each. To pump water from the lower to the upper reservoir, a multistage 1.5 kW pump is installed, while for the energy production a Pelton 450 W turbine is used. The water flow supplying the turbine is regulated by an electric valve. The battery system operating in parallel with the PHS system, consists of 12 lead-acid battery cells with a total capacity of 2400 Ah. Although the useful energy capacity of 3.5 kWh for the hydroelectric system is considered small compared to the battery capacity (24 kWh), it is essential because it extends the batteries' lifespan by 1000 cycles.

Another completed micro-scale PHS system was implemented at the Negundo innovation center in the Froyennes area of Belgium. The energy supply to this facility is provided by PV panels with a total capacity of 110.2 kWp power and 4 wind turbines with a capacity of 2.4 kWp each. The installed PHS system uses an existing artificial 1500 m^3 basin, for collecting run-off water from roofs and roads, as the upper reservoir. An underground tank with a capacity of 650 m^3, located near the buildings is used as the lower reservoir. These 2 reservoirs are connected through a piping system with a total length of 80 m and an internal diameter of 335 mm. Between the upper and the lower reservoir, a pump with a variable frequency drive is installed, which also functions as a turbine (PAT) and is able to generate a maximum of 7 kW of power [19].

Other implementations of micro-scale PHS systems can be found in some remote areas and villages, which are not connected to the main grid. In such cases, the primary energy sources are PV parks or small wind turbines. Their possible excess energy is stored by the PHS system and returned to the consumers when power demand exceeds production. An example of such as system is described below.

A micro-scale PHS system, combined with PVs and batteries, has been constructed in the isolated village of Mersina on Donoussa Island, Greece. This remote village is not connected to the grid which supplies the rest of the island. The main purpose of this system is to provide uninterrupted power supply to the 13 houses of the village, covering the basic electricity needs of the residents: lighting, TVs and refrigerators. The system is powered by 18 kWp of PV panels. Two identical 150 m^3 water tanks are used as upper and lower reservoirs with an elevation difference of 100 m. The micro-hydraulic system consists of a 6 kVA water pump and a turbine connected to a 7.5 kW DC generator. During the day, the electrical load of the village is totally covered by PVs through an inverter, and the excess electrical energy pumps water to the upper tank. At night, the stored water is directed to the lower reservoir, rotating the turbine and providing electric power to the village. The entire system is also accompanied by a 100 Ah battery array, to cover peak demand that exceeds the 7.5 kW of the hydro-generator, for a short period of time [20].

The constructed micro-scale PHS systems, presented above, suffer from certain disadvantages. Their small-sized reservoirs and their low-power pumps and turbines, provide a reduced energy storage capacity, compared with the PV generation. To overcome this reduced capacity, the installation of a battery system was more than necessary, rendering the whole installation unsustainable. Additionally, in Goudemand and Donoussa PHS systems, separate pumps and turbines were used, which increased further the initial cost of the installation. Furthermore, in all the aforementioned examples, the PHS system was constructed several years ago when the development of such micro-scale systems was still in its early stages. As a result, their efficiency remained low and their cost quite high. These disadvantages hindered the further implementation of micro-scale PHS systems.

In this paper, a micro-scale hybrid PHS and PV system freed from most of the issues of similar systems mentioned above, specifically sized and configured for the AGH, is proposed. Even if the AGH is a fictitious installation, it roughly describes a very common demand profile for a great number of hotels around the mediterranean sea. Therefore, the conclusions drawn from this work can be expanded to a great number of sea-side hotels or installations of similar size. Specifically, first the system is dimensioned and the estimation of the total cost of the project is carried out. Existing literature and data from the market have been combined and verified in order to create up-to-date cost models. The economic viability of the project is assessed by the most popular indexes for similar hydro-power projects: PP and LCOE. These 2 indexes, especially when used in conjunction with one another, provide useful insights for assessing the investment profitability and success.

The main contributions and results of the paper are summarized below:

- Results indicate that the combined operation of micro-PHS systems and PVs provide an economically sustainable option, with payback periods that range below 6 years.
- The PAT system performance map is evaluated for both nominal and part load operation for both pump and turbine modes.
- Results also indicate that the LCOE value for the selected PAT is calculated 0.08202 €/kWh and is much lower than other energy storage systems [21].

Furthermore, it is demonstrated that micro-PHS can be a financially viable small-scale storage solution when the location and characteristics of the installation permits significant cost cuts in civil works. The case study in this paper concerns the AGH, mainly, due to its location, which is close to both a hill for placing the upper reservoir and the sea for using it as a lower reservoir. Generation performance is quite high, too, since the Mediterranean weather in Greece boosts PV generation (days are sunny for most of the year) and the hotel’s roof can accommodate significant PV capacity. We have also examined the possibility of higher exploitation of PHS by taking advantage of the cheaper electricity rates during the night to store energy, in order to cover part of the demand during the more expensive time-of-use during the day.

All effort has been given, so that the analysis contains realistic data for most operating and financial factors: civil work costs, PV installation costs, pump storage costs, energy production, tariffs for energy purchase from the utility and a precise PAT model that estimates the varying efficiency of PHS under part-load conditions. It has to be noted that this last factor is usually ignored in most studies. The purpose of this paper is to demonstrate that, under some typical conditions, a micro-scale PHS system may be viable solution that can coexist in the so-defined AGH.

The structure of the paper is as follows. Section 2 contains the methodology used to simulate the average Greek hotel, as an energy consumer, PV generation throughout the year, pump-storage system efficiency and operation under full and partial load conditions. Section 3 contains the mathematical model used to calculate PV excess generation or deficiency with respect to the varying load and the amount of water pumped or used for power generation at the PAT and the conditions that this is happening with respect to different strategies and financial incentives. Section 4 contains the cost models and assumptions made to estimate the cost of the system, as well as the compensation scheme of the generated power from the PV or the PAT during operation as a turbine. In the same section the financial indexes used to assess the financial viability of such a project are described. In Section 5, the results from the operational and financial assessment are presented. Conclusions, as well as suggestions for future work, are contained in the last section.

2. Methodology

2.1. The average Greek hotel

In this paper, the AGH was chosen as a case study for analyzing and implementing a modern micro-scale PHS system. First, the dimensions of the AGH must be defined so that its energy profile can then be constructed precisely. We assume that a PHS system could be implemented either at a 4-star or 5-star hotel due to its significant capital cost. We opted for the 4-star hotel, because there is a limited number of 5-star hotels in Greece. Since the majority of hotels in Greece are at seaside, it is assumed that the AGH is located at such a location, near the city of Kalamata. Consulting the “Hellenic Chamber of hotels” [22], an average newly built 4-star hotel consists of 70 rooms. By utilizing data from governmental regulations regarding the individual areas of hotel spaces [23], an average area for the hotel of 2600 m^2 was obtained. This area can be reasonably divided as follows: 1st and 2nd floor will occupy an area of 700 m^2 each, the ground floor 810 m^2 (assuming a lobby, a reception and administrative rooms) and the basement of the building 400 m^2.

Having estimated the dimensions of the AGH, its energy profile will be illustrated. Greek regulations classify buildings according to their energy consumption and performance into the following scale categories: A, B, C, D, E, F, G [24]. Class “A” characterizes an energy efficient building, while class “G” indicates an energy inefficient building. The criteria considered for categorizing buildings according to this scale, include the thermal insulation characteristics of the building's external surfaces and its design, the active and passive heating, cooling and ventilation systems, the method of hot water production, the quality of natural ventilation and air conditioning. Obviously, the AGH occupied with the PHS system, should belong to energy classes A or B, as it would make no sense to have a highly sophisticated and expensive storage system and have abundance of energy wasted, as it is the case in a lower class. Since most of the 4-star Greek hotels belong to "B" energy class, this class is also assumed for the AGH. According to the Energy Inspections of buildings for the year 2021 by the Ministry of Environment and Energy, and the "Building energy efficiency regulation" in Greece Hellenic [24], an annual electricity consumption of 223 kWh/m^2 is expected from the AGH. This consumption includes only electrical energy, since all thermal needs are solely covered by heat pumps. By multiplying the total area of the AGH with the energy consumption per m^2, the total annual energy consumption for the building is obtained, which equals 580 MWh.

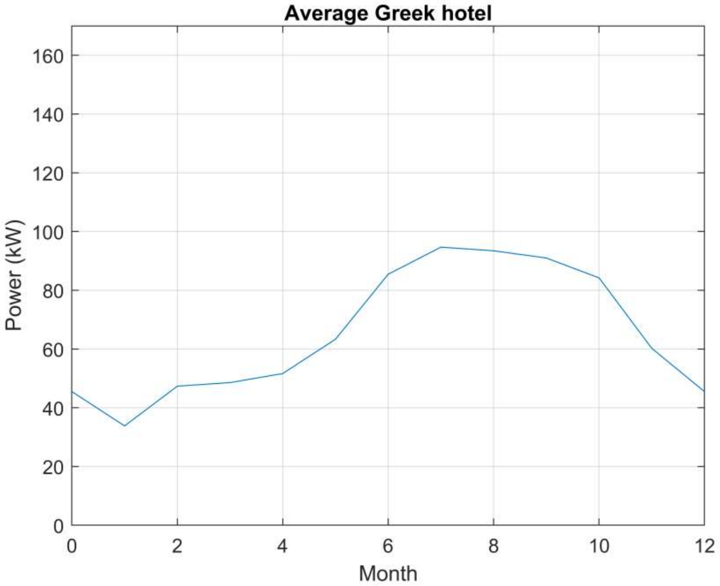

Figure 1. Average monthly power demand of the AVG with respect to the month of the year. It is assumed that the average daily demand is constant throughout each month of the year.

To complete the energy profile of the AGH, since pumping depends on the difference between PV generation and demand, its daily and annual load curves must be constructed. Due to the lack of data for specific 4-star seaside Greek hotels, we had to use data from other Mediterranean hotels found in literature, which fitted the profile of the AGH well: four stars, seaside, similar climate, volume and demand. First, we used the mean daily power demand of a hotel in Malta. The power demand was provided as an average value for all days of the same month [25]. In order to get the estimate for AGH's mean demand (**Figure 1**), we had to scale up those values, in order to make sure that the total aggregate (i.e., annual demand) equals that of the AGH (580 MWh). Similarly, the estimated variation of demand throughout the day has been based on an Italian hotel [26]. The demand curve was provided per square meter (**Figure 2**), so it had to be scaled up, so that its average value is equal to the daily averages provided for each month in **Figure 1**. It is assumed that during a month, the daily demand curves calculated with the above procedure, do not change (**Figure 3**).

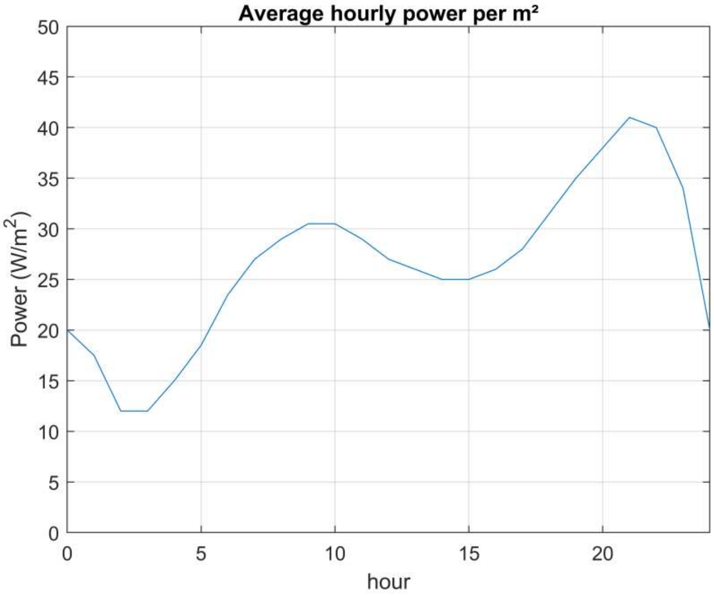

Figure 2. Daily demand curve of AGH (adjusted from hotel with similar profile in Provenzano [26]).

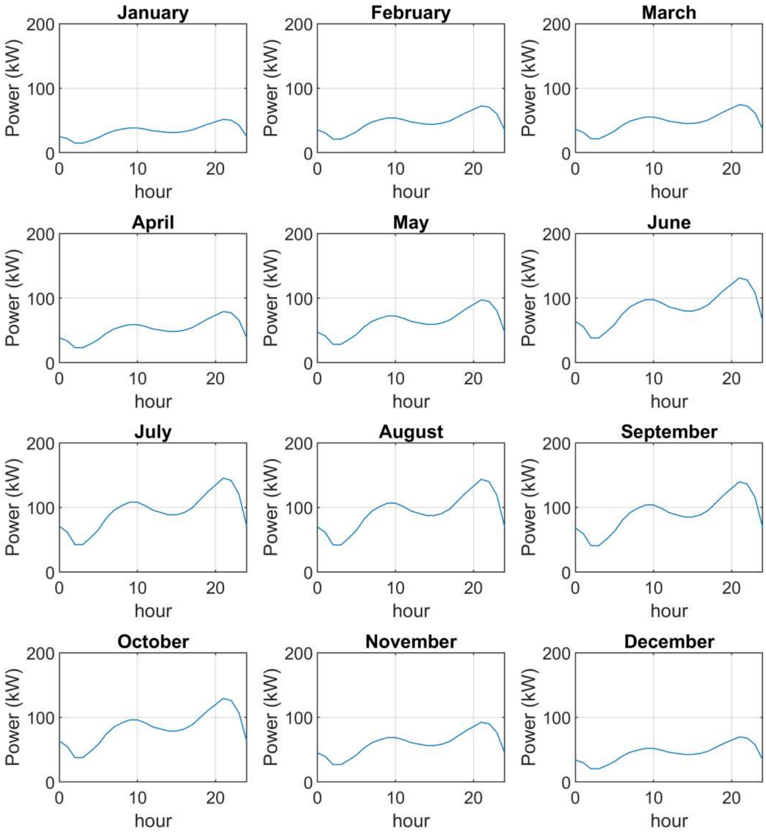

Figure 3. Daily demand curves for each month of the year for AGH.

2.2. PV generation

It is assumed that the RES which provides electrical energy to the AGH is PVs. This energy source is preferred among others (such as wind turbines) mainly because of its low installation and maintenance cost for a micro-scale project. PVs are also a RES that does not have an aesthetic impact to the hotel, as the panels cover the roof of the building.

To obtain the energy production curves from PV panels, some basic data for the AGH and the PV technology need to be determined first. The panels cover the entire surface area of the 700 m^2 roof, tilted at the optimal angle of 35 degrees and having the optimal orientation towards the south, for maximum yearly yield. The irradiation curves for the region of Kalamata were retrieved from the European platform PVGIS European Commission [27].

Choosing the appropriate PV technology for the system plays a pivotal role in the final production curves of PVs. Solar panels from monocrystalline silicon have been chosen, because they are the recommended solution for limited spaces (such as the hotel roof top) due to their higher efficiency among other commercially widespread technologies, at a reasonable cost. If further increase of PV's energy production is sought, sun tracking bases are suggested. However, this technology, displays a much higher installation and maintenance cost, which would probably not be bearable for the average Greek hotel. For the above reasons, constant bases have been selected. Simulation results presented in Section 5 demonstrate that they are sufficient to cover the AGH's energy needs, considering the high number of sunny days in Greece.

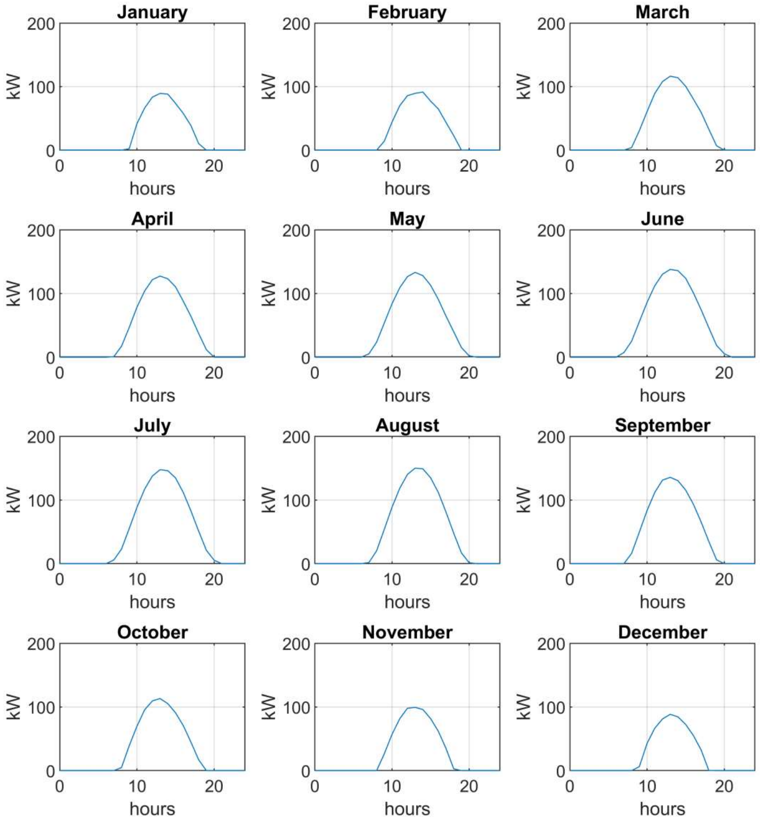

Figure 4. Daily PV energy production curves for each month of the year.

The PV daily production curves have been calculated by applying the daily irradiance curves obtained from the PVGIS platform on the array of panels, assumed to be covering the whole rooftop of AGH and then by assuming an average efficiency factor of 22% for monocrystalline silicon solar panels (**Figure 4**).

2.3. Pump storage

PAT is one of the most common turbine technologies used for pico/micro scale projects, mainly due to its low purchase cost resulting from the wide commercial availability of pumps. Moreover, they are proven robust and require little maintenance, with a lifespan typically greater than 20 years Le Marre et al. [28]. The power output of the PAT in turbine mode is given by Equation (1) [29]:

$$P_T(W) = \gamma \cdot Q_T \cdot H_T \cdot n_h \cdot n_g \tag{1}$$

where γ is the specific weight of water ($9810\ \mathrm{N/m^3}$), where Q_T is the volumetric flow rate ($\mathrm{m^3/s}$) through the turbine, H_T is the turbine's working head (m), while n_h and n_g is the turbine's hydraulic efficiency and generator's efficiency, respectively.

However, despite being highly sufficient in pump mode, their performance prediction in turbine mode is still based on empirical relations and prediction methods, since the characteristic curves in turbine mode are not typically provided by the manufacturers [30]. Among the various analytic models available in literature, the equations of Yang et al. [31] are widely applied because they provide the best accuracy for both flow rate and head ratio estimation, according to Pugliese et al. [32]. Moreover, unlike other models, they correlate PAT performance in turbine mode with PAT performance in pump mode. The latter is always provided by the manufacturer, and thus, their implementation becomes simple and straightforward. The estimation of the BEP in turbine mode when the BEP in pump mode is available, can be determined according to the expressions presented in **Table 1**. PAT performance in turbine mode and operating away from the BEP is calculated by Equation (2) [33]. Among the other expressions available in the literature, this model was selected because the values obtained by CFD analysis and by the model forecasts accurately the PATs' performance in off-design operating conditions that are close to the BEP (with max discrepancy 3%), while a slight mismatch is shown when operating far from it (max discrepancy 10%), as it is explained in the study of Novara and McNabola [34].

$$\frac{H_T}{H_{T,BEP}} = 0.2394 \cdot \left(\frac{Q_T}{Q_{T,BEP}}\right)^2 + 0.769 \cdot \frac{Q_T}{Q_{T,BEP}} \tag{2}$$

Table 1. Correlation of BEP in turbine mode with BEP in pump mode. Subscripts T and P refer to turbine and pump mode.

$\boldsymbol{Q_{T,BEP}}$ [31]	$\boldsymbol{H_{T,BEP}}$ [31]	$\boldsymbol{n_{T,BEP}}$ [34]
$\frac{1.2\ Q_{P,BEP}}{\left(n_{P,BEP}\right)^{0.55}}$	$\frac{1.2\ H_{P,BEP}}{\left(n_{P,BEP}\right)^{1.1}}$	$0.89 - \left(\frac{0.024}{Q_{T,BEP}^{0.41}}\right) - 0.076\left[0.22 + \ln\left(\frac{N_{st}}{52.993}\right)\right]^2$

where $N_{st} = \frac{N_t\sqrt{Q_t}}{H_t{}^{0.75}}$ is the specific speed of the turbine.

3. PHS operation schemes

In this section, the mathematical model of the PHS system, which estimates the energy stored (pumping) or recovered (generating) from it is presented.

3.1. Pumping

Pumping is the process of storing energy in a PHS system by pumping water from a lower tank to a higher tank. In our case this is happening under two possible schemes of operation: a) pumping only during excess PV generation and b) pumping during excess PV generation and during lower prices for purchased electricity from the grid, in a time of use billing system, such as the Greek. Both of them are detailed below.

3.1.1. Pumping only during excess PV generation

The energy production curve of PVs during daytime follows a pattern as shown in **Figure 4**. PVs start producing electrical energy in the morning and stop producing around sunset, so the duration depends on the time of the year. The peak production is observed at midday hours and its magnitude also depends on the time of the year and the clarity of the sky of that day. During peak production and depending on the demand of the AGH at that time of the year, PV generation exceeds demand, and this excess energy can be stored at the PHS system. Practically, this is done by a control system that continuously checks the hotel's hourly power demand and the hourly power production from the PV panels. The hours of the day, which generation exceeds consumption, their difference is calculated, and the possibility of pumping is examined, according to the following algorithm.

Table 2. BEP of the PAT system in pump mode.

$P_{P,BEP}$ (kW)	$Q_{P,BEP}$ (m^3/h)	$H_{P,BEP}$ (m)	$n_{P,BEP}$ (%)
15	275	20	92
25	460	20	92
35	645	20	92.5
45	830	20	92.5
55	1000	20	92.5
65	1200	20	93
75	1380	20	93
85	1560	20	93.5

Each PAT has its own nominal power consumption and a corresponding water supply when operating as a pump (**Table 2**). According to this nominal power consumption and the difference between generation and demand, the algorithm allows pumping or not and calculates the amount of water in the tank every hour of the day. First, the hours needed for the upper reservoir to be filled if the PAT operates continuously at its nominal power are determined. Two cases are then examined:

- If the difference between generation and demand is greater than the nominal power of the PAT, then the PAT is assumed to be pumping water with nominal flow by consuming nominal power. If during this mode of PAT's operation, we calculate that enough water has been pumped to fill in the upper tank, then we assume that pumping stops, and the tank is full. After this point in time, PV generation is assumed capped to the amount equal to demand, until demand becomes higher than generation again, which means that PV generation does not need to be capped longer.

- If these hours are fewer than those during which the excess power from the PV exceeds the power demand by an amount greater than the consumption of the PAT, the hours when the difference is the greatest are selected. In this case the PAT operates in its nominal power.
- If the difference between generation and demand is lower than 50% of the nominal power of the PAT, then the PAT is not pumping any water. This is because, we have assumed that operating the PAT as a pump in lower than half load would cause unacceptably high wear, cavitation effect and generally losses, significantly reducing its lifetime and increasing maintenance costs. During this time the PV generation is capped to an amount equal to demand, until the demand surpasses possible PV generation again.
- If the difference between generation and demand is between 50% and 100% of the nominal power of the PAT, then the PAT is pumping water, but with a flow and efficiency lower than nominal. In this range of operation, the height remains constant, but the pumping efficiency, the rotational speed of the PAT and the water supply are changing. From the simulation of the PAT based on its operating model, the power values and the corresponding efficiencies for water flow rates of 0.8, 0.6 and 0.5 of the nominal values were obtained. It was observed that the correlation between the PAT's power and the water flow is almost linear. Thus, the water flow as a function of surplus PV power can be obtained. The BEP and performance of the PAT system in pump mode for different flow rates and power outputs is displayed in **Figure 5**. By calculating these subnominal flow rates for each hour of the day, the amount of water pumped to the upper tank, thus the total amount of water in the tank, can be calculated. If the tank becomes full, pumping stops. After this point in time, PV generation is assumed capped to the amount equal to demand, until demand becomes higher than generation again, which means that PV generation does not need to be capped longer.

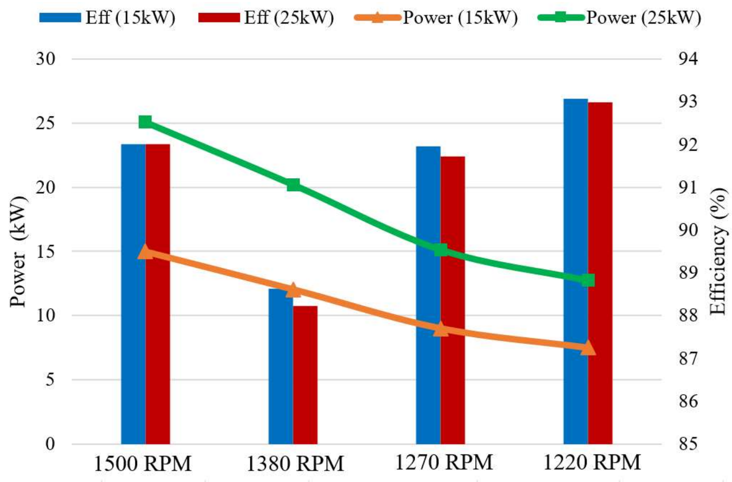

(a)

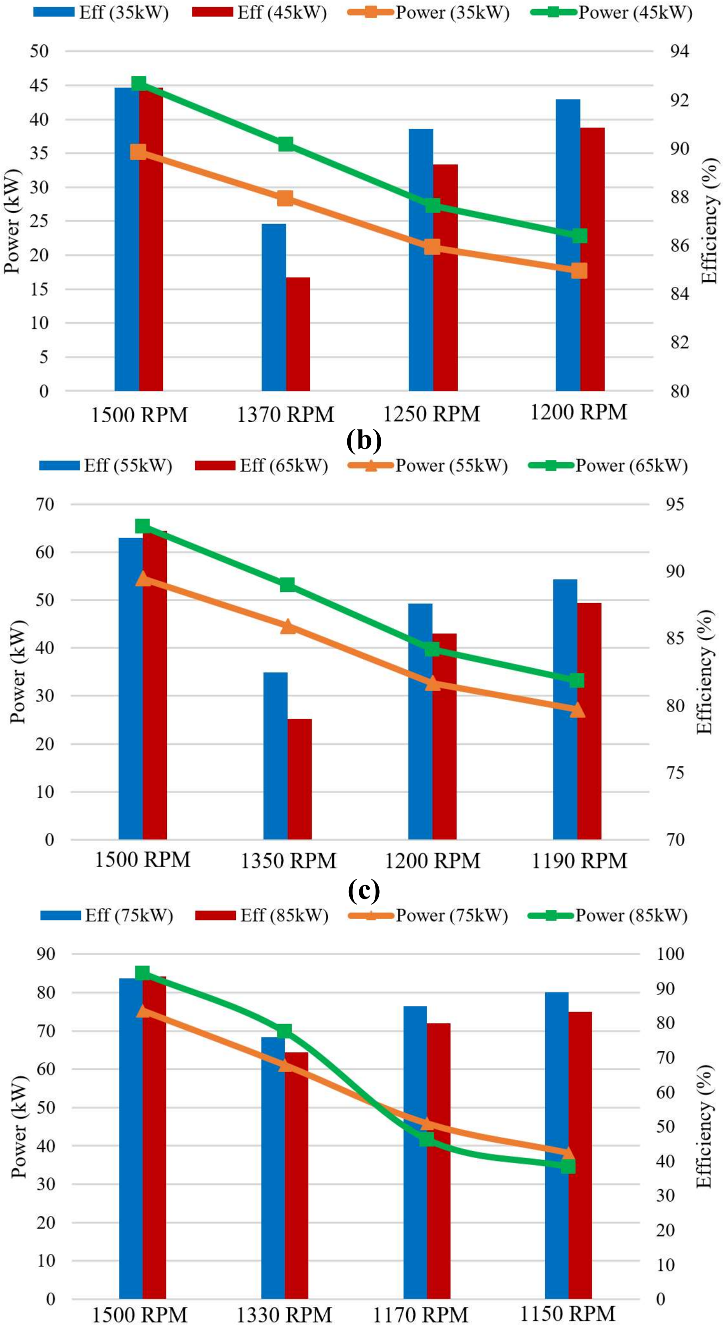

Figure 5. PAT performance in pump mode for different flow rates for **(a)** 15 and 25 kW; **(b)** 35 and 45 kW; **(c)** 55 and 65 kW; **(d)** 75 and 85 kW.

In any case, the amount of water pumped in the upper tank is automatically subtracted from the lower tank.

3.1.2. Pumping during excess PV generation and cheaper tariff

In subsection 3.1.1 the operation of the pumping system is limited to time periods that PV generation is greater than demand. This practically means that it operates only during the day. In this subsection, an analysis is conducted concerning the extension of the operation of the PHS system in a second daily cycle, during the night, using the cheaper tariff provided by the electrical utility during that time.

In Greece, some of the electricity suppliers provide a time-of-use billing option, giving a cheaper tariff for electrical energy consumed during 8 specific hours of the day. This reduced tariff takes place from 23:00 to 07:00 between 1 May and 1 November and from 02:00 to 08:00 and 15:00 to 17:00 for the rest of the year. In the present analysis, for simplicity of calculations, it was assumed that the cheaper tariff begins from 02:00 and ends at 07:00 throughout the year. It will be demonstrated from the simulation results in Section 5, that keeping only the night part of the cheaper tariff throughout the year, did not affect the pumping pattern. During winter afternoons, even if PV generation is reduced when compared with the summer, the much lower demand keeps PV excess power at a sufficient level to make the cheaper tariff useless.

The prices for daytime and nighttime electricity tariffs from the most popular supplier in Greece (PPC) for every month of the year 2023 are presented in **Table 3** [35]. It has to be noted that the tariff prices presented in this table, must be considered only as indicative, as they may vary significantly from supplier to supplier, from year to year and from country to country. Therefore, in order for such a pumping scheme to make sense, a basic principle must be met: the ratio of the night electricity tariff over the daytime tariff should be less than the cycle efficiency of the PHS system, which is calculated by multiplying the individual efficiencies of pumping and generating. Otherwise, there is no reason for night pumping, since the cost of the consumed energy by the PAT is certainly more than the financial gain derived from the morning generation.

Table 3. Daytime and nighttime electricity tariffs.

	Daytime tariff (€/kWh)	Nighttime tariff (€/kWh)	Ratio nighttime/daytime
January	0.404	0.314	0.777
February	0.218	0.138	0.633
March	0.238	0.154	0.647
April	0.214	0.124	0.579
May	0.208	0.118	0.567
June	0.204	0.114	0.559
July	0.204	0.114	0.559
August	0.204	0.114	0.559
September	0.204	0.114	0.559
October	0.217	0.114	0.525
November	0.256	0.129	0.504
December	0.256	0.129	0.504

The pumping process during the night is much simpler than the corresponding procedure during the noon (excess of PV generation). For the precise definition of the pumping hours at night, the system needs to predict the power demand during the next morning's hours from the end of the nighttime tariff until the time when the entire AGH's load is covered by PVs. Since such a precise prediction is quite difficult to make, the estimation of the next day's consumption is the consumption of the previous day. This can be easily assumed because it was considered in subsection 2.1 that during a month, the daily load curve of the AGH remains practically constant.

In the case of pumping at night, the algorithm followed for pumping water to the upper reservoir is easier than the corresponding procedure of pumping at noon. At night, there is no point in operating the pump below its rated power and maximum efficiency. The required pumping hours to fill the upper tank are calculated according to the nominal water flow at the PAT's nominal power. It should also be checked if the 7 h of cheaper electricity are sufficient for the pump to fill the upper tank, according to its nominal power and flow. If the upper tank becomes full, the pumping operation stops. In the case of operating the PHS system in two daily cycles, the midday pumping due to excess PV generation is completely independent of the nighttime pumping with cheaper electricity tariff, which greatly simplifies the calculations.

3.2. Generation

Generation is the process in PHS systems during which energy is recovered from the upper water tank by letting water flow to the lower tank through the hydro generator. In our case, both pumping and generation is performed by the same device, PAT. Generation is performed when demand surpasses PV generation, no matter what scheme is followed during pumping (see Section 3.1).

The decision process when the generation takes place is simpler than the pumping process for both pumping schemes, analyzed in subsections 3.1.1 and 3.1.2. In the first scheme (pumping occurs only at midday from PV excess energy), the stored energy is recovered in order to cover part of the demand of the hotel during the afternoon or evening. Due to the high demand during these hours, it is considered that all the PATs studied in this paper are operating in their nominal power. Even for the PAT with the highest nominal power (85 kW), the maximum power the generator can provide to the hotel is quite lower from the demand during the evening. Thus, the calculations are simplified, and the PAT is operating at its BEP.

Once the pumping process is completed at midday, the PHS control system calculates the time required for the PAT to operate, in order to empty the upper reservoir and recover energy to the hotel. Then, based on the load data from the previous day (since the prediction for the next day is uncertain and inaccurate), the hours during which the peak load is observed, are identified. Finally, prioritizing the hour with the highest peak load and in descending order to the hour with the lowest power demand, energy is recovered from the PHS system. When the upper reservoir is emptied, the PAT stops generating.

Similarly, once the nighttime pumping is completed, according to subsection 3.1.2, the energy recovered from the AGH in the morning is calculated, based on the stored water quantity in the tank and the nominal water flow of the PAT. The PAT is chosen to operate at its nominal power during production, so that maximum efficiency is achieved. Thus, the PAT operating at its BEP can provide the maximum energy and financial gain to the AGH.

The BEP of the PAT system in turbine mode, as calculated by Equation (2) and **Table 1** is displayed in **Table 4**. However, for all cases, turbine cannot operate at its nominal head $H_{T,BEP}$, as it exceeds the total elevation of the upper reservoir $H = 20$ m, and therefore, it would have to operate at a lower H_T. PAT performance in turbine mode and operating away from the BEP is calculated by Equation (2) [33], while the results for all cases are displayed in **Table 5**.

Table 4. BEP of the PAT system in turbine mode.

$P_{T,BEP}$ (kW)	$Q_{T,BEP}$ (m^3/h)	$H_{T,BEP}$ (m)	$n_{T,BEP}$ (%)
24	345	26.3	82.6
41	577	26.3	83.5
57	807	26.1	83.9
74	1039	26.1	84
89	1252	26.1	84.2
106	1498	25.9	84.2
122	1723	25.9	84.2
136	1942	25.8	84.1

Table 5. PAT performance for turbine mode for H_T =15 m and N = 1500 RPM.

P_T (kW)	Q_T (m^3/h)	H_T (m)	n_T (%)
8.77	214	15	75
14.6	359	15	75
20.62	504	15	75
26.54	649	15	75
31.97	782	15	75
38.45	940	15	75
44.22	1081	15	75
50.09	1225	15	75

3.3. Daily cycle

The process of pumping and generation described in Sections 3.1 and 3.2, respectively, should be automated in a real-world system. The flowchart below (**Figure 6**) describes the algorithmic process that should be followed by any automation equipment aiming at maximizing the performance of the PHS system. The flowchart is divided in two parts: daily and night operation. In daily operation, the energy production is compared with the AGH's demand. When PV production exceeds demand, the PHS system can pump water to the upper reservoir until either the upper tank becomes full or the available excess energy is reduced to zero. In these situations the PAT can operate as a pump only when the difference between generation and demand is greater than the half of the PAT's nominal power. Otherwise, pumping stops or never begins. In night operation, the ratio between daytime and nighttime energy tariffs is compared with the PHS system's overall efficiency. If the ratio is lower than system's efficiency, the PHS system starts pumping water at night. Pumping procedure stops either when the necessary volume of water has been pumped to the upper reservoir or the nighttime tariff has ended. In both situations, when the nighttime reduced billing stops, the PHS system begin generation. The required equipment that could implement this automation logic is described in subsection 4.2.2.

Figure 6. Flowchart describing the automatic logic followed by PHS system for optimal performance.

A daily cycle of the suggested PHS schemes is explained below, so that the reader has a clearer view of the combined operation of pumping and generation. In **Figure 7**, the difference between daily demand and PV generation during a typical day of a month of June, is presented with the blue curve. It can be noticed that there is excess generation during noon (negative values) that without the PHS system would have to be fully capped. The operation of the PHS system with a 25 kW PAT, increases demand during pumping and covers part of the demand during generation (red curve). This exchange of energy from and to the PHS can be noticed as the difference between the two curves. Area "D" is the excess PV energy diverted to pumping according to the scheme presented in subsection 3.1.1. Obviously, much less PV power has to be capped during that period (area "C"). Additional energy can be stored (area "A") using the cheaper time-of-use night tariff, according to subection 3.1.2. That stored energy is supplied to the AGH when the more expensive time-of-use tariff starts at 7 am (area "B"). The energy stored during excess PV generation is supplied to AGH when demand is greater than PV generation again in the evening (area "E").

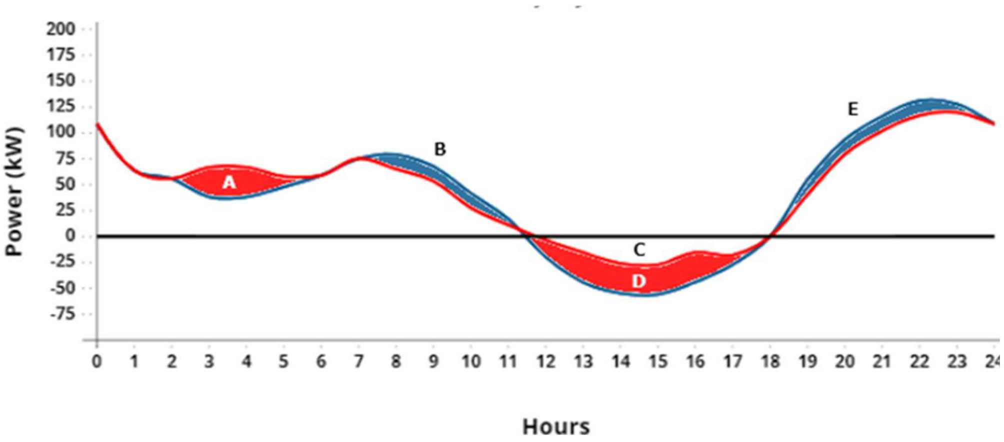

Figure 7. Impact of PHS system on demand of the AGH with PV generation.

Table 6 summarizes the different energy amounts that are exchanged between the PV (generation), PHS (storage) and AGH (demand). During July and October, two months of the year that the AGH operates close to its capacity (high touristic season, thus high demand) pumping during the night increases ("A" in **Figure 8c,d**), so that the savings from the difference of day and night tariffs are maximized ("B" in **Figure 8c,d**). April, a month that AGH has a rather low demand (low touristic season), but the PV generation is rather efficient (long sunny days, but low ambient temperatures) a great amount of PV energy is capped ("C" in **Figure 8b**). On the contrary, during October, the storage capacity of the PHS is underused during the day ("D" in **Figure 8d**), due to the relevantly high demand (high touristic season) but relevantly low PV generation (see October in **Figure 4**), Obviously, the under-usage of PHS during the evening leads to much less energy recovered as well ("E" in **Figure 8d**). For the rest of the cases, storage capacity is better used during the day ("D" in **Figure 8a–c**), plus much more energy is recovered during the evening ("E" in **Figure 8a–c**).

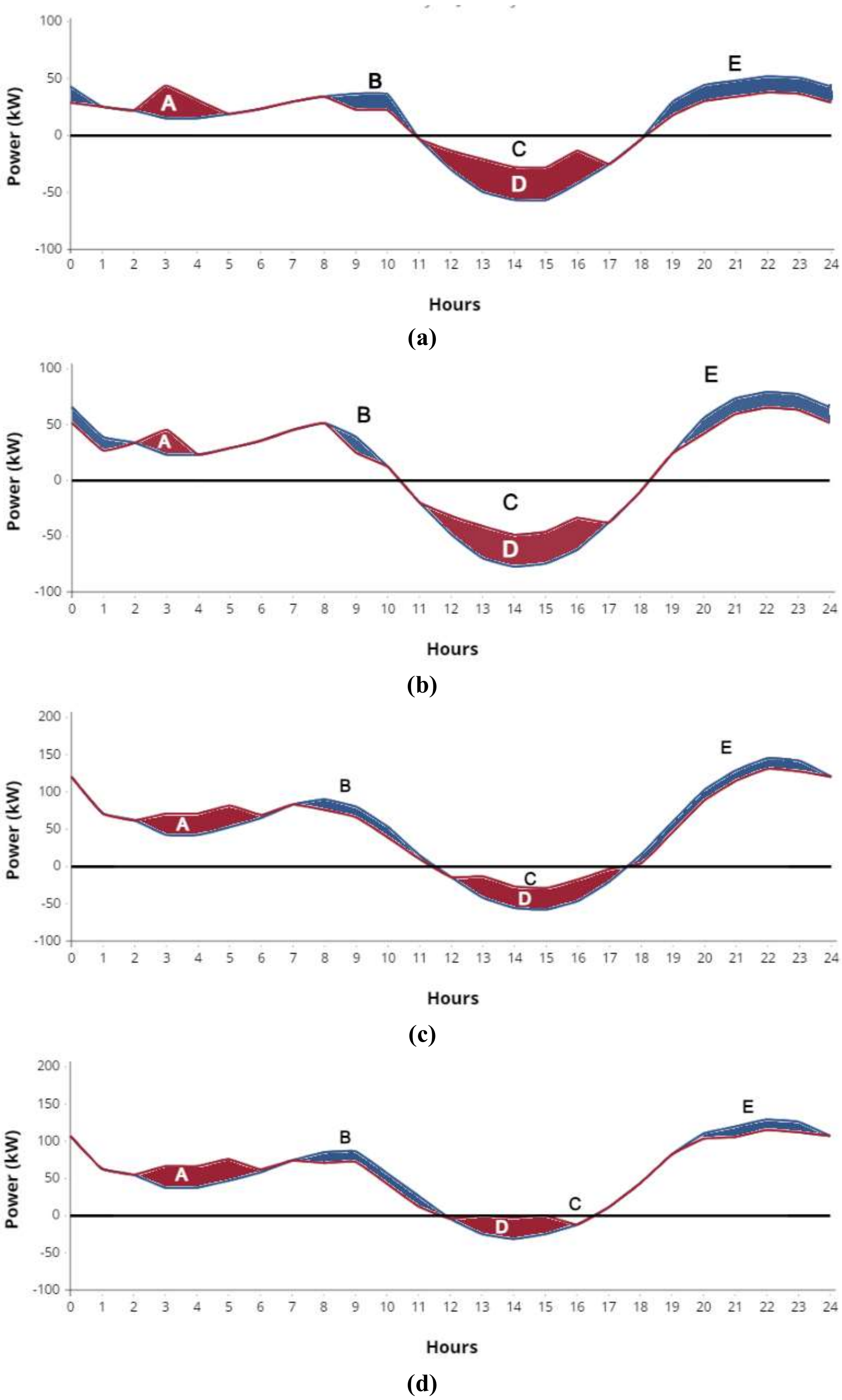

(a)

(b)

(c)

(d)

Figure 8. 25 kW PHS system daily performance under different demand and generation conditions: **(a)** January; **(b)** April; **(c)** July; **(d)** October.

Table 6. Energy amounts exchanged between the PV (generation), PHS (storage) and AGH (demand).

	A	B	C	D	E
January	44.62	27.9	134.6	130.7	81.61
April	22.31	13.95	268.0	130.7	81.61
July	89.57	55.8	103.8	130.7	81.61
October	89.57	55.8	18.8	79.4	48.83

4. Cost models

In this section, the indexes used to assess the financial viability of the simulated project are described. Furthermore, the cost models and assumptions made to estimate the overall cost of the system to be installed and maintained will be explained. Finally, the compensation scheme of the generated power from the PV or PAT will be described. The implementation of the PHS achieves attractive payback periods (5 years on average), which are in accordance with those of micro hydroelectric projects employing PATs, that typically range between 2 and 5 years, according to Pugliese and Giugni [12], Laghari et al. [36], the fact that the renewable energy overproduction is not wasted due to storage leads to low LCOE values (approximately 0.09 €/kWh) that are in compliance with other RES technologies with storage.

4.1. Financial indexes

For the evaluation of the investment and for proving that a micro-scale PHS system is feasible and economically viable, two separate financial indexes are presented and calculated in this subsection: LCOE and PP.

The LCOE is a method by which the price per energy unit that balances out the total cost of the project is obtained. The calculation of the LCOE can be performed either over a one-year period or over the lifetime of the project, with the latter method providing greater accuracy [37]. The mathematically calculation of the LCOE is given by Equation (3) [38]:

$$\mathrm{LCOE} = \frac{\sum_t^n \frac{I_t + M_t + F_t}{(1+r)^t}}{\sum_t^n \frac{E_t}{(1+r)^t}} \tag{3}$$

where I_t represents the investment cost in year t (€), M_t in the operation and maintenance cost in year t (€), F_t stands for the fuel cost in year t (€), E_t is the generated electrical energy from the power unit in year t (€), r is the discount rate and n represents the lifetime of the installation.

In our case, the energy production unit is the PVs in combination with the PHS system. The lifetime of the entire system is limited to 25 years due to the PVs panel's lifetime. Additionally, a zero-discount rate and a zero-fuel cost (as PVs are a RES) are considered. The investment cost in year *t*, is fully depreciated in the first year of construction. Thus, Equation (3) is simplified as follows:

$$\mathrm{LCOE} = \frac{I_0 + n \cdot M_t}{n \cdot E_t} \tag{4}$$

The denominator of Equation (4) includes the total generated electrical energy for the AGH over its operating years and consists of three components. The first one is the total energy generated from the PVs and received directly by the hotel (E_{pv}). The second one refers to the total energy generated by the PHS system during the evening (E_{ev}) and the third one refers to the total energy generated by the PHS system during the morning (E_{m}). Thus, Equation (4) can be described as follows:

$$\mathrm{LCOE} = \frac{I_0 + n \cdot M_t}{n \cdot (E_{\mathrm{pv}} + E_{\mathrm{ev}} + E_{\mathrm{m}})} \tag{5}$$

On the other hand, PP is one simpler financial index than LCOE, for evaluating the investment and is referred to the time needed for an investment to recover its initial outlay, in terms of profits or savings. The calculation of PP is given by Equation (6):

$$\mathrm{PP} = \frac{I_0}{G_{\mathrm{an}}} \tag{6}$$

where I_0 represents the total investment cost, and G_{an} stands for the annual energy gain by the operation of the system.

4.2. System costs

4.2.1. PVs

The total cost of the photovoltaic installation consists of the individual costs of the panels, inverters, constant mounting bases, electrical equipment and the installation works.

Starting with the panels, for a total installation capacity of 150 kWp, 273 monocrystalline silicon panels are required, each costing €190. Thus, the total cost amounts to €51,870. To convert the DC current generated by the PVs into AC, to can be connected to the AGH's electrical system, three 3-phase DC/AC inverters without transformers, with 50 kW nominal power and €3300 cost each, are required. For supervising and monitoring the PV installation, a communication unit is selected, costing €100. The mounting system of the 273 PV panels on the flat floor of the AGH will be carried out using fixed mounting brackets with a total cost of €19,040. For the proper operation and control of the PVs and for their connection with the AGH, electrical panel boards, energy meters, suitable solar cables, circuit brakers and relays are required. The cost of this electrical equipment is estimated at €14,800. Finally, the labor cost for the panels' installation amounts to €24,000 and includes the transportation of the equipment to the hotel and their installation.

Thus, the total investment expenses for the PVs amount to €148,440 (including taxes). If this is divided by the installed capacity, the cost per installed kWp is €990. This cost is derived from an offer obtained from a company in Greece [39] and involves material prices for the year 2023. Indeed, the cost per installed kWp (€990) is very close to the cost determined theoretically by Tzouras [37] in his study (€975) for the installation of monocrystalline silicon PV panels with fixed bases on a roof. The annual maintenance expenditures for the PVs have been calculated at €2019 and cover panel maintenance, cleaning and insurance.

4.2.2. PHS

Reservoirs

The Goudemand example, mentioned in the introductory Section of this work, has placed the upper reservoir on the roof of the building. However, such a construction requires the structural reinforcement of the building's roof to support the tank, as well the reinforcement of the adjacent floors, in order to overcome the limitations regarding the stability. This problem escalates as the volume of the upper tank increases. In our case, where the upper reservoir has a volume of 2100 m^3, the indicative cost of reinforcing the building amounts to €1,274,350, according to a study by a civil engineer [40], rendering the entire system unsustainable and uneconomical. Therefore, the construction of an artificial hill in the hotel's vicinity for the placement of the upper tank could be a more sustainable solution. In this case, according to a study by a civil engineer [40], the cost of constructing an embankment hill amounts to €128,000, much lower than the cost of building's reinforcement. The expenditures for the upper reservoir could be minimized by using an existing hill close to the hotel, for placing the upper tank. This assumption has been handled in this paper. Therefore, the only expense related to the reservoirs is the construction cost of the upper tank, which according to a civil engineer's study, amounts to €268,140.

Reservoir costs are the main force of ambiguity about the total cost and implementation of the suggested system to a hotel. Indeed, the suggested system cannot be implemented in all existing hotels. In order for the cost of the tanks to be bearable from the hotel owners, a nearby hill is required to provide the required elevation. In this work, we have assumed that this elevation is provided by the surrounding landscape within the hotel property and only the reservoir will have to be constructed on top of it. Otherwise, this elevation will have to be created with appropriate civil work, which, as already mentioned, will cost approximately €128,000 in Greece. Of course, the exact cost is hard to define, as it heavily depends on location of the hotel and the cost of the required workforce and expertise: different costs apply to a small island, seaside town etc. Furthermore, most Greek hotels may be near the sea that could be used as the lower "tank" but access to the sea may not always be possible at a reasonable cost, due to geomorphological, legal or practical reasons. Of course, that cost also varies greatly, depending on the level of hydraulic works required to connect the system to the sea, as well as the cost of purchasing or hiring land in between or even acquiring appropriate permits from the authorities. Finally, even if there is a natural elevation for the upper reservoir within the property and the sea shore is accessible for use as a lower reservoir, energy savings from PHS operation may not always adequate to compensate for the loss of revenue from using the occupied space otherwise, e.g., building a garden, kiosk or even another hotel wing.

PATs

In this paper, the analysis included the study of 8 different PATs with power ranging from 15 to 85 kW. The estimation of the electro-mechanical equipment cost for the PAT C_{EM} system is provided by the most recent expressions available in the literature Alzohbi [41], Novara et al. [42], Saidur et al. [43], which are presented in **Table 7**. PAT estimation is usually correlated as a function of power (P_{BEP}), head (H_{BEP}) and flow rate (Q_{BEP}) at design point. In the same table, the individual cost of the PAT-generator set $C_{\mathrm{PAT+GEN}}$ [42] and the inverter required by PATs for the regulation of their shaft speed C_{inv} [43], is provided. In this case, total cost C_{EM} is given by the sum of these two individual costs, contrary to the expression found in Alzohbi et al. [41], which directly calculates C_{EM}. Implementing the equations, shown in **Table 7**, for the PAT cost, based on cost models found in the literature mentioned above, the C_{EM} per analyzed PAT is calculated and presented in **Figure 9**. It is observed that, the deviation between the final costs calculated by the two approaches is insignificant. For the evaluation of the LCOE and payback period, the annual operation and maintenance cost $C_{\mathrm{O\&M}}$ of the PAT were considered 15% of C_{EM}, as it is suggested from various studies by Marini et al. [44], De Marchis et al. [45], Hammond et al. [46].

Table 7. Calculation of C_{EM}, based on cost models found in the literature.

Expression	Related Cost	References
$1355.6 \times P_{\mathrm{BEP}}{}^{0.8296} \times H_{\mathrm{BEP}}{}^{-0.1035}$ (€)	PAT + gen + inverter	Alzohbi [41]
$11{,}913.91 \times Q_{\mathrm{BEP}} \times H_{\mathrm{BEP}}{}^{0.5} + 1289.92$ (€)	PAT + gen	Novara et al. [42]
$1239.9 + 165.72 \times P$(€)	Inverter	Saidur et al. [43]

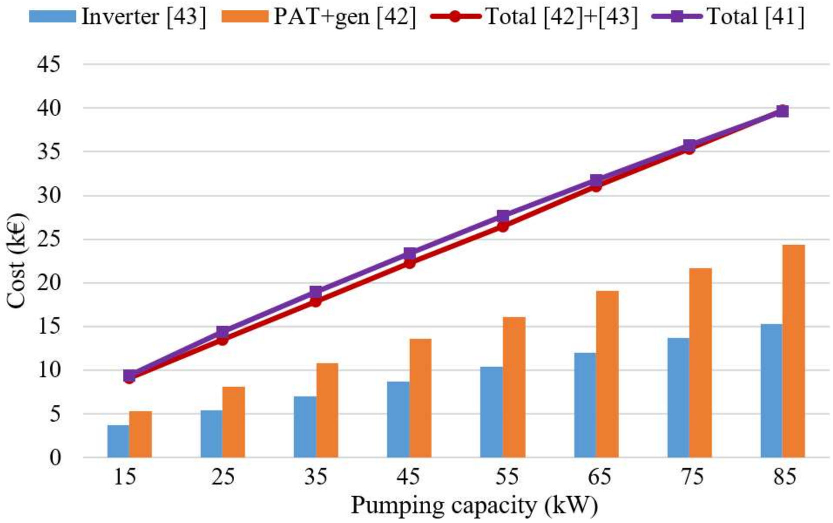

Figure 9. Total electro-mechanical equipment cost (C_{EM}), PAT-generator set cost ($C_{\mathrm{PAT+GEN}}$) and inverter cost (C_{inv}) estimation with respect to different pumping capacities.

Sometimes due to unexpected leakages of the tanks, the upper reservoir can be emptied earlier than calculated and the PAT can be operating with almost zero water pressure. This can cause serious damage to the PAT, such as wear and cavitation. To overcome this unexpected situation, pressure gauges are installed within the tanks, which, once the water level exceeds a minimum threshold, stop the generation.

Piping system and electro-valves

For transferring water from the upper to the lower reservoir and vice versa, flexible PVC, 16-bar pipes are the most appropriate. Their connection with the reservoirs and with the inlet and outlet of the pump is achieved through a flange and a neck, while the sealing of the connection is ensured using electrofusion. For the entire piping installation, the following are required: 20 meters of flexible PVC pipe, 4 metal flanges, 4 necks and 4 electrofusions. Their cost ranges according to the internal and external diameter of each PAT as shown in **Table 8**.

For regulating water flow during generation, electro-valves with pneumatic actuator are selected. Their size depends on the external diameter of the PAT and hence their cost, which is also shown in **Table 8**, varies for each PAT studied.

Table 8. Total costs for PATs, piping system and electro-valves.

PAT nominal power (kW)	PAT cost (€)	Piping system cost (€)	Electro-valve cost (€)
15	9085.66	971.16	651.76
25	13,480.90	1571.76	808.84
35	17,876.13	1571.76	808.84
45	22,271.36	2485.96	1193.33
55	26,444.59	4021.24	1670.00
65	31,061.83	4021.24	1670.00
75	35,383.06	5602.00	3439.70
85	39,704.29	5602.00	3439.70

Automation system

An automation system is needed by PHS to operate according to the operating schemes explained in Section 3. This system consists mainly of a PLC. The PLC receives data from pressure meters, placed inside the reservoirs, and from the energy analyzer, and acts through a SCADA software on the electro-valve to control production. For connecting and disconnecting the PAT during the power generation, PLC acts on automations and relays in the low voltage electric panel board. The individual cost of these systems is presented in **Table 9** and is constant, regardless of the nominal power of each PAT.

Table 9. Total costs for the components of automation system.

Automation	Cost (€)
Programmable Logic Controller (PLC)	520.00
Energy analyzer	360.00
2 pressure meters	480.00
SCADA software	1200.00
Electrical equipment	1500.00

4.3. Total system cost

In the following **Table 10**, the total cost of the system for the different configurations is provided. As the reservoir and the automation system remains the same, indifferent of the PAT size, the total cost becomes a function of PAT size, since PAT size also determines the rest of the costs (piping system and electro-valves).

Table 10. Total system cost with respect to PAT size.

PAT nominal power (kW)	Total system cost (€)
15	431,349.6
25	436,501.5
35	440,896.7
45	446,590.7
55	452,775.8
65	457,393.1
75	465,064.8
85	469,386.0

4.4. Compensation scheme

It is considered that in a zero feed-in system, PV generation cannot be injected to the grid or cannot be compensated. In zero-feed grids, the transmission system is overly stretched, and no more permits can be given for net-metered or by-all-sell-all systems [47]. This is not an unusual situation already for many grids with high penetration of RES, such as the Greek system. Net metering started in Greece in 2013 and is about to end in 2024. With a net-metering system, consumers who have installed PVs on the roof of their homes, can inject the excess energy into the grid and be paid about that by the reduction of their energy bills. Now, such a system is replaced by a net-billing system. Similar results should be expected, though, if the system was simulated as a net-billing system [47], as this compensation scheme also incentivizes self-consumption of RES generation, such as the one provided by the PHS. Thus, consumers who have already installed a PV system at their homes, or are about to make such an installation, should find other ways to store the excess energy. From now on, in Greece, the only way the electricity to be reduced is by storing the excess generation through a PHS system and by covering parts of the peak demand with that energy.

The comparison between the reduced electricity bills and the electricity bills the AGH would pay without PVs and PHS, is the measurable compensation received by the operation of combined PVs and PHS. Separate analysis will follow: a) one that will calculate the cost of electricity for the AGH without PVs, which will be used as a base case, b) one with PVs but no PHS and c) one with both PVs and PHS in place. This way, the part of the compensation received purely by the operation of PHS will also be calculated, as a difference between the results of analysis b) and c).

5. Operational and financial assessment

In this Section, the methodology described in Section 2 is used to simulate the demand of the AGH, PV generation and PHS operation. The PHS system is assumed to take advantage of all the special properties of the AGH and is appropriately dimensioned for it (see subsection 4.1.1). The operation of the overall system is simulated and analyzed. The output of this analysis becomes the input for the financial assessment of the project. An AGH without the PHS is first considered as a benchmark case. Then its performance and financial attributes are compared with the same system, but with a PHS installed. The impact of both pumping schemes is considered (see subsections 3.1.1 and 3.1.2). The common system properties between all cases are the energy profile of the AGH, presented in Section 2.1, and the PV generation estimated in Section 2.2.

5.1. PV generation only

From the electricity tariffs presented in subsection 3.1.2 and the demand curves provided in Section 2.1, the annual energy cost for the AGH without PVs and PHS can be calculated. This cost amounts to 192,432 €/year.

With the PVs installed at the rooftop, covering part of the demand during daytime and having all excess generation during noon capped, the energy expenditures are reduced by 76,876 €/year to 115,556 €/year.

5.2. PVs and storage of excess generation at PHS

In this case, the PHS system pumps water only once per daily cycle, during excess PV generation, according to the scheme detailed in subsection 3.1.1. The results deriving from this analysis for different sizes of PATs (first column) are presented in **Table 11**. The new annual energy costs for each PAT size in order to cover AGH's demand are listed in the second column. By subtracting those costs from the annual energy cost of operating the system without PHS (Section 5.1), the profit from PHS operation can be calculated (third column). Using the annual costs and profits, the LCOE and the PP are also calculated according to Section 4.3, and listed in columns four and five, respectively.

Table 11. Annual energy cost and profits for the operation of the PHS system according to the scheme presented in subsection 3.1.1.

PAT (kW)	Energy cost (€)	Profit from PHS operation (€)	LCOE (€/kWh)	PP (yr)
15	107,070.83	8485.30	0.08512	5.05
25	104,781.04	10,775.09	0.08655	4.98
35	104,651.25	10,904.88	0.08978	5.02
45	105,253.73	10,302.40	0.09036	5.12
55	105,554.79	10,001.34	0.09780	5.21
65	106,863.69	8692.44	0.10282	5.34
75	108,212.44	7343.69	0.10833	5.52
85	107,286.81	8269.32	0.11063	5.51

5.3. Storage of excess PV generation and energy from the grid during lower tariff at PHS

The last case concerns the operation of the PHS system twice per daily cycle: a) when PV generation is greater than AGH's demand, and b) during the night, using the lower energy tariff provided by the grid. From the analysis conducted in this case (**Table 12**), even if more energy was purchased from the grid, the total energy cost has been reduced further from nighttime pumping (third column). In the same table, the LCOE and the PP for this case are also calculated according to Section 4.3.

Table 12. Annual energy cost and profits for the operation of the PHS system according to the scheme presented in subsection 3.1.2.

PAT (kW)	Energy cost (€)	Profit from PHS operation (€)	LCOE (€/kWh)	PP (yr)
15	106,844.22	226.61	0.08268	5.04
25	104,370.69	410.35	0.08202	4.96
35	104,056.37	594.88	0.08354	4.99
45	104,560.43	693.30	0.08661	5.08
55	104,847.64	707.15	0.08926	5.17
65	105,397.13	1466.56	0.09334	5.20
75	107,343.96	869.22	0.09902	5.47
85	106,356.96	929.85	0.10230	5.45

5.4. Comparison of results between cases

Figure 10 presents a comparison of the economic indexes calculated for the AGH for various PAT sized for the same PHS system under the two different pumping schemes: pumping water once in a daily cycle (Section 5.2) and pumping twice in a daily cycle (Section 5.3). It can be easily noticed that PPs and LCOEs are comparable to other RES technologies with storage.

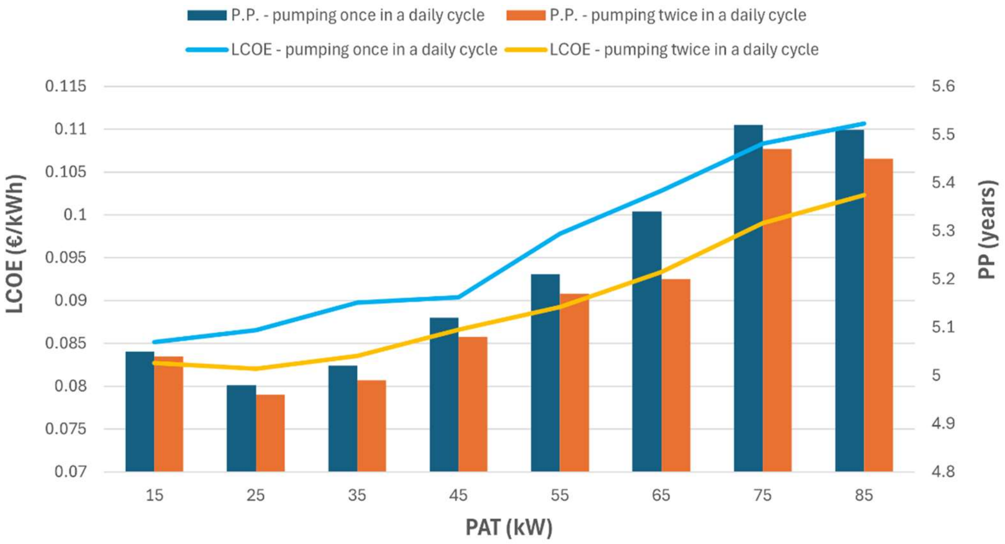

Figure 10. LCOE and PP of PHS system pumping either once or twice in a daily cycle.

First, if pumping takes place only when there is excess PV generation (i.e., once in a daily cycle) then the bigger the PAT becomes the more the LCOE increases. There is an optimal size of 25 kW, though, that fits AGHs demand and generation profile, providing the minimum PP. Furthermore, if the profits from PHS operation with respect to different PAT sizes are compared, then the 35 kW PAT is the optimal choice offering 10,904.88 €/year.

Interestingly, the same PAT size of 25 kW is considered as optimal, if the LCOE and PP are chosen as the economic assessment indexes for a PHS system that pumps water also during the cheaper energy tariff (pumping twice in a daily cycle). The results presented so far indicate that the construction of a micro-scale PHS system in buildings with a profile close to that of the AGH is feasible and economically viable. Obviously, if investment decisions are based on PP or LCOE they may be different from those derived from profit comparison: 25 kW PAT in the first case and 35 kW PAT in the second case. That happens because when comparing profits, the total costs of the installation are not taken into consideration.

The average LCOE from all PAT cases considered, is approximately 0.09 €/kWh. This value is in the range of 0.05 and 0.18 €/kWh, for PHS large-scale systems found in the literature by Zakeri and Syri [21], Mohsen Ibrahim Abd El-Rahman [48]. Considering now the PPs presented in Sections 5.2 and 5.3 for all PAT cases, we can observe that the system needs approximately 5 years to recoup the total investment. An average PP of 5 years for such a system is quite short, especially when compared to its lifespan of 25 years. This is explained by the fact that the annual profit provided by the system is quite high and when combined with the initial installation cost, a very short PP is achieved. Concluding, LCOE and PP indexes show that a micro-scale PHS system in combination with a PV installation, can provide electricity at a quite low total cost per kWh, compared with other methods of storage, such as batteries etc. [6,21].

6. Conclusions

In this work, a micro-scale PHS system has been suggested as energy storage for the AGH with PVs installed at its roof. Appropriate modelling of PV generation and demand throughout the year, allowed a good estimation of the excess generation available for storage. Since time-of-use tariffs exists in Greece, the extension of the pumping operation during the cheaper tariff was also investigated. PAT operation for PATs with different nominal power has been modelled for part load, both in pumping and generating mode. Such modeling of PATs in the economic assessment of PHS systems has not been previously presented. The simulation results of the overall system provided solid evidence that a micro-scale PHS system is a viable investment, if attention is paid in taking advantage of special properties of the installation in order to reduce installation costs (using the sea as the lower tank for PHS, covering the roof with PV etc.). The size of the PAT also plays pivotal role. Depending on the financial index used during decision, a different PAT size may qualify as the best choice. In the case of the AGH, it was proven that a 25 kW PAT is sufficient when LCOE or PP is considered, and 35 kW PAT is better if the profit is the decisive factor.

For the PHS system of the AGH, described in this paper, it was assumed an average upper reservoir volume of 2100 w.m. By increasing this volume, the PHS system's capacity is also increased and therefore, more water can be pumped and exploited through the day. A preliminary expansion of the system's capacity is possible, since a large amount of PV generation remains unexploited with the use of the 2100 q.m. tank. An alternative way to reduce the unexploited energy from PVs, after energy has already been stored through the PHS system, is the shift of hotel's energy-intensive processes (such as laundry, kitchens or water heating) to those hours during the day when this excess energy is available. Long-term, the collection of the rainwater to the upper reservoir would certainly improve PHS system's total energy efficiency. Greece is predominantly a rainy country, with big amounts of rainfalls throughout the year. The collection of this water would decrease the daily required water for fulfilling the upper tank and consequently the energy needed from the pump. The above-mentioned possible solutions of increasing the dimensions of the PHS system and exploiting the rainfall waters, in conjunction with the better dimensioning of the PV's installation and selection of the required equipment, will lead to a much better and more sustainable energy storage system for the AGH.

Author contributions: Conceptualization, PNV; methodology, DKK and PNV; software, DKK and AABD; validation, DKK, PNV and AABD; formal analysis, DKK, PNV and AABD; writing—original draft preparation, DKK, PNV and AABD; writing—review and editing, DKK, PNV and AABD; supervision, PNV. All authors have read and agreed to the published version of the manuscript.

Conflict of interest: The authors declare no conflict of interest.

Abbreviations

AGH	Average Greek Hotel
BEP	Best Efficiency Point
RES	Renewable Energy Sources
LCOE	Levelized Cost of Energy
LCOS	Levelized Cost of Storage
PP	Payback Period
PV	Photovoltaic
PVGIS	Photovoltaic Geographical Information System
PLC	Programmable Logic Controller
PAT	Pump As Turbine
PHS	Pumped Hydro Storage

References

1. Sahoo S, Timmann P. Energy Storage Technologies for Modern Power Systems: A Detailed Analysis of Functionalities, Potentials, and Impacts. IEEE Access. 2023; 11: 49689-49729. doi: 10.1109/access.2023.3274504
2. Boroomandnia A, Rismanchi B, Wu W, et al. Optimal design of micro pumped-storage plants in the heart of a city. Sustainable Cities and Society. 2024; 101: 105054. doi: 10.1016/j.scs.2023.105054
3. Statista Research Department. Pure pumped storage hydropower capacity worldwide from 2010 to 2023. Available online: https://www.statista.com/statistics/1304113/pumped-storage-hydropower-capacity-worldwide/ (accessed on 2 May 2024).
4. Boicea VA. Energy Storage Technologies: The Past and the Present. Proceedings of the IEEE. 2014; 102(11): 1777-1794. doi: 10.1109/jproc.2014.2359545
5. Li L, Wang B, Jiao K, et al. Comparative techno-economic analysis of large-scale renewable energy storage technologies. Energy and AI. 2023; 14: 100282. doi: 10.1016/j.egyai.2023.100282
6. Smallbone A, Jülch V, Wardle R, et al. Levelised Cost of Storage for Pumped Heat Energy Storage in comparison with other energy storage technologies. Energy Conversion and Management. 2017; 152: 221-228. doi: 10.1016/j.enconman.2017.09.047
7. Zeng X, Li J, Singh N. Recycling of Spent Lithium-Ion Battery: A Critical Review. Critical Reviews in Environmental Science and Technology. 2014; 44(10): 1129-1165. doi: 10.1080/10643389.2013.763578

8. Dobó Z, Dinh T, Kulcsár T. A review on recycling of spent lithium-ion batteries. Energy Reports. 2023; 9: 6362-6395. doi: 10.1016/j.egyr.2023.05.264
9. Guruprasad PSM, Quaranta E, Coronado-Hernández OE, et al. Hydropower Advantages over Batteries in Energy Storage of Off-Grid Systems. MDPI. doi: 10.20944/preprints202308.0300.v1
10. Bideris-Davos AA, Vovos PN. Comprehensive Review for Energy Recovery Technologies Used in Water Distribution Systems Considering Their Performance, Technical Challenges, and Economic Viability. Water. 2024; 16(15): 2129. doi: 10.3390/w16152129
11. Meirelles Lima G, Brentan BM, Luvizotto E. Optimal design of water supply networks using an energy recovery approach. Renewable Energy. 2018; 117: 404-413. doi: 10.1016/j.renene.2017.10.080
12. Pugliese F, Giugni M. An Operative Framework for the Optimal Selection of Centrifugal Pumps as Turbines (PATs) in Water Distribution Networks (WDNs). Water. 2022; 14(11): 1785. doi: 10.3390/w14111785
13. Pérez-Sánchez M, Sánchez-Romero FJ, Ramos HM, et al. Improved Planning of Energy Recovery in Water Systems Using a New Analytic Approach to PAT Performance Curves. Water. 2020; 12(2): 468. doi: 10.3390/w12020468
14. Barbarelli S, Amelio M, Florio G. Predictive model estimating the performances of centrifugal pumps used as turbines. Energy. 2016; 107: 103-121. doi: 10.1016/j.energy.2016.03.122
15. Venturini M, Manservigi L, Alvisi S, et al. Development of a physics-based model to predict the performance of pumps as turbines. Applied Energy. 2018; 231: 343-354. doi: 10.1016/j.apenergy.2018.09.054
16. Fecarotta O, McNabola A. Optimal Location of Pump as Turbines (PATs) in Water Distribution Networks to Recover Energy and Reduce Leakage. Water Resources Management. 2017; 31(15): 5043-5059. doi: 10.1007/s11269-017-1795-2
17. Nguyen KD, Duc Dai P, Quoc Vu D, et al. A MINLP Model for Optimal Localization of Pumps as Turbines in Water Distribution Systems Considering Power Generation Constraints. Water. 2020; 12(7): 1979. doi: 10.3390/w12071979
18. de Oliveira e Silva G, Hendrick P. Pumped hydro energy storage in buildings. Applied Energy. 2016; 179: 1242-1250. doi: 10.1016/j.apenergy.2016.07.046
19. Morabito A, Hendrick P. Pump as turbine applied to micro energy storage and smart water grids: A case study. Applied Energy. 2019; 241: 567-579. doi: 10.1016/j.apenergy.2019.03.018
20. Manolakos D, Papadakis G, Papantonis D, et al. A stand-alone photovoltaic power system for remote villages using pumped water energy storage. Energy. 2004; 29(1): 57-69. doi: 10.1016/j.energy.2003.08.008
21. Zakeri B, Syri S. Electrical energy storage systems: A comparative life cycle cost analysis. Renewable and Sustainable Energy Reviews. 2015; 42: 569-596. doi: 10.1016/j.rser.2014.10.011
22. Hellenic Chamber of hotels. e-Household Potential Greece 2022—Total Country (Greek). Available online: https://www.grhotels.gr/ksenodocheiako-dynamiko-elladas-2022-synolo-choras/ (accessed on 2 May 2024).
23. The Hellenic Parliament. Official Government Gazette. The Hellenic Parliament. 2015; 10(2): 31-48.
24. Hellenic Ministry of the Environment and Energy. Energy Audits of buildings, heating systems and air-conditioning systems, statistical analysis for the year 2020 (available in Greek). Ministry of the Environment and Energy; 2021.
25. Magro B, Borg SP. A Feasibility Study on CHP Systems for Hotels in the Maltese Islands: A Comparative Analysis Based on Hotels' Star Rating. Sustainability. 2023; 15(2): 1337. doi: 10.3390/su15021337
26. Provenzano M. Analysis of the energy consumption in the hotel sector and feasibility study for the installation of sofc-based cogeneration systems. Politecnico di Torino. 2021.
27. European Commission. Photovoltaic Geographical Information System. Available online: https://re.jrc.ec.europa.eu/pvg_tools/en/# (accessed on 2 May 2024).
28. Le Marre M, Mandin P, Lanoisellé JL, et al. Experimental study on performance predictions of pumps as turbine. Energy Conversion and Management. 2023; 292: 117235. doi: 10.1016/j.enconman.2023.117235
29. Bideris-Davos AA, Vovos PN. Co-optimization of power and water distribution systems for simultaneous hydropower generation and water pressure regulation. Energy Reports. 2024; 11: 3135-3148. doi: 10.1016/j.egyr.2024.02.041
30. Bideris-Davos AA, Vovos PN. Algorithm for Appropriate Design of Hydroelectric Turbines as Replacements for Pressure Reduction Valves in Water Distribution Systems. Water. 2023; 15(3): 554. doi: 10.3390/w15030554
31. Yang SS, Derakhshan S, Kong FY. Theoretical, numerical and experimental prediction of pump as turbine performance. Renewable Energy. 2012; 48: 507-513. doi: 10.1016/j.renene.2012.06.002
32. Pugliese F, Fontana N, Marini G, et al. Experimental assessment of the impact of number of stages on vertical axis multi-stage centrifugal PATs. Renewable Energy. 2021; 178: 891-903. doi: 10.1016/j.renene.2021.06.132

33. Rossi M, Nigro A, Renzi M. A predicting model of PaTs' performance in off-design operating conditions. Energy Procedia. 2019; 158: 123-128. doi: 10.1016/j.egypro.2019.01.056
34. Novara D, McNabola A. The Development of a Decision Support Software for the Design of Micro-Hydropower Schemes Utilizing a Pump as Turbine. EWaS3. 2018; 11: 678. doi: 10.3390/proceedings2110678
35. Public Power Corporation Group (PPC). For professionals & businesses with different consumption needs during the day than at night (Greece). Available online: https://www.dei.gr/el/gia-tin-epixeirisi/revma/epaggelmaties-epixeiriseis/g23/ (accessed on 2 May 2024).
36. Laghari JA, Mokhlis H, Bakar AHA, et al. A comprehensive overview of new designs in the hydraulic, electrical equipments and controllers of mini hydro power plants making it cost effective technology. Renewable and Sustainable Energy Reviews. 2013; 20: 279-293. doi: 10.1016/j.rser.2012.12.002
37. Tzouras T. Photovoltaic installation in an Industrial Unit with Net Metering (available in Greek). Available online: https://hdl.handle.net/10889/25640 (accessed on 2 May 2024).
38. CFI Team. Levelized Cost of Energy (LCOE). Available online: https://corporatefinanceinstitute.com/resources/valuation/levelized-cost-of-energy-lcoe/ (accessed on 2 May 2024).
39. Xenakis Energy. Financial Offer for the Installation of a Rooftop Photovoltaic System. Patras. 2023.
40. Siavelis D. Study on the Cost of the Construction of a Reservoir and on the Structural Reinforcement of a Building. Patras. 2023.
41. Alzohbi G. The cost of electromechanical equipment in a small hydro power storage plant. Journal of Energy Systems. 2018; 2(4): 238-259. doi: 10.30521/jes.457288
42. Novara D, Carravetta A, NcNabola A, Ramos H. Cost Model for Pumps as Turbines in Run-of-River and In-Pipe Microhydropower Applications. Journal of Water Resources Planning and Management. 2019; 145(5). doi: 10.1061/(ASCE)WR.1943-5452.0001063
43. Saidur R, Mekhilef S, Ali MB, et al. Applications of variable speed drive (VSD) in electrical motors energy savings. Renewable and Sustainable Energy Reviews. 2012; 16(1): 543-550. doi: 10.1016/j.rser.2011.08.020
44. Marini G, Di Menna F, Maio M, et al. HYPER: Computer-Assisted Optimal Pump-as-Turbine (PAT) Selection for Microhydropower Generation and Pressure Regulation in a Water Distribution Network (WDN). Water. 2023; 15(15): 2807. doi: 10.3390/w15152807
45. De Marchis M, Fontanazza CM, Freni G, et al. Energy Recovery in Water Distribution Networks. Implementation of Pumps as Turbine in a Dynamic Numerical Model. Procedia Engineering. 2014; 70: 439-448. doi: 10.1016/j.proeng.2014.02.049
46. Hammond C, Good R, Loge F. Economically Optimal Leak Management: Balancing Pressure Reduction, Energy Recovery, and Leak Detection and Repair. Journal of Water Resources Planning and Management. 2024; 150(8). doi: 10.1061/jwrmd5.wreng-6428
47. Tsagas I. Greece shuns net metering. PV Magazine. 2024.
48. Mohsen Ibrahim Abd El-Rahman M. Optimization of Renewable Energy-Based Smart Micro-Grid System. In: Modeling, Simulation and Optimization of Wind Farms and Hybrid Systems. IntechOpen; 2020. doi: 10.5772/intechopen.87093

Energy Storage and Conversion 2024, 2(3), 515.
https://doi.org/10.59400/esc.v2i3.515

Article

Heat transfer characteristics in Williamson fluid flow in a vertical channel with chemical reaction and entropy production

Amala Olkha, Mukesh Kumar*

Department of Mathematics, University of Rajasthan, Jaipur 302004, India
*** Corresponding author:** Mukesh Kumar, mukeshkumar2011992@gmail.com

CITATION

Olkha A, Kumar M. Heat transfer characteristics in Williamson fluid flow in a vertical channel with chemical reaction and entropy production. Energy Storage and Conversion. 2024; 2(3): 515. https://doi.org/10.59400/esc.v2i3.515

ARTICLE INFO

Received: 26 March 2024
Accepted: 21 June 2024
Available online: 1 July 2024

Abstract: This research endeavor investigates the natural convection flow of Williamson fluid in the region between two vertical parallel flat plates via a porous medium. Impacts of viscous dissipation, joule heating, exponential space, and thermal-dependent heat sources (ESHS/THS) are invoked. Mass transfer is also studied in accounting for chemical reaction impact. The governing non-linear PDEs are reduced to ODEs in non-dimensional form under adequate transformation relations. The numerical technique, namely, Runge-Kutta fourth-order, is utilized to tackle the problem with the shooting method. Additionally, second-law analysis is presented in terms of entropy production. The effects of numerous regulating parameters occurred in the problem relevant to flow, heat and mass transport, and entropy production are discussed via graphical mode of representation. Moreover, the quantities of physical significance are computed, displayed in graphical form, and discussed. For verification of acquired results, a comparison is also made using HPM with prior research, which was found to be in excellent agreement. It is concluded that the fluid temperature field enhances with upsurging values of pertinent parameters. The influence of the convective surface parameter and order of reaction are found to make augmentation in mass diffusion. Further, the effect of joule heating is noticed to increase the rate of heat transfer, while the reverse scenario is observed with upsurging values of heat source parameters. The influence of viscous dissipation is seen to increase entropy production.

Keywords: Williamson fluid; velocity slip; THS; ESHS; viscous dissipation; porous medium; joule heating; chemical reaction; entropy production; convective boundaries; HPM

1. Introduction

The channel flows are the fundamental configurations in fluid dynamics. The study of convection flow in channels has been a prominent field of research interest for its important engineering applications, e.g., in electrochemical processes, heat exchangers, solar energy collectors, fibrous insulation, and so forth. Several researchers have considered the natural convection problems of viscous fluids in the region between two vertical flat plates, including Bruce and Na [1], Aung et al. [2], Vajravelu and Sastri [3], Rajagopal and Na [4], Cheng et al. [5], Ziabakhsh and Domairry [6], Narahari and Dutta [7], Kargar and Akbarzade [8], Rashidi et al. [9], Hatami et al. [10], etc.

The overhead investigations were carried out for the clear fluid flows. None of these studies considered flow via a porous medium. In thermal-free convection via porous medium, the fluid flow is driven by buoyancy forces. These forces occur because of density variations due to temperature gradients in the fluid. The interest in the study of convection via porous medium is inspired by its significance in widespread practical and engineering applications, for example, solar power collectors, drying processes, heat removal in nuclear reactors, groundwater pollution, thermal insulation, etc. A considerable number of studies on convection flow problems of viscous fluids via porous medium in the region between two vertical parallel plates under the influence of Lorentz force have been reported by many researchers, such as Rapits et al. [11], Chamkha [12], Singh and Pathak [13], Das et al. [14], and many others. MHD flow continues to be of interest to researchers due to its wide range of practical applications in manufacturing processes, MHD power generators, astrophysical fluid dynamics, plasma aerodynamics, and geophysical fluid dynamics. Besides, in medical therapies like laparoscopic treatment, MHD with joule heating plays a significant role. In recent years, Asha and Sunitha [15], Swain et al. [16], Ramesh et al. [17], Ali et al. [18], etc. have examined the effects of MHD with joule heating.

Williamson fluid, a pseudoplastic non-Newtonian fluid, was introduced by Williamson [19]. The investigations of such fluid flows are significant because of their important practical applications, such as in the drawing of polymer sheets, the production of adhesives, photographic film production, and so on. Vasudev [20] investigated heat transport in the peristaltic flow of Williamson fluid in the region between horizontal parallel plates via a porous medium. Considering the impact of Lorentz force, the natural convection flow of Williamson fluid in the region between vertical parallel plates via porous medium was proposed by Subramanyam et al. [21]. Swaroopa and Prasad [22] proposed free convection Williamson flow in the region between parallel walls under consideration of radiation and Lorentz force impact. An analytical investigation of Williamson fluid-free convective flow in an upright channel with permeable walls, considering viscosity and radiation effects, was presented by Ajibade et al. [23]. Forced convection in Williamson flow via a porous medium was carried out by Qawasmeh et al. [24]. Pattanaik et al. [25] have analysed Williamson flow via porous medium in the existence of nanoparticles in a parallel plate channel due to thermal buoyancy, considering Lorentz force and radiation impacts. Usman et al. [26] have examined heat transport in Williamson fluid flow in a ciliated channel with permeable walls under the influence of Lorentz force via porous media.

In nature and industries, many transport processes occur where thermal and mass transport take place parallelly as a consequence of the joint buoyancy effects of thermal and species diffusion. The heat and mass transport phenomenon is also encountered in chemical process industries, for instance, polymer production and food processing. The occurrence of reactions and their order in such phenomena influence the performance and features of the product obtained. Grosan et al. [27] examined the impact of thermophoretic transport of particles in mixed convective heat and mass transport in a vertical parallel plate channel. Reaction influence on convection flow of power law fluid in the existence of porous medium, invoking heat and mass transport, was examined by Ibrahim et al. [28]. Uwanta and Hamza [29] discussed the impact of suction or injection on the exothermic reaction of Arrhenius kinetics, thermal diffusion, and the time-dependent convective flow of viscous Newtonian fluid in the region between two infinite upright parallel permeable plates. Prasannakumara et al. [30] studied reaction and radiation influence on Williamson fluid flow with nanoparticles in porous medium influenced by stretchy surfaces. Singh and Kumar [31] investigated heat and mass transmission in micropolar fluid flow in porous channels, considering chemical reactions with radiation influence. Mallikarjun et al. [32] analysed fully developed mixed convection flow in a vertical channel, considering heat production, absorption, and reactions of first order. Thermal and mass transport in the convective flow of Williamson fluid outside a cylinder via porous medium, under assumptions of the boundary layer, was investigated by Loganathan and Dhivya [33]. Huang [34] has examined thermal and mass transport in convective flow via porous medium along an inclined surface, considering Lorentz force influence. Nazir et al. [35] have considered surface chemical reactions in the flow of Walter's B fluid past a paraboloid, including heat and mass diffusion. Olkha and Kumar [36] have reported heat and mass transport in free convection flow of non-Newtonian fluid via porous medium in the region between two vertical cylinders, considering chemical reaction impact. Olkha and Kumar [37] have also investigated melting heat transport in non-Newtonian fluid flow via porous medium produced by a curved surface stretching non-linearly, including mass transport and reaction influence.

The consideration of convective boundary conditions in heat transport problems is significant in engineering processes, e.g., thermal energy storage, gas turbines, nuclear plants, and so forth. Srinivas et al. [38] studied thermal and mass diffusion in the pulsating flow of viscous Newtonian fluid in a horizontal channel via porous medium, considering slip flow and convective boundary constraints, including Lorentz force and chemical reaction. Oyelakin et al. [39] employed convective surface boundary conditions, including velocity slip in time-dependent non-Newtonian flow in the existence of nanoparticles including influence of heat transport characteristics. Such constraints on the convection slip flow of Williamson fluid produced by a stretchy surface, considering Lorentz force and Joule heating, were employed by Sharada and Shankar [40]. Zeeshan et al. [41] explored the radiative Couette-Poiseuille flow of nanofluid in a channel with chemical reactions considering convective boundaries, Joule heating, activation energy, and viscous dissipation. Convective boundary conditions to discuss heat transport in the flow of Casson fluid in the region between inclined permeable parallel plates, invoking the impacts of flow-thermal properties, were considered by Neeraja et al. [42]. Jagadeesh and Reddy [43] have employed convective boundary conditions in 3-D convection non-Newtonian couple stress flow in the existence of nanoparticles influenced by a stretchable sheet, considering Lorentz force, radiation, and reaction.

The exponential space-dependent heat source procedure is probably more suited for excellent thermal processes since a minor size augmentation of the heat source leads to a significant improvement in the thermal field. Several researchers have considered exponential space- and thermal-dependent heat sources (ESHS/THS) in their studies conducted on viscous Newtonian and non-Newtonian fluid flows in various aspects, including Zaigham Zia et al. [44], Thriveni et al. [45], Mahanthesh et al. [46], Nagaraja and Gireesha [47], Swain et al. [48], Hasibi et al. [49], Sharma et al. [50], etc.

Entropy, a key thermodynamic irreversibility parameter, occurs in the second law of thermodynamics. The analysis of entropy production makes a significant contribution to thermal systems design decisions and thus supports optimization of cost and energy in science and engineering areas like the cooling of electronic devices, heat exchangers, energy storage systems (Yessef et al. [51], Chojaa et al. [52], Loulijat et al. [53], and Hamid et al. [54]), etc. Bejan [55,56] presented pioneering work on entropy production and its optimization. Baytas [57] analysed entropy production in free convection via porous medium along with thermal transport and mass transport in a tilted permeable enclosure. Makinde and Eegunjobi [58] proposed the rate of entropy and Bejan number in viscous couple stress flow in an upright channel filled with porous material in the existence of buoyancy forces. Das et al. [59] examined entropy production in pseudo-plastic fluid flow in the existence of nanoparticles in a channel having permeable walls under convective heating. Analysis of heat transport in natural convection and entropy production inside a channel including a permeable plate mounted at the lower wall was performed numerically by Maskaniyan et al. [60]. Yusuf et al. [61] examined the entropy production number in the bioconvective flow of pseudoplastic fluid in the existence of nanoparticles along an aligned semi-infinite porous plate under convective boundaries, considering magnetic field, Joule heating, viscous dissipation, and chemical reaction. Olkha and Dadheech [62] numerically analysed entropy production in the flow of three different fluids (Williamson fluid, Casson fluid, and viscous fluid) produced by a permeable stretching sheet. Entropy production in the free convection of nanofluid via porous medium in a square configuration including heated corners, in the existence of Lorentz force, has been discussed by Reddy et al. [63]. Entropy production in Jeffery fluid flow in tilted permeable pipe via porous medium applying convective boundary constraints in the existence of an applied magnetic field has been investigated by Raje et al. [64]. In natural and forced convection slip flow in the region between vertical parallel permeable plates, entropy production has been discussed by Balamurugan et al. [65].

In view of the aforementioned studies, this work investigates gravity-driven Williamson fluid flow in the region bounded by two vertical parallel flat plates under convective surface boundary constraints. Slip flow is considered a porous medium under Lorentz force impact. In heat transport analysis, viscous dissipation, joule heating, and non-uniform heat source contributions are accounted for. Mass transport is also discussed in light of the existence of the reaction effect. Apart from that, second-law analysis is invoked in the study in terms of entropy production, which completes the heat transport analysis. The Runge-Kutta 4th order technique is employed for numerical simulations on MATLAB. Additionally, the influence of pertinent parameters on wall shear stress, rate of heat transport, and mass transport rate is exhibited in a graphical way and discussed. A comparison of the results obtained with previously published data shows an excellent match.

2. Problem formulation

We consider the fully developed, steady flow of an incompressible Williamson fluid in the region bounded by two vertical, infinitely parallel flat plates situated at a distance h apart (as **Figure 1** depicts). We choose $x-$axis parallel to the flow, opposite to the gravitational field, and $y-$ axis is considered perpendicular to it. The fluid flow is considered via porous medium, and a uniform magnetic field B_0 is applied in the perpendicular direction of flow. Convective boundary constraints relevant to heat and concentration are applied at the channel walls along with velocity slip. Moreover, the impacts of viscous dissipation, exponential space-and thermal-dependent heat sources, joule heating, and higher-order chemical reactions are accounted for. A cartesian coordinate system is considered. The plates are assumed of infinite length in $x-$ and $z-$directions, all physical quantities are, therefore, treated as functions of y only.

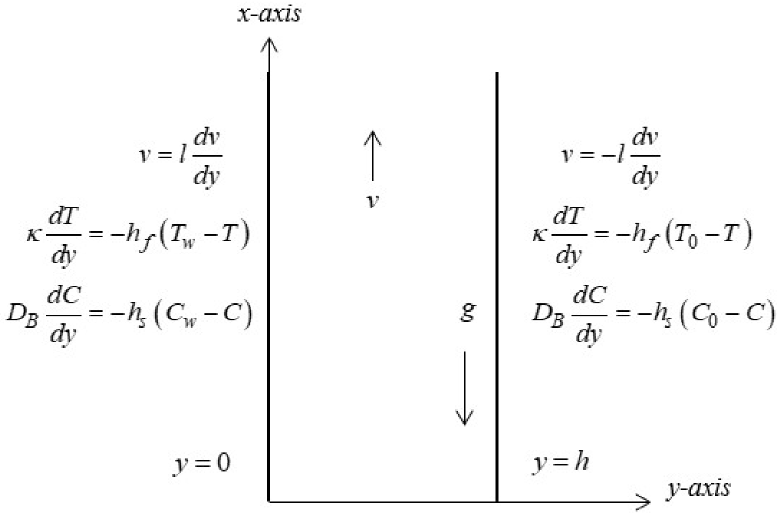

Figure 1. Systematic diagram for present problem.

With the aforementioned considerations, the regulating equations are

$$\mu\frac{d^2v}{dy^2} + \frac{\mu\Gamma}{\sqrt{2}}\frac{d}{dy}\left\{\left(\frac{dv}{dy}\right)^2\right\} + \rho g[\beta_T(T - T_0) + \beta_C(C - C_0)] - \frac{\mu}{K_p}v - \sigma B_0^2 v = 0 \tag{1}$$

$$\kappa\frac{d^2T}{dy^2} + \mu\left[1 + \frac{\Gamma}{\sqrt{2}}\frac{dv}{dy}\right]\left(\frac{dv}{dy}\right)^2 + Q_T^*(T - T_0) + Q_E^*(T_w - T_0) \times p\left(-\frac{y}{h}\right) + \sigma B_0^2 v^2 = 0 \tag{2}$$

$$D_B\frac{d^2C}{dy^2} - k_n(C - C_0)^n = 0 \tag{3}$$

and the relevant boundary constraints are considered as

$$\begin{aligned} &at\ y = 0: v = l\,\frac{dv}{dy}, \kappa\,\frac{dT}{dy} = -h_f(T_w - T), D_B\frac{dC}{dy} = -h_s(C_w - C), \\ &at\ y = h: v = -l\,\frac{dv}{dy}, \kappa\,\frac{dT}{dy} = -h_f(T_0 - T), D_B\frac{dC}{dy} = -h_s(C_0 - C), \end{aligned} \tag{4}$$

where v is the axial velocity of the fluid, T is the temperature of the fluid, T_0 is the temperature of the right wall, C is the concentration of the fluid, μ is the viscosity, ρ is the density, Γ is the time constant, β_T is the coefficient of thermal expansion, β_C is the coefficient of mass expansion, C_0 is the concentration at the right wall, σ is the electrical conductivity, B_0 is strength of magnetic field, K_p is the permeability of the porous medium, κ is the thermal conductivity, U is the reference velocity, h_f is the convective heat transfer coefficient, h_s is the convective mass transfer coefficient, D_B is diffusion coefficient, ${Q_T}^*$ is the thermal based heat source coefficient, ${Q_E}^*$ is the exponential heat source coefficient, T_w is temperature of left wall, C_w is the concentration at the left wall.

Invoking the following non-dimensional quantities

$$V = \frac{v}{U}, \eta = \frac{y}{h}, \theta = \frac{T - T_0}{T_w - T_0}, \phi = \frac{C - C_0}{C_w - C_0} \tag{5}$$

Equations (1)–(3) reduce to following non-dimensional form,

$$\frac{d^2V}{d\eta^2} + We\frac{dV}{d\eta}\frac{d^2V}{d\eta^2} + \frac{Gr}{Re}\theta + \frac{Gc}{Re}\phi - D\,V - Ha^2V = 0 \tag{6}$$

$$\frac{d^2\theta}{d\eta^2} + Br\left[1 + \frac{We}{2}\frac{dV}{d\eta}\right]\left(\frac{dV}{d\eta}\right)^2 + Q_T\theta + Q_E\,exp(-\eta) + Ha^2Br\,V^2 = 0 \tag{7}$$

$$\frac{d^2\phi}{d\eta^2} - ScK_n\phi^n = 0 \tag{8}$$

and the corresponding boundary conditions in non-dimensional form are:

$$\begin{aligned} &V = L\frac{dV}{d\eta}, \theta = 1 + \frac{1}{Bi_1}\frac{d\theta}{d\eta}, \phi = 1 + \frac{1}{Bi_2}\frac{d\phi}{d\eta}, at\ \eta = 0 \\ &V = -L\frac{dV}{d\eta}, \theta = \frac{1}{Bi_1}\frac{d\theta}{d\eta}, \phi = \frac{1}{Bi_2}\frac{d\phi}{d\eta}, at\ \eta = 1 \end{aligned} \tag{9}$$

where, $We = \sqrt{2}\Gamma U/h$ is the non-Newtonian parameter, $Br = \mu U^2/\kappa(T_w - T_0)$ is the Brinkman number, $Q_T = {Q_T}^*h^2/\kappa$ is the THS parameter, $Q_E = {Q_E}^*h^2/\kappa$ is the ESHS parameter, $Ha = B_0h\sqrt{\sigma/\mu}$ is the Hartman number, $D = h^2/K_p$ is the porous medium parameter,$Gr = g\beta_T(T_w - T_0)h^3/v^2$ is the thermal Grashof number, $Gc = g\beta_C(C_w - C_0)h^3/v^2$ is the solutal Grashof number, $Re = Uh/v$ is Reynolds number, $Sc = v/D_B$ is the Schmidt number, $K_n = k_n(C_w - C_0)^{n-1}h^2/v$ is the chemical reaction parameter, $L = l/h$ is the velocity slip parameter, $Bi_1 = hh_f/\kappa$ is thermal Biot number, $Bi_2 = hh_s/D_B$ is the solutal Biot number.

3. Quantities of physical significance

The quantities of physical importance (skin-friction coefficient, Nusselt number, and Sherwood number) respectively, given by

$$C_f = \frac{\tau_w}{\mu\,U/h}, Nu = \frac{hq_w}{\kappa(T_w - T_0)}\ and\ Sh = \frac{hj_w}{D_B(C_w - C_0)} \tag{10}$$

where shear stress (τ_w), heat flux (q_w), and mass flux (j_w) are given by

$$\tau_w = \mu\left\{\frac{\partial v}{\partial y} + \frac{\Gamma}{\sqrt{2}}\left(\frac{\partial v}{\partial y}\right)^2\right\}_{y=0}, q_w = -\left(\kappa\frac{\partial T}{\partial y}\right)_{y=0}, j_w = -D_B\left(\frac{\partial C}{\partial y}\right)_{y=0} \tag{11}$$

On substituting values from Equation (11) and Equation (5) into Equation (10), the obtained non-dimensional expressions are as follows:

$$C_f = \left[\frac{dV}{d\eta} + \frac{We}{2}\left(\frac{dV}{d\eta}\right)^2\right]_{\eta=0}, Nu = -\left(\frac{d\theta}{d\eta}\right)_{\eta=0}, Sh = -\left(\frac{d\phi}{d\eta}\right)_{\eta=0} \tag{12}$$

4. Entropy generation

The dimensional entropy production for the current problem is given as

$$S_{gen} = \frac{\kappa}{{T_0}^2}\left(\frac{dT}{dy}\right)^2 + \left[\frac{RD}{C_0}\left(\frac{dC}{dy}\right)^2 + \frac{RD}{T_0}\left(\frac{dC}{dy}\frac{dT}{dy}\right)\right] + \frac{\mu}{T_0}\left[1 + \frac{\Gamma}{\sqrt{2}}\frac{du}{dy}\right] + \frac{1}{T_0}\frac{\mu}{k_p}u^2 + \frac{1}{T_0}\sigma{B_0}^2u^2 \tag{13}$$

where the terms on right side in Equation (13) are entropy contributions due to heat transport, mass transport, viscous dissipation, porous medium, and magnetic field respectively.

The non-dimensional entropy generation (NS) is defined as

$NS = \frac{S_{gen}}{S_0}$, where $S_0 = \frac{\kappa(T_w - T_0)^2}{{T_0}^2 h^2}$

Thus, the non-dimensional entropy production (NS) is expressed as

$$\begin{aligned} NS &= \left(\frac{d\theta}{d\eta}\right)^2 + \frac{\Omega_C}{\Omega_T}\phi_C\left[\frac{\Omega_C}{\Omega_T}\left(\frac{d\phi}{d\eta}\right)^2 + \frac{d\theta}{d\eta}\frac{d\phi}{d\eta}\right] + \frac{Br}{\Omega_T}\left[\left(1 + \frac{We}{2}\frac{dV}{d\eta}\right)\left(\frac{dV}{d\eta}\right)^2 + (Ha)^2V^2 + DV^2\right] \\ &= S_T + S_C + S_f + S_M + S_P \end{aligned} \tag{14}$$

where,

$S_T = \left(\frac{d\theta}{d\eta}\right)^2$, $S_C = \frac{\Omega_C}{\Omega_T}\phi_C\left[\frac{\Omega_C}{\Omega_T}\left(\frac{d\phi}{d\eta}\right)^2 + \frac{d\theta}{d\eta}\frac{d\phi}{d\eta}\right]$, $S_f = \frac{Br}{\Omega_T}\left(1 + \frac{We}{2}\frac{dV}{d\eta}\right)\left(\frac{dV}{d\eta}\right)^2$, $S_M = (Ha)^2V^2$, and $S_P = DV^2$ represent the irreversibility corresponding to heat transfer, mass transfer, viscous dissipation in porous medium, and magnetic field, respectively. $\Omega_T = (T_w - T_0)/T_0$ represent the temperature difference parameter, $\Omega_C = (C_w - C_0)/C_0$ represent the concentration difference parameter, $\phi_C = RDC_0/\kappa$ represent the diffusion parameter.

5. Numerical methodology

The Runge-Kutta fourth-order method with a shooting approach is utilized to tackle the system of nonlinear ODEs (6)-(8) numerically under the boundary conditions (9). Non-linear ODEs (6)-(8) including boundary constraints (9), are initially transformed into simultaneous nonlinear DEs of first order; they are then further changed into an initial value problem by applying the shooting approach.

$$\left(V, \frac{dV}{d\eta}, \theta, \frac{d\theta}{d\eta}, \phi, \frac{d\phi}{d\eta}\right) = (y_1, y_2, y_3, y_4, y_5, y_6) \tag{15}$$

$$\frac{dy_1}{d\eta} = y_2, \frac{dy_3}{d\eta} = y_4, \frac{dy_5}{d\eta} = y_6 \tag{16}$$

$$\frac{dy_2}{d\eta} = -\frac{\frac{Gr}{Re}y_3 + \frac{Gc}{Re}y_5 - Dy_1 - (Ha)^2y_1}{1 + We\, y_2} \tag{17}$$

$$\frac{dy_4}{d\eta} = -Br\left(1 + \frac{We}{2}y_2\right){y_2}^2 - Q_T\, y_3 - Q_E\, exp(-\eta) - (Ha)^2Br\, {y_1}^2 \tag{18}$$

$$\frac{dy_6}{d\eta} = ScK_n(y_5)^n \tag{19}$$

The boundary conditions are as follows:

$$\begin{aligned} y_1(0) = Ly_2(0), y_2(0) = \alpha_1, y_3(0) = 1 + \frac{1}{Bi_1}y_4(0), y_4(0) = \alpha_2, y_5(0) = 1 + \frac{1}{Bi_2}y_6(0), y_6(0) = \alpha_3, y_1(1) \\ = -Ly_2(0), y_3(1) = \frac{1}{Bi_1}y_4(1), y_5(1) = \frac{1}{Bi_2}y_6(1) \end{aligned} \tag{20}$$

where, α_1, α_2, and α_3 are the initial guesses.

6. Homotopy perturbation method

We use He's homotopy perturbation approach [66–68] to solve the presented problem analytically. According to HPM, the differential Equations (6)–(8) satisfied by $f(\eta)$, $\theta(\eta)$ and $\phi(\eta)$ are separated into two parts, the linear component $\mathscr{L}(f)$, $\mathscr{L}(\theta)$, and $\mathscr{L}(\phi)$ and the non-linear component $\mathcal{N}(f)$, $\mathcal{N}(\theta)$, and $\mathcal{N}(\phi)$ and may be expressed as follows:

$$\mathscr{L}(f) + \mathscr{N}(f) - g(\eta) = 0 \tag{21}$$

$$\mathscr{L}(\theta) + \mathscr{N}(\theta) - h(\eta) = 0 \tag{22}$$

$$\mathscr{L}(\phi) + \mathscr{N}(\phi) - I(\eta) = 0 \tag{23}$$

where $\mathscr{L}(V) = \frac{d^2V}{d\eta^2}$, $\mathscr{L}(\theta) = \frac{d^2\theta}{d\eta^2}$, $\mathscr{L}(\phi) = \frac{d^2\phi}{d\eta^2}$

$\mathscr{N}(V) = We\,\frac{dV}{d\eta}\frac{d^2V}{d\eta^2} + \frac{Gr}{Re}\theta + \frac{Gc}{Re}\phi - D\,V - Ha^2V$,

$\mathscr{N}(\theta) = Br\left[1 + \frac{We}{2}\frac{dV}{d\eta}\right]\left(\frac{dV}{d\eta}\right)^2 + Q_T\,\theta + Q_E\,exp(-\eta) + Ha^2Br\,V^2$,

$\mathscr{N}(\phi) = -ScK_n\phi^n$, $g(\eta) = 0$, $h(\eta) = 0$, and $I(\eta) = 0$. With the homotopy technique, we create a homotopy $\overline{V}(\eta, p){:}\,\Omega \times [0,1] \to \mathbb{R}$, $\overline{\theta}(\eta, p){:}\,\Omega \times [0,1] \to \mathbb{R}$, and $\overline{\phi}(\eta, p){:}\,\Omega \times [0,1] \to \mathbb{R}$ which satisfies the following equation

$$(1-p)\left[\mathscr{L}(\overline{V}) - \mathscr{L}(u_0)\right] + p\left[\mathscr{L}(\overline{V}) + \mathscr{N}(\overline{V}) - g(\eta)\right] = 0, \qquad p \in [0,1] \tag{24}$$

$$(1-p)\left[\mathscr{L}(\overline{\theta}) - \mathscr{L}(\theta_0)\right] + p\left[\mathscr{L}(\overline{\theta}) + \mathscr{N}(\overline{\theta}) - h(\eta)\right] = 0, \qquad p \in [0,1] \tag{25}$$

$$(1-p)\left[\mathscr{L}(\overline{\phi}) - \mathscr{L}(\phi_0)\right] + p\left[\mathscr{L}(\overline{\phi}) + \mathscr{N}(\overline{\phi}) - I(\eta)\right] = 0, \qquad p \in [0,1] \tag{26}$$

Equations (24)–(26) can be written as

$$(1-p)\frac{d^2V}{d\eta^2} + p\left(\frac{d^2V}{d\eta^2} + We\,\frac{dV}{d\eta}\frac{d^2V}{d\eta^2} + \frac{Gr}{Re}\theta + \frac{Gc}{Re}\phi - D \times V - Ha^2V\right) = 0 \tag{27}$$

$$(1-p)\frac{d^2\theta}{d\eta^2} + p\left(\frac{d^2\theta}{d\eta^2} + Br\left[1 + \frac{We}{2}\frac{dV}{d\eta}\right]\left(\frac{dV}{d\eta}\right)^2 + Q_T\,\theta + Q_E\,exp(-\eta) + Ha^2Br \times V^2\right) = 0 \tag{28}$$

$$(1-p)\frac{d^2\phi}{d\eta^2} + p\left(\frac{d^2\phi}{d\eta^2} - ScK_n\phi^n\right) = 0 \tag{29}$$

In Equations (24)–(26), p is an embedding parameter, u_0, θ_0 and ϕ_0 is an initial guess, which satisfies the boundary conditions (9). It can be consider the solutions of the Equations (24)–(26) as a power series in p as follows:

$$\overline{V}(\eta, p) = \sum_{k=0}^{\infty} v_k(\eta)\,p^k \tag{30}$$

$$\overline{\theta}(\eta, p) = \sum_{k=0}^{\infty} \theta_k(\eta)\,p^k \tag{31}$$

$$\overline{\phi}(\eta, p) = \sum_{k=0}^{\infty} \phi_k(\eta)\,p^k \tag{32}$$

where v_k, θ_k, ϕ_k are unknown function of η. The approximate solutions (by taking $p \to 1$) are given by

$$V(\eta) = \overline{V}(\eta, 1) = \sum_{k=0}^{\infty} v_k(\eta) \tag{33}$$

$$\theta(\eta) = \overline{\theta}(\eta, 1) = \sum_{k=0}^{\infty} \theta_k(\eta) \tag{34}$$

$$\phi(\eta) = \overline{\phi}(\eta, 1) = \sum_{k=0}^{\infty} \phi_k(\eta) \tag{35}$$

using the Equations (9), (30)–(32) into Equations (24)–(26), equating the coefficients of like powers of p, we get

$$
\begin{aligned}
&p^0: \frac{d^2 v_0}{d\eta^2} = 0, v_0(0) = L\,\frac{dv_0(0)}{d\eta}, v_0(1) = -L\,\frac{dv_0(1)}{d\eta} \\
&\frac{d^2\theta_0}{d\eta^2} = 0, \theta_0(0) = 1 + \frac{1}{Bi_1}\frac{d\theta_0(0)}{d\eta}, \theta_0(1) = \frac{1}{Bi_1}\frac{d\theta_0(1)}{d\eta} \\
&\frac{d^2\phi_0}{d\eta^2} = 0, \phi_0(0) = 1 + \frac{1}{Bi_2}\frac{d\phi_0(0)}{d\eta}, \phi_0(1) = \frac{1}{Bi_2}\frac{d\phi_0(1)}{d\eta}
\end{aligned}
\tag{36}
$$

$$
\begin{aligned}
&p^1: \frac{d^2 v_1}{d\eta^2} + We\frac{dv_0}{d\eta}\frac{d^2 v_0}{d\eta^2} + \frac{Gr}{Re}\theta_0 + \frac{Gc}{Re}\phi_0 - (D + Ha^2)v_0 = 0\,, \\
&v_1(0) = L\frac{dv_1(0)}{d\eta}, v_1(1) = -L\frac{dv_1(1)}{d\eta} \\
&\frac{d^2\theta_1}{d\eta^2} + Br\left(1 + \frac{We}{2}\frac{dv_0}{d\eta}\right)\left(\frac{dv_0}{d\eta}\right)^2 + Q_T\theta_0 + Q_E e^{-\eta} + Ha^2 Br v_0^2 = 0, \\
&\theta_1(0) = \frac{1}{Bi_1}\frac{d\theta_1(0)}{d\eta}, \theta_1(1) = \frac{1}{Bi_1}\frac{d\theta_1(1)}{d\eta} \\
&\frac{d^2\phi_1}{d\eta^2} - ScK_n\phi_0^n = 0, \phi_1(0) = \frac{1}{Bi_2}\frac{d\phi_1(0)}{d\eta}, \phi_1(1) = \frac{1}{Bi_2}\frac{d\phi_1(1)}{d\eta}
\end{aligned}
\tag{37}
$$

$$
\begin{aligned}
&p^2: \frac{d^2 v_2}{d\eta^2} + We\left(\frac{dv_0}{d\eta}\frac{d^2 v_1}{d\eta^2} + \frac{dv_1}{d\eta}\frac{d^2 v_0}{d\eta^2}\right) + \frac{Gr}{Re}\theta_1 + \frac{Gc}{Re}\phi_1 - (D + Ha^2)v_1 = 0\,, \\
&v_2(0) = L\frac{dv_2(0)}{d\eta}, v_2(1) = -L\frac{dv_2(1)}{d\eta} \\
&\frac{d^2\theta_2}{d\eta^2} + Br\left(2 + \frac{3}{2}We\frac{dv_0}{d\eta}\right)\frac{dv_0}{d\eta}\frac{dv_1}{d\eta} + Q_T\theta_1 + 2Ha^2 Br v_0 v_1 = 0, \\
&\theta_2(0) = \frac{1}{Bi_1}\frac{d\theta_2(0)}{d\eta}, \theta_2(1) = \frac{1}{Bi_1}\frac{d\theta_2(1)}{d\eta} \\
&\frac{d^2\phi_2}{d\eta^2} - nScK_n\phi_0^{n-1}\phi_1 = 0, \phi_2(0) = \frac{1}{Bi_2}\frac{d\phi_2(0)}{d\eta}, \phi_2(1) = \frac{1}{Bi_2}\frac{d\phi_2(1)}{d\eta}
\end{aligned}
\tag{38}
$$

Similarly, we can obtain other coefficients with the help of MATLAB software. Solving these linear ordinary differential equations using corresponding boundary conditions with the help of MATLAB and substituting in the Equations (33)–(35), we can find homotopy perturbation solutions for various values of parameters.

7. Results and discussion

In this section, various graphs are drawn to display the effects of various parameters that occurred in the problem. Throughout the numerical computations, we considered $Gr = 1$, $Ha = 0.3$, $D = 0.5$, $Br = 2$, $Q_T = 0.2$, $Q_E = 0.2$, $Re = 1$, $Sc = 0.5$, $K_n = 0.5$, $n = 2$, $L = 0.1$, $Gc = 1$, $Bi_1 = 100$, and $Bi_2 = 100$, as fixed. The MATLAB based RK-4th order technique is utilized to tackle the system of regulating Equations (6)–(8) along with boundary constraints (9). For the validity of the results obtained, a comparison is made with previously reported studies by Singh and Paul [69] and Ajibade et al. [23], as presented in **Table 1**. The validity of the study's findings is confirmed by a high level of agreement between the two sets of data.

Table 1. Comparison for $V(\eta)$ and $\theta(\eta)$ when $Re = Gr = 1.0$ and values of other parameters are taken zero.

η	**Singh and Paul [69]**		**Ajibade et al. [23]**		**Present study**			
					RK 4		**HPM**	
	$V(\eta)$	$\theta(\eta)$	$V(\eta)$	$\theta(\eta)$	$V(\eta)$	$\theta(\eta)$	$V(\eta)$	$\theta(\eta)$
0					0	1	0	1
0.1	0.02850	0.900	0.02819	0.900	0.02850	0.900	0.02850	0.900
0.2					0.04800	0.800	0.04800	0.800
0.3	0.05950	0.700	0.05916	0.700	0.05950	0.700	0.05950	0.700
0.4					0.06400	0.600	0.06400	0.600
0.5	0.06250	0.500	0.06238	0.500	0.06250	0.500	0.06250	0.500
0.6					0.05600	0.400	0.05600	0.400
0.7	0.04550	0.300	0.04553	0.300	0.04550	0.300	0.04550	0.300
0.8					0.03200	0.200	0.03200	0.200
0.9	0.01650	0.100	0.01653	0.100	0.01650	0.100	0.01650	0.100
1.0					0	0	0	0

Figures 2–10 show the impacts of various pertinent parameters such as thermal Grashof number (Gr), mass Grashof number (Gc), Reynolds number (Re), non-Newtonian fluid (Williamson fluid) parameter (We), Hartmann number (Ha), porous medium parameter (D), velocity slip parameter (L), chemical reaction parameter (K_n), thermal Biot number (Bi_1), solutal Biot number (Bi_2), Schmidt number (Sc), exponential space (Q_E) -and thermal-dependent (Q_T) heat source parameters, Brinkman number (Br), temperature difference parameter (Ω_T), concentration difference parameter (Ω_C), and diffusion parameter (ϕ_C) on fluid flow, thermal, and concentration fields.

The effects of D and Ha on the velocity distribution $V(\eta)$ are exhibited in **Figure 2**. It is observed, from this figure, $V(\eta)$ lessens with upsurge in the value parameter D. The reason behind this is that raising the porous medium parameter (or decreasing permeability) Darcy resistance which opposes the flow upsurges. Fluid flow also lowers with augmentation in Ha parameter value. An increase in Ha value results in increase of Lorentz force, which acts in a transverse direction. Hence, the flow field shrinks with the upsurging value of the parameter Ha.

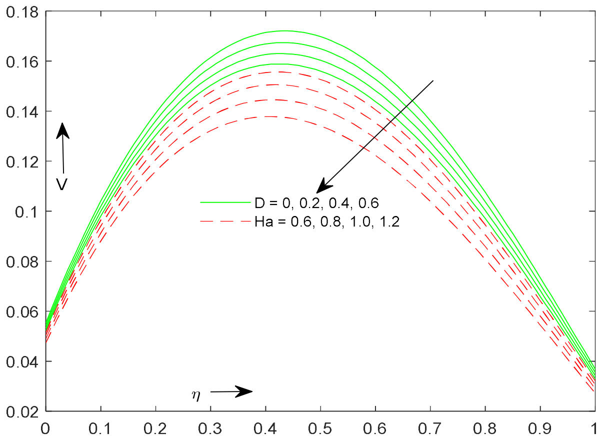

Figure 2. Velocity variation for D and Ha.

The impacts of Gr and Gc on fluid velocity $V(\eta)$ are displayed in **Figure 3**. We concluded, $V(\eta)$ enhances for increasing values of Gr and Gc because a greater Grashof number conveys a larger buoyancy force, which causes upsurge in velocity field.

Figure 4 illustrates the impact of Br and L on pace of the flow. With rising values of Br and L, fluid velocity $V(\eta)$ is found to grow. Upsurge in value of Br makes enhancement in viscous heating, which raises fluid kinetic energy and hence the pace of the flow improves. As the flow slip parameter (L) rises, the flow in the channel increases, and the effect is more apparent in the middle portion of the channel.

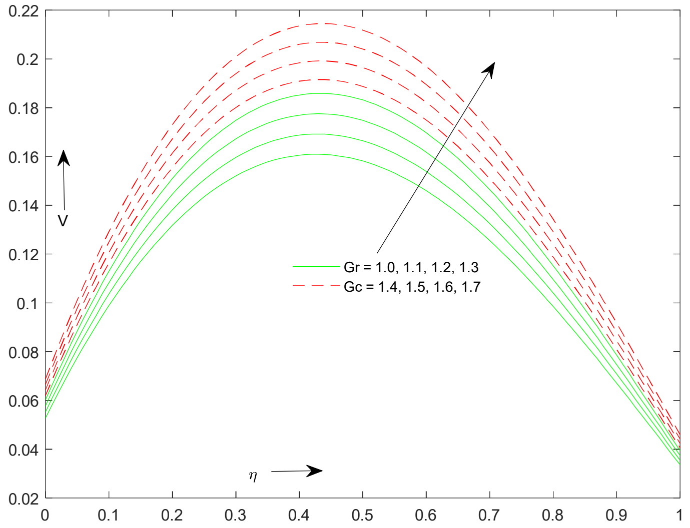

Figure 3. Velocity variation for Gr and Gc.

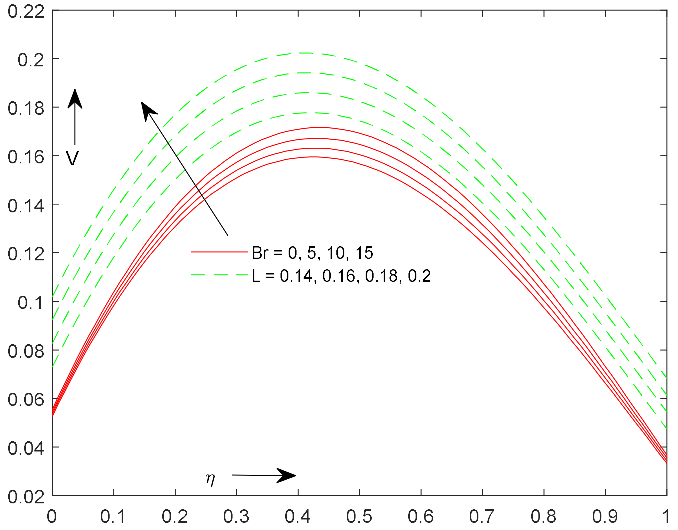

Figure 4. Velocity variation for L and Br.

Figure 5 depicts the impact of Re and We on velocity distribution. It is found that $V(\eta)$ lessens with rising value of Re. The impact of the Williamson parameter is also observed to shrink the velocity field. Physically, an upsurge in We parameter value implies an increase in stress relaxation time, which causes a reduction in fluid flow and thus lowers the velocity profile. The effect is prominent in almost half of the lower portion of the channel.

Figure 6 depicts the impacts of rising THS parameter and ESHS parameter values, i.e., Q_T and Q_E on the pace of the flow. The figure reveals that with a rise in the values of Q_T and Q_E fluid velocity increases. It may happen due to the higher kinetic energy of fluid molecules.

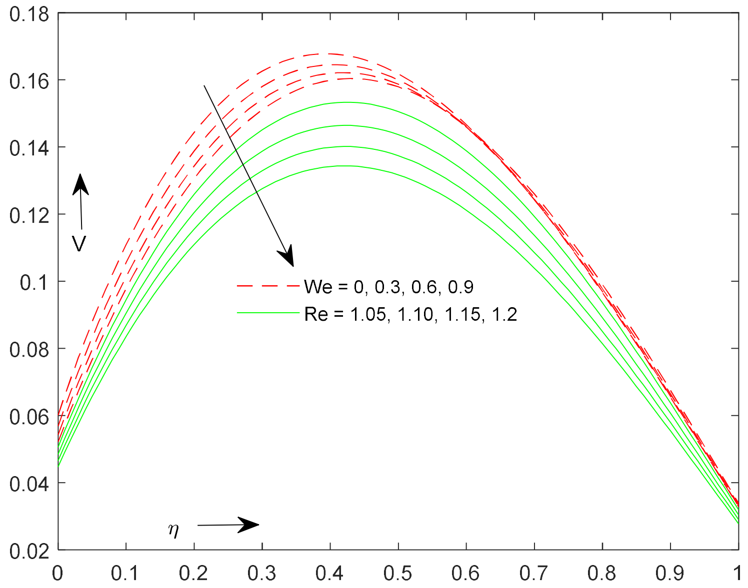

Figure 5. Velocity variation for We and Re.

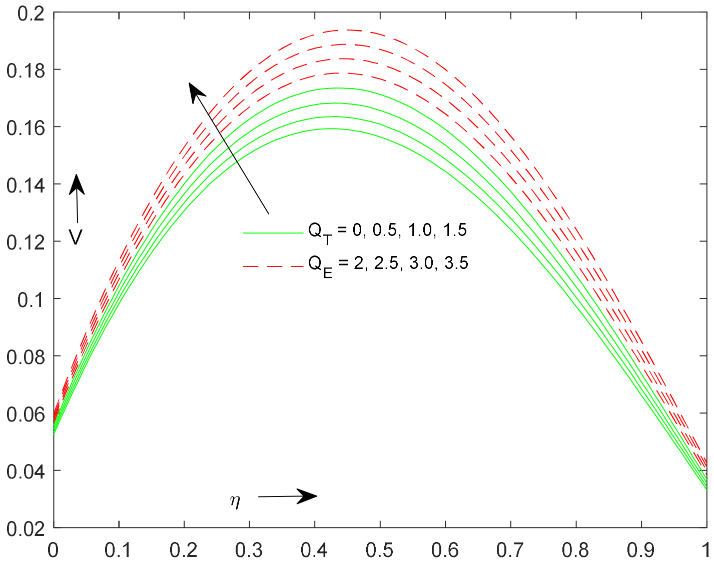

Figure 6. Velocity variation for Q_T and Q_E.

The effect of the THS and ESHS parameters i.e., (Q_T, and Q_E) on the energy profile $\theta(\eta)$ is exhibited in **Figure 7**. This graphical representation shows that when the value of Q_T and Q_E grows, the temperature profile improves because heat production improves as the values of heat source parameters (Q_T, and Q_E) increase.

Figure 8 reveals the effect of ascending Br and Bi_1 values on the temperature distribution $\theta(\eta)$. The figure displays that fluid temperature $\theta(\eta)$ increases with upsurging the values of Br and Bi_1. Physically, an increase in Brinkman number value enhances viscous heating, which causes an augmentation in fluid flow temperature and thus the magnifies thermal profile. Thermal Biot number Bi_1 involves heat transfer coefficient. $Bi_1 = 0$, i.e., there is no heat transfer, and $Bi_1 > 0$ means heat transfer rate increases, which causes an increase in the temperature profile.

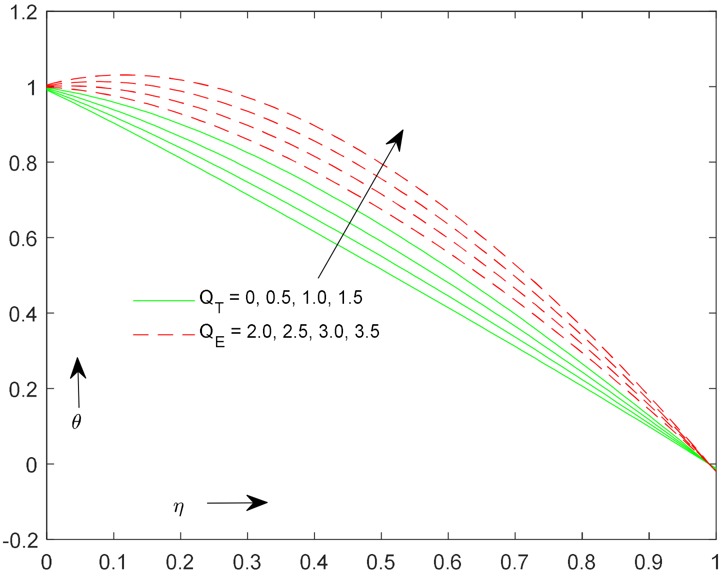

Figure 7. Temperature variation for Q_T and Q_E.

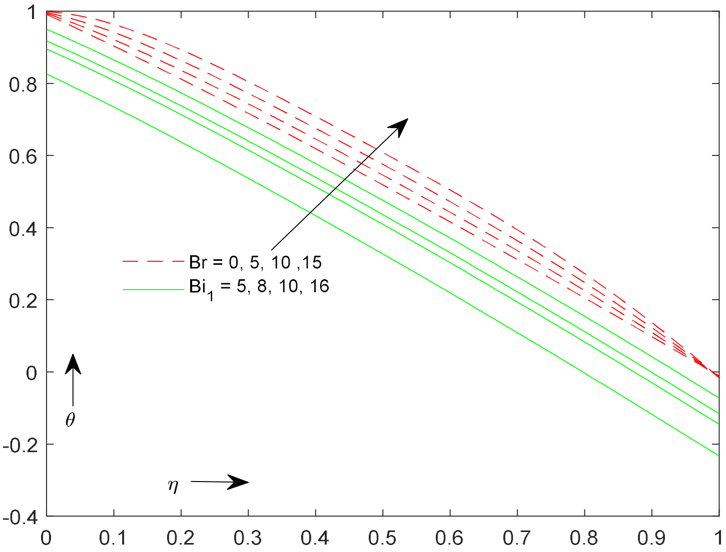

Figure 8. Temperature variation for Br and Bi_1.

Figure 9 indicates the variation in concentration distribution $\phi(\eta)$ corresponding to Sc and K_n. This figure depicts that concentration distribution, $\phi(\eta)$ is reducing with an augmentation in Sc and K_n values. The reason behind this is a reduction in mass diffusivity as the Schmidt number (Sc) value upsurges.

Figure 10 exhibits the variation in concentration distribution $\phi(\eta)$ for ascending values of n and Bi_2. It is quite obvious from these figures that $\phi(\eta)$ enhance for improving the values of n and Bi_2.

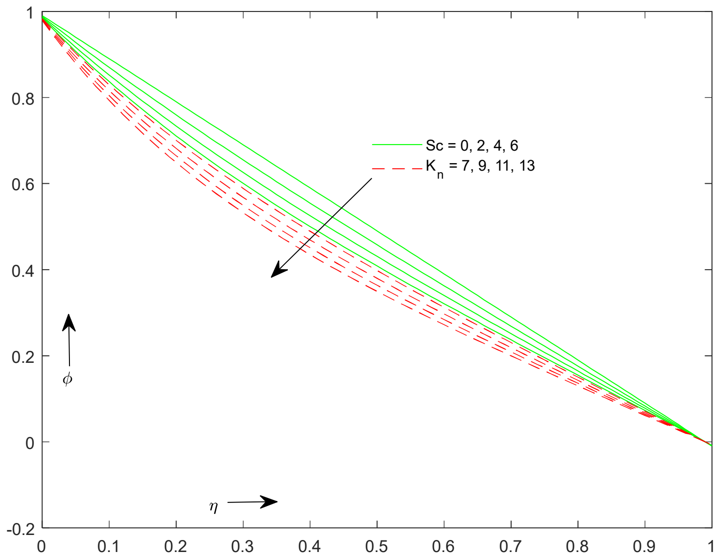

Figure 9. Concentration variation for Sc and K_n.

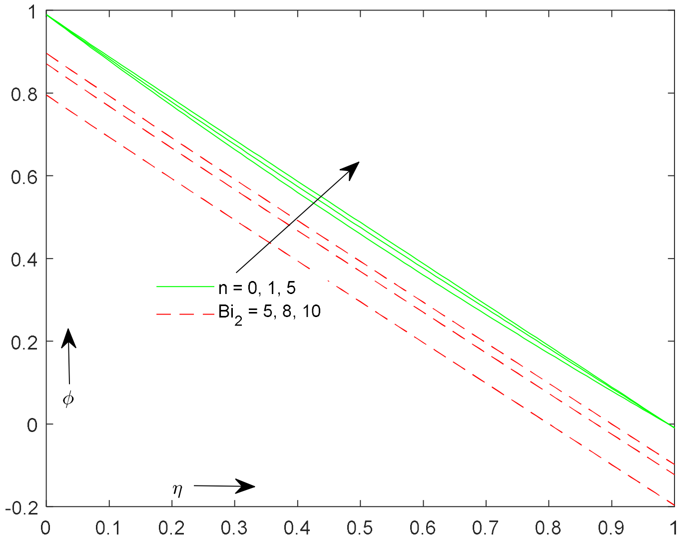

Figure 10. Concentration variation for n and Bi_2.

Figures 11–14 are sketched to depict the pertinent parameters impacting entropy production NS. These figures show more entropy production near the lower wall in comparison to that near the upper plate.

Figure 11 shows variation in NS due to the rising Brinkman number value. We observed, NS upsurges for ascending Br values. The reason behind, as Br is a parameter for viscous heating, and more heat is produced for larger values of Br which causes enhancement in NS and hence NS profile magnifies.

Figure 12 is drawn to exhibit the effect of Grashof numbers (Gr, and Gc) on NS. It depicts NS profile magnifies for ascending values of Grashof numbers, and the effect is significant in the entire channel width, and this is due to elevated friction (shear) near the walls.

Figure 13 is plotted to show the impact of Reynolds number (Re) and diffusion parameter (ϕ_C) on NS. It is noticed that an increase in Re values causes a reduction in NS and hence NS profile shrinks with ascending Reynolds number. This may be attributed to the decrease in velocity, which results in a decrease in heat transfer and hence, a decrease in entropy generation. It is seen in this graph that upsurging value of the parameter ϕ_C cause upsurge in NS value and hence the corresponding profile improves. This is attributed to the increased convection currents driven by the differences in the densities of the fluid under the influence of gravitational forces, leading to increased heat production.

In **Figure 14,** the impact of the temperature difference parameter (Ω_T) and concentration difference parameter (Ω_C) is shown on the entropy generation number. The figure shows that the rising Ω_T value lowers NS and the corresponding profile diminishes due to the assumption that the temperature difference between the wall of the channel and fluid layers is sufficiently small. It depicts that irreversibility levels heightens with upsurge in Ω_C values. A greater mass is deposited on the surface of the plates as concentration increases, resulting in higher pressure being exerted on the walls of the plates, which causes higher rates of entropy generation.

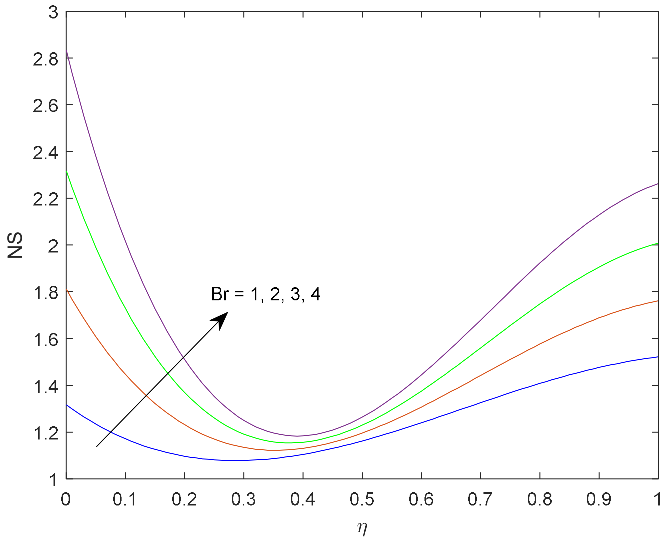

Figure 11. Entropy variation for Br.

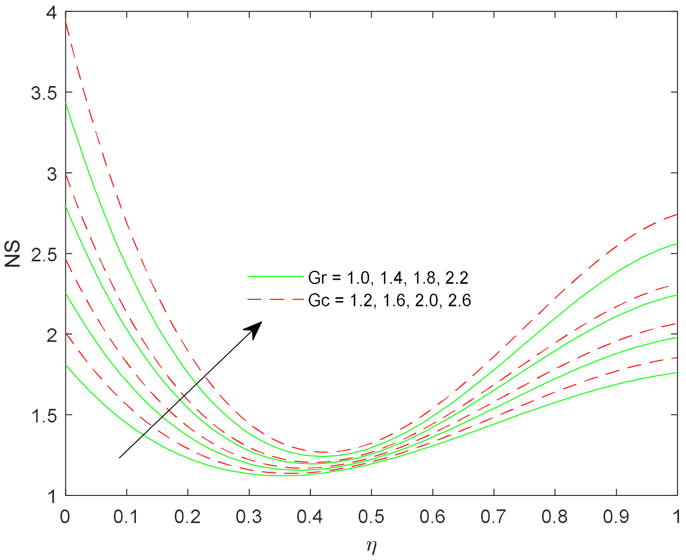

Figure 12. Entropy variation for Gr and Gc.

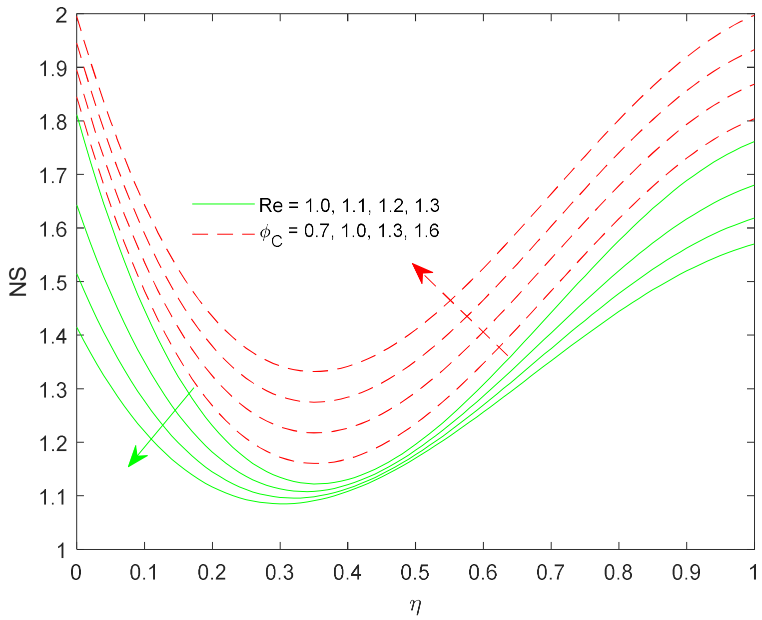

Figure 13. Entropy variation for Re and ϕ_C.

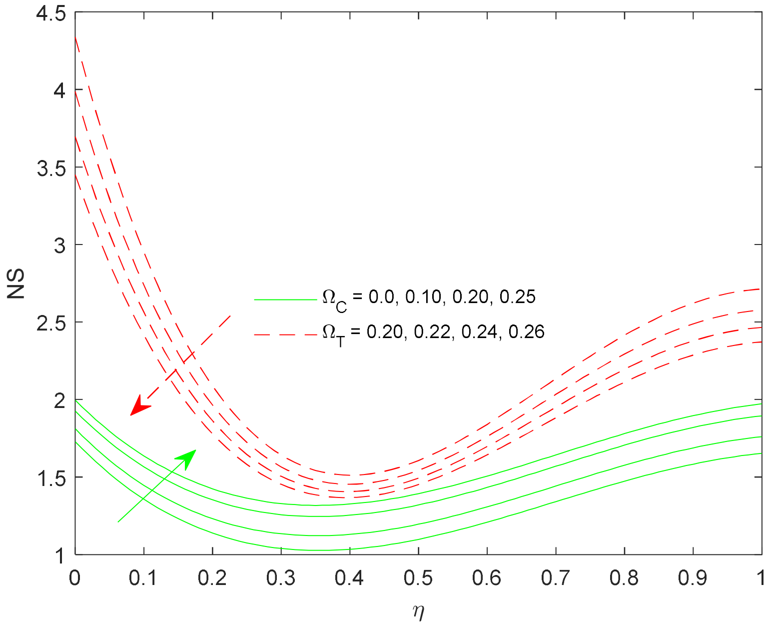

Figure 14. Entropy variation for Ω_T and Ω_C.

The values of the wall shear stress in terms of skin friction coefficient $\left(C_f\right)$ and rate of heat transport in terms of Nusselt number (Nu) for the rising values of the relevant parameters are shown in **Figures 15** and **16**. It is observed that the wall shear stress decreases by raising the values of Re, Ha, D, while, the parameters: Gr and Gc enhance it. The Nusselt number decreases with the growing value of the parameters Br, Q_T, Q_E, and Bi_1 however, scenario changes in case of ascending values of Ha, as can be seen from the figure. Furthermore, **Figure 17** illustrates the variation in the Sherwood number (Sh) for ascending values of pertinent parameters. It is concluded that enhancement in values of the parameters K_n, Sc, Bi_2 augments Sh while, effect of the parameter n is seen to reduce it.

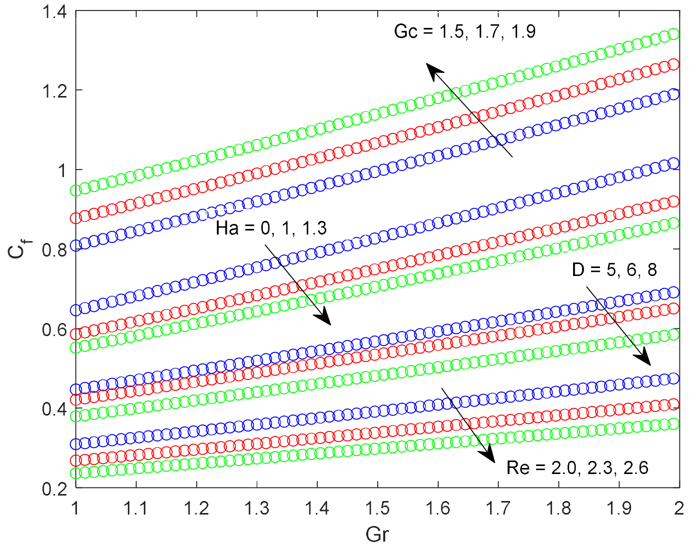

Figure 15. Skin friction coefficient for Gr, Gc, Ha, D, and Re.

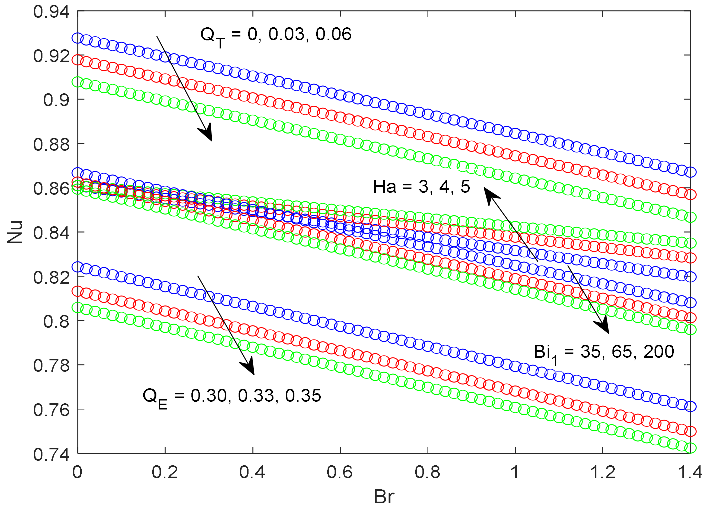

Figure 16. Nusselt number for Br, Q_T, Ha, Bi_1, and Q_E.

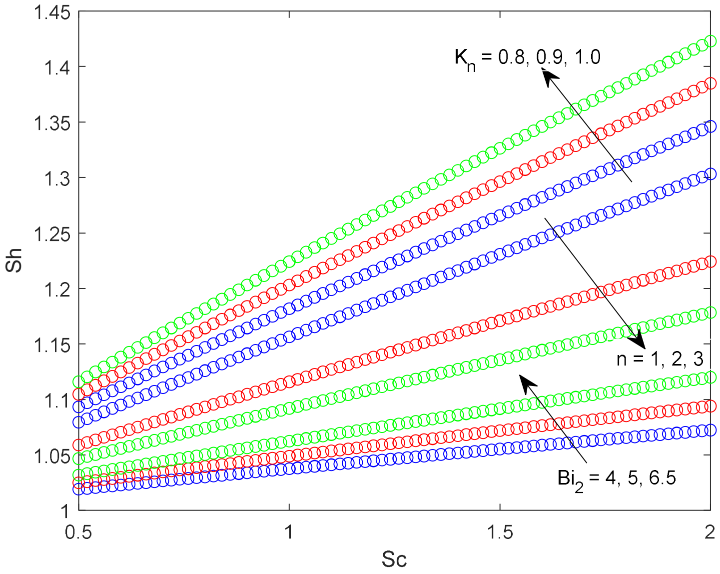

Figure 17. Sherwood number for Sc, K_n, n, and Bi_2.

8. Conclusions

In this research, we consider the fully developed steady-state laminar, natural convection flow of Williamson fluid in a vertical channel via porous medium. The velocity slip and the convective boundary conditions are applied. The contributions of higher order chemical reaction, viscous dissipation, Joule heating, and non-linear heat sources (ESHS/THS) are accounted for. Second-law analysis is presented in terms of entropy production. A numerical approach namely, Runge-Kutta 4th order is employed to tackle the problem with the shooting method. A comparison is also made using HPM (Homotopy Perturbation Method) in order to validate the findings. The conclusions of this study are:

1) Velocity field shrinks with rising values of D, Ha, Re, and We.
2) Velocity field upsurges with augmentation in values of Gr, Gc, Br, L, Q_T, and Q_E.
3) Temperature distribution magnifies with the rising values of Q_T, Q_E, Br, and Bi_1.
4) Concentration distribution increases for rising values of n and Bi_2, while it lessens for enhancement in values of Sc and K_n.
5) Entropy production upsurges as values of Br, Gr, Gc, Ω_T, and ϕ_C are increased, but it decreases as values of Re and Ω_T are increased.
6) Skin friction coefficient upsurges with enhancement in values of Gr and Gc while, the trend is changed in case of the parameters Re, Ha, D.
7) Nusselt number is observed to decrease with Br, Q_T, Q_E, and Bi_1 while, scenario changes in case of increasing values of Ha.
8) Rate of concentration transport upsurges with enhancement in values of K_n, Sc, and Bi_2 however, scenario changes in case of ascending values of n.

Author contributions: Conceptualization, AO and MK; methodology, MK; software, MK; validation, MK; formal analysis, AO and MK; investigation, MK; resources, MK; writing—original draft preparation, AO; writing—review and editing, AO and MK; visualization, MK; supervision, AO; project administration, AO. All authors have read and agreed to the published version of the manuscript.

Acknowledgments: The support provided by CSIR through the Senior Research Fellowship to Mukesh Kumar is gratefully acknowledged. The authors wish to express their thanks to the reviewers for their helpful comments and suggestions to improve the quality and presentation of this article.

Conflict of interest: The authors declare no conflict of interest.

References

1. Bruce RW, Na TY. Natural Convection Flow of Powell-Eyring Fluids between Two Vertical Flat Plates. ASME; 1967.
2. Aung W, Fletcher LS, Sernas V. Developing laminar free convection between vertical flat plates with asymmetric heating. International Journal of Heat and Mass Transfer. 1972, 15(11): 2293-2308. doi: 10.1016/0017-9310(72)90048-8
3. Vajravelu K, Sastri KS. Fully developed laminar free convection flow between two parallel vertical walls-I. International Journal of Heat and Mass Transfer. 1977, 20(6): 655-660. doi: 10.1016/0017-9310(77)90052-7
4. Rajagopal KR, Na TY. Natural convection flow of a non-Newtonian fluid between two vertical flat plates. Acta Mechanica. 1985, 54(3-4): 239-246. doi: 10.1007/bf01184849

5. Cheng CH, Kou HS, Huang WH. Flow reversal and heat transfer of fully developed mixed convection in vertical channels. Journal of Thermophysics and Heat Transfer. 1990, 4(3): 375-383. doi: 10.2514/3.190
6. Ziabakhsh Z, Domairry G. Analytic solution of natural convection flow of a non-Newtonian fluid between two vertical flat plates using homotopy analysis method. Communications in Nonlinear Science and Numerical Simulation. 2009, 14(5): 1868-1880. doi: 10.1016/j.cnsns.2008.09.022
7. Narahari M, Dutta BK. Free convection flow and heat transfer between two vertical parallel plates with variable temperature at one boundary. Acta Technica. 2011, 56: 103-113.
8. Kargar A, Akbarzade M. Analytic solution of natural convection flow of a non-newtonian fluid between two vertical flat plates using homotopy perturbation method (HPM). World Applied Sciences Journal. 2012, 20(11): 1459-1465. doi: 10.5829/idosi.wasj.2012.20.11.1707
9. Rashidi MM, Abelman S, Freidooni Mehr N. Entropy generation in steady MHD flow due to a rotating porous disk in a nanofluid. International Journal of Heat and Mass Transfer. 2013, 62: 515-525. doi: 10.1016/j.ijheatmasstransfer.2013.03.004
10. Hatami M, Hatami J, Jafaryar M, et al. Differential transformation method for Newtonian and Non-Newtonian fluids flow analysis: comparison with HPM and numerical solution. Journal of the Brazilian Society of Mechanical Sciences and Engineering. 2015, 38(2): 589-599. doi: 10.1007/s40430-014-0275-3
11. Raptis A, Massalas C, Tzivanidis G. Hydromagnetic free convection flow through a porous medium between two parallel plates. Physics Letters A. 1982, 90(6): 288-289. doi: 10.1016/0375-9601(82)90118-9
12. Chamkha AJ. Non-Darcy fully developed mixed convection in a porous medium channel with heat generation/absorption and hydromagnetic effects. Numerical Heat Transfer, Part A Applications. 1997, 32(6): 653-675. doi: 10.1080/10407789708913911
13. Singh KD, Pathak R. Effect of rotation and Hall current on mixed convection MHD flow through a porous medium filled in a vertical channel in presence of thermal radiation. Indian Journal of Pure & Applied Physics. 2012, 50: 77-85.
14. Das S, Jana RN, Makinde OD. An oscillatory MHD convective flow in a vertical channel filled with porous medium with Hall and thermal radiation effects. Special Topics & Reviews in Porous Media: An International Journal. 2014, 5(1): 63-82. doi: 10.1615/SpecialTopicsRevPorousMedia.v5.i1.60
15. Asha SK, Sunitha G. Effect of joule heating and MHD on peristaltic blood flow of Eyring–Powell nanofluid in a non-uniform channel. Journal of Taibah University for Science. 2019, 13(1): 155-168. doi: 10.1080/16583655.2018.1549530
16. Swain, BK, Parida BC, Kar S, et al. Viscous dissipation and joule heating effect on MHD flow and heat transfer past a stretching sheet embedded in a porous medium. Heliyon. 2020, 6(10): e05338. doi: 10.1016/j.heliyon.2020.e05338
17. Ramesh K, Riaz A, Dar ZA. Simultaneous effects of MHD and Joule heating on the fundamental flows of a Casson liquid with slip boundaries. Propulsion and Power Research. 2021, 10(2): 118-129. doi: 10.1016/j.jppr.2021.05.002
18. Ali A, Ahammad NA, Tag-Eldin E, et al. MHD williamson nanofluid flow in the rheology of thermal radiation, joule heating, and chemical reaction using the Levenberg–Marquardt neural network algorithm. Frontiers in Energy Research. 2022, 10. doi: 10.3389/fenrg.2022.965603
19. Williamson RV. The Flow of Pseudoplastic Materials. Industrial & Engineering Chemistry. 1929, 21(11): 1108-1111. doi: 10.1021/ie50239a035
20. Vasudev, R. Peristaltic Pumping of Williamson fluid through a porous medium in a horizontal channel with heat transfer. American Journal of Scientific and Industrial Research. 2010, 1(3): 656-666. doi: 10.5251/ajsir.2010.1.3.656.666
21. Subramanyam S, Reddy MVS, Reddy BJ. Influence of Magnetic Field on Fully Developed Free Convective Flow of a Williamson Fluid through a Porous Medium in a Vertical Channel. JAMFM. 2013, 5(1): 33-44.
22. Swaroopa B, Prasad KR. Influence of Radiation on MHD free Convective flow of a Williamson Fluid in a Vertical Channel. International Journal of Engineering and Technical Research. 2016, 5(2): 73-77.
23. Ajibade OA, Jha BK, Jibril HM, et al. Effects of dynamic viscosity and nonlinear thermal radiation on free convective flow through a vertical porous channel. International Journal of Thermofluids. 2021, 9: 100062. doi: 10.1016/j.ijft.2020.100062
24. Qawasmeh BR, Duwairi HM, Alrbai M. Non-Darcian forced convection heat transfer of Williamson fluid in porous media. Journal of Porous Media. 2021, 24(8): 23-35. doi: 10.1615/JPorMedia.2021025540
25. Pattanaik PC, Mishra SR, Jena S, et al. Impact of radiative and dissipative heat on the Williamson nanofluid flow within a parallel channel due to thermal buoyancy. Proceedings of the Institution of Mechanical Engineers. 2022, 236(1-2): 3-18. doi: 10.1177/23977914221080046

26. Usman, Shaheen S, Arain MB, et al. A case study of heat transmission in a Williamson fluid flow through a ciliated porous channel: A semi-numerical approach. Case Studies in Thermal Engineering. 2023, 41: 102523. doi: 10.1016/j.csite.2022.102523
27. Grosan T, Pop R, Pop I. Thermophoretic deposition of particles in fully developed mixed convection flow in a parallel-plate vertical channel. Heat and Mass Transfer. 2009, 45(4): 503-509. doi: 10.1007/s00231-008-0443-z
28. Ibrahim FS, Hady FM, Abdel-Gaied SM, et al. Influence of chemical reaction on heat and mass transfer of non-Newtonian fluid with yield stress by free convection from vertical surface in porous medium considering Soret effect. Applied Mathematics and Mechanics. 2010, 31: 675-684. doi: 10.1007/s10483-010-1302-9
29. Uwanta IJ, Hamza MM. Effect of suction/injection on unsteady hydromagnetic convective flow of reactive viscous fluid between vertical porous plates with thermal diffusion. International Scholarly Research Notices. 2014, 2014. doi: 10.1155/2014/980270
30. Prasannakumara BC, Gireesha BJ, Gorla R, et al. Effects of chemical reaction and nonlinear thermal radiation on Williamson nanofluid slip flow over a stretching sheet embedded in a porous medium. Journal of Aerospace Engineering. 2015, 29(5): 04016019. doi: 10.1061/(ASCE)AS.1943-5525.0000578
31. Singh K, Kumar M. Influence of chemical reaction on heat and mass transfer flow of a micropolar fluid over a permeable channel with radiation and heat generation. Journal of Thermodynamics. 2016, 2016: 8307980. doi: 10.1155/2016/8307980
32. Mallikarjun P, Murthy RV, Mahabaleshwar US, et al. Finite-Element Analysis of Fully Developed Mixed Convection through a Vertical Channel in the Presence of Heat Generation/Absorption with a First-Order Chemical Reaction. Defect and Diffusion Forum. 2018, 388: 394-406. doi: 10.4028/www.scientific.net/DDF.388.394
33. Loganathan P, Dhivya M. Heat and mass transfer analysis of a convective Williamson fluid flow over a cylinder. International Journal of Fluid Mechanics Research. 2020, 47(2): 171-189. doi: 10.1615/InterJFluidMechRes.2020027371
34. Huang JS. Chemical reaction and activation energy on heat and mass transfer for convective flow along an inclined surface in Darcy porous medium with Soret and Dufour effects. Journal of Mechanics. 2023, 39: 88-104. doi: 10.1093/jom/ufad006
35. Nazir S, Kashif M, Zeeshan A, et al. A study of heat and mass transfer of non-Newtonian fluid with surface chemical reaction. Journal of the Indian Chemical Society. 2022, 99(5): 100434. doi: 10.1016/j.jics.2022.100434
36. Olkha A, Kumar M. Casson fluid flow in a vertical annulus through porous medium with heat transfer characteristics and chemical reaction: An exact solution. IJMPC. 2022, 34(6): 2350078. doi: 10.1142/S012918312350078X
37. Olkha A, Kumar M. Heat transfer characteristics in non-Newtonian fluid flow due to a naturally permeable curved surface and chemical reaction. Heat Transfer. 2023, 52: 5431–5453. doi: 10.1002/htj.22934
38. Srinivas S, Malathy T, Reddy AS. A note on thermal-diffusion and chemical reaction effects on MHD pulsating flow in a porous channel with slip and convective boundary conditions. JKSUES. 2016, 28(2): 213-221. doi: 10.1016/j.jksues.2014.03.011
39. Oyelakin IS, Mondal S, Sibanda P. Unsteady Casson nanofluid flow over a stretching sheet with thermal radiation, convective and slip boundary conditions. Alexandria Engineering Journal. 2016, 55(2): 1025-1035. doi: 10.1016/j.aej.2016.03.003
40. Sharada K, Shankar B. Effect of partial slip and convective boundary condition on MHD mixed convection flow of Williamson fluid over an exponentially stretching sheet in the presence of joule heating. Global Journal of Pure and Applied Mathematics. 2017, 13(9): 5965-5975.
41. Zeeshan A, Shehzad N, Ellahi R. Analysis of activation energy in Couette-Poiseuille flow of nanofluid in the presence of chemical reaction and convective boundary conditions. Results in Physics. 2018, 8: 502-512. doi: 10.1016/j.rinp.2017.12.024
42. Neeraja A, Devi RR, Devika B, et al. Effects of viscous dissipation and convective boundary conditions on magnetohydrodynamics flow of casson liquid over a deformable porous channel. RINENG. 2019, 4: 100040. doi: 10.1016/j.rineng.2019.100040.
43. Jagadeesh S, Reddy MCK. Convection of 3D MHD non-Newtonian couple stress nanofluid flow via stretching surface. Heat Transfer. 2022, 52(2): 1081-1096. doi: 10.1002/htj.22730
44. Zia QZ, Ullah I, Waqas MA, et al. Cross diffusion and exponential space dependent heat source impacts in radiated three-dimensional (3D) flow of Casson fluid by heated surface. Results in Physics. 2018, 8: 1275-1282. doi: 10.1016/j.rinp.2018.01.001
45. Thriveni K, Mahanthesh B, Giulio L et al. Significance of induced magnetic field and exponential space dependent heat source on quadratic convective flow of Casson fluid in a micro-channel via HPM. Mathematical Modelling of Engineering

Problems. 2019, 6(3): 369-384. doi: 10.18280/mmep.060308

46. Mahanthesh B, Lorenzini G, Oudina FM, et al. Significance of exponential space-and thermal-dependent heat source effects on nanofluid flow due to radially elongated disk with Coriolis and Lorentz forces. Journal of Thermal Analysis and Calorimetry. 2020, 141: 37-44. doi: 10.1007/s10973-019-08985-0
47. Nagaraja B, Gireesha BJ. Exponential space-dependent heat generation impact on MHD convective flow of Casson fluid over a curved stretching sheet with chemical reaction. Journal of Thermal Analysis and Calorimetry. 2021, 143(6): 4071-4079. doi: 10.1007/s10973-020-09360-0
48. Swain K, Animasaun IL, Ibrahim SM. Influence of exponential space-based heat source and Joule heating on nanofluid flow over an elongating/shrinking sheet with an inclined magnetic field. International Journal of Ambient Energy. 2021, 43(1): 1-13. doi: 10.1080/01430750.2021.1873854
49. Hasibi A, Gholami A, Asadi Z et al. Importance of Induced Magnetic Field and Exponential Heat Source on Convective Flow of Casson Fluid in a Micro-channel via AGM. Theoretical and Applied Mechanics Letters. 2022, 12(3): 100342. doi: 10.1016/j.taml.2022.100342
50. Sharma BK, Kumar A, Gandhi R, et al. Exponential space and thermal-dependent heat source effects on electro-magneto-hydrodynamic Jeffery fluid flow over a vertical stretching surface. International Journal of Modern Physics B. 2022, 36(30): 2250220. doi: 10.1142/S0217979222502204
51. Yessef M, Bossoufi B, Taoussi M, et al. Improving the maximum power extraction from wind turbines using a second-generation CRONE controller. Energies. 2022, 15(10): 3644. doi: 10.3390/en15103644
52. Chojaa H, Derouich A, Zamzoum O, et al. Robust control of DFIG-based WECS integrating an energy storage system with intelligent MPPT under a real wind profile. IEEE Access. 2023, 11: 90065-90083. doi: 10.1109/ACCESS.2023.3306722
53. Loulijat A, Chojaa H, El marghichi M, et al. Enhancement of LVRT Ability of DFIG Wind Turbine by an Improved Protection Scheme with a Modified Advanced Nonlinear Control Loop. Processes. 2023, 11(5): 1417. doi: 10.3390/pr11051417
54. Hamid C, Aziz D, Zamzoum O, et al. Robust Control System for DFIG-Based WECS and Energy Storage in reel Wind Conditions. EAI Endorsed Transactions on Energy Web. 2024, 11. doi: 10.4108/ew.4856
55. Bejan A. A study of entropy generation in fundamental convective heat transfer. ASME Journal of Heat and Mass Transfer. 1979, 101(4): 718-725. doi: 10.1115/1.3451063
56. Bejan A. Short Communication Notes on the History of the Method of Entropy Generation Minimization (Finite Time Thermodynamics). Journal of Non-Equilibrium Thermodynamics. 1996, 21(3): 239-242. doi: 10.1515/jnet.1996.21.3.239
57. Baytas AC. Entropy generation for natural convection in an inclined porous cavity. International Journal of Heat and Mass Transfer. 2000, 43(12): 2089-2099. doi: 10.1016/S0017-9310(99)00291-4
58. Makinde OD, Eegunjobi AC. Entropy generation in a couple stress fluid flow through a vertical channel filled with saturated porous media. Entropy. 2013, 15(11): 4589-4606. doi: 10.3390/e15114589
59. Das S, Banu AS, Jana RN, et al. Entropy analysis on MHD pseudo-plastic nanofluid flow through a vertical porous channel with convective heating. Alexandria Engineering Journal. 2015, 54(3): 325-337. doi: 10.1016/j.aej.2015.05.003
60. Maskaniyan M, Nazari M, Rashidi S, et al. Natural convection and entropy generation analysis inside a channel with a porous plate mounted as a cooling system. TSEP. 2018, 6: 186-193. doi: 10.1016/j.tsep.2018.04.003
61. Yusuf TA, Mabood F, Prasannakumara BC et al. Magneto-bioconvection flow of Williamson nanofluid over an inclined plate with gyrotactic microorganisms and entropy generation. Fluids. 2021, 6(3): 109. doi: 10.3390/fluids6030109
62. Olkha A, Dadheech A. Second Law Analysis for Radiative Magnetohydrodynamics Slip Flow for Two Different Non-Newtonian Fluid with Heat Source. Journal of Nanofluids. 2021, 10(3): 447-461. doi: 10.3390/fluids6030109
63. Reddy PBA, Salah T, Jakeer S, et al. Entropy generation due to magneto-natural convection in a square enclosure with heated corners saturated porous medium using Cu/water nanofluid. Chinese Journal of Physics. 2022, 77: 1863-1884. doi: 10.1016/j.cjph.2022.01.012
64. Raje A, Bhise AA, Kulkarni A. Entropy analysis of the MHD Jeffrey fluid flow in an inclined porous pipe with convective boundaries. International Journal of Thermofluids. 2023, 17: 100275. doi: 10.1016/j.ijft.2022.100275
65. Balamurugan KS, Varma NU, Prasad JLR. Entropy generation analysis on forced and free convection flow in a vertical porous channel with aligned magnetic field and Navier slip. Heat Transfer. 2023. doi: 10.1002/htj.22897
66. He JH. Homotopy perturbation technique. Computer Methods in Applied Mechanics and Engineering. 1999, 178(3-4): 257-262. doi: 10.1016/S0045-7825(99)00018-3

67. He JH. Homotopy perturbation method: a new nonlinear analytical technique. Applied Mathematics and Computation. 2003, 135(1): 73-79. doi: 10.1016/S0096-3003(01)00312-5
68. He JH. An elementary introduction to recently developed asymptotic methods and nanomechanics in textile engineering. International Journal of Modern Physics B. 2008, 22(21): 3487-3578. doi: 10.1142/s0217979208048668
69. Singh AK and Paul T. Transient natural convection between two vertical walls heated/cooled asymmetrically. International Journal of Applied Mechanics and Engineering. 2006, 11(1): 143-154.

Energy Storage and Conversion 2024, 2(3), 538.
https://doi.org/10.59400/esc.v2i3.538

Review

Wind power forecasting technologies: A review

Krishan Kumar[1,*], **Priti Prabhakar**[1], **Avenesh Verma**[2]

[1] Department of Electrical and Electronics Engineering GJUS&T, Hisar 125001, Haryana, India
[2] Department of Instrumentation Engineering, Kurukshetra University, Kurukshetra 136119, Haryana, India
*** Corresponding author:** Krishan Kumar, morningkrishan@gmail.com

CITATION

Kumar K, Prabhakar P, Verma A. Wind power forecasting technologies: A review. Energy Storage and Conversion. 2024; 2(3): 538. https://doi.org/10.59400/esc.v2i3.538

ARTICLE INFO

Received: 30 May 2024
Accepted: 9 August 2024
Available online: 22 August 2024

Abstract: This study addresses the critical role of wind power forecasting in ensuring stable and reliable power system operations. Wind power forecasting is critical for the efficient operation of plants, time scheduling, and the balancing of power generation with grid integration systems. Due to its dependency on dynamic climatic conditions and associated factors, accurate wind power forecasting is challenging. The research delves into various aspects, including input data, input selection techniques, data pre-processing, and forecasting methods, with the aim of motivating researchers to design highly efficient online/offline models on weather-based data. The overarching goal is to enhance the reliability and stability of power systems while optimizing energy resource utilization. The analysis reveals that hybrid models offer more accurate results, highlighting their significance in the current era. This study investigates different Wind Power Forecasting (WPF) models from existing literature, focusing on input variables, time horizons, climatic conditions, pre-processing techniques, and sample sizes that affect model accuracy. It covers statistical models like ARMA and ARIMA, along with AI techniques including Deep Learning (DL), Machine Learning (ML), and neural networks, to estimate wind power.

Keywords: forecasting; neural networks; pre-processing; time series; wind power forecasting

1. Introduction

Rising demands for energy with a limited supply of fossil fuels have motivated the world to depend on renewable sources of energy, which include solar power, ocean power, geothermal power, biomass power, wind power, etc. These renewable energies act as an alternative solution to meet the huge demand of the world population [1]. Amongst which is wind power energy, which is highly rated as an as an encouraging and favorable power energy resource with abundant availability on the earth surface. In this current scenario, as demand for fossil fuels increases at a faster rate, there is a requirement to shift towards renewable energies. This leads to the use of the use of technology to find innovative solutions related to renewable energies. Hence Wind power forecasting has become one of the emerging research fields related primarily to electrical engineering. Several academicians and researchers are focused on the development of algorithms and related tools for forecasting wind power [2,3]. Ambitious goals are set by many nations to increase the generation of renewable energy to integrate into grid power, where a major contribution is expected from wind energy in order to reach these goals. But at the deeper levels, we can view uncertainty significantly and variability inherently in the generation of wind power, posing challenges in integrating wind power with grid power [4]. Generating wind energy is highly uncertain because it depends on the velocity of the wind, which is highly uncertain in nature. Also, wind farms are developing rapidly, creating the need for better forecasting methods of wind power generation. If these forecasting methods are accurate in computing the amount of wind power generated in the future, the cost incurred in balancing the system will be less. In the case of large windmill farms where wind power generation is on a large scale, substantial savings can be implied for the owners of the wind farm, increasing the overall efficiency of the system to a considerable level [2,5]. These power systems have a fundamental problem as the operators are unable to predict the schedule of generation of wind power due to its variability. Such inherent characteristics lead to commercial and technical implications for wind power systems and their effective planning and operation. Wind energy prediction power provides data on expected wind energy generation at specific time slots over a certain time interval. Hence, the critical aspect of the operation and integration of wind power totally depends on wind power forecasting [4]. **Figure 1** shows the way wind power forecasting takes place.

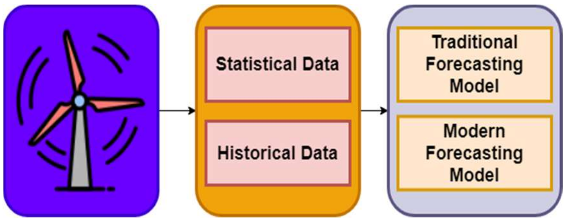

Figure 1. Wind power forecasting.

The necessity of forecasting for proper operation in power generation is part of planning for the future. However, the need for wind forecasting for wind power generation is given below:

- Wind power generation is variable in nature.
- The matching of supply and demand for power.
- The wind forecast system provides grid operators with a means to forecast and align electricity production and consumption.
- Operation planning decisions for the determination of the size, type, and economical location of wind power plants are to be planned in the future.
- Being able to predict wind output will make the electric grid work better under variable conditions.
- It is necessary for successful contract negotiations between suppliers and customers.
- Building of bidding strategies by the power suppliers and derivation of plans by the consumers in order to maximize the usage of utilities by purchasing electricity from pools [4].

Various approaches to forecasting wind power broadly fall into three main categories. The first categorization is based on a physical approach to meteorology, where various physical factors at the building of the model must be considered, which include humidity, roughness of the surface, temperature of the location, terrain quality, height of the hub, etc. The second approach is the statistical approach, which aims to find the relationship between the variables of the input of the wind power generation system and the output variables based on the data sets available in history. In this correlation, cross-correlation and auto-correlation functions are involved in wind power forecasting. In large-scale forecasting and long-term prediction, advantages are achieved by physical methods, whereas, in the short term, statistical methods are found to be good. Forecasting accuracy can be improved over time. To span the horizon, researchers focus on a hybrid method that combines both physical methods and statistical methods. Numerical prediction of weather, such as wind speed prediction, can be done by employing statistical methods/hybrid methods based on the input variables. Several approaches in the literature approve hybrid methods for forecasting in a better way. A training data set has to be selected that has great influence in establishing a model of statistical forecasting. In the approach of wind power forecasting, input variables that are non-linearly related to the output wind power can be easily constructed if the samples of training are the same as those of predicting the day [4–6].

In the wind forecasting models, they are categorized based on different technologies according to their accuracy. A comparative analysis of wind forecasting approaches is as follows in **Table 1**.

Table 1. Comparative analysis of wind forecasting approaches.

Wind forecast approach	Advantages	Features	Disadvantages
Physical approach	Focuses on how the wind flow flows around along with wind farm, their manufacturer's power curve and estimation over the wind power output range. Several sub-models are assigned together to translate the NWP forecast with the grid points	SCADA Data NWP Transformation to Hub Spatial refinement (Roughness)	Time-consuming Expensive Rebuilding is difficult
Statistical approach	Emulating the relation between each meteorological prediction where it attains the historical measurements and other generation output using the statistical models. Each parameter has their own estimated data without any phenomenon of physical medium into account.	NWP SCADA Data Statistical Model Kalman Filters ARMA	Misinterpretation in data Improper validation in data
Hybrid approach	In some of the WPF systems, they generally combine the two approaches along with other approaches to improve the forecast range.	Combination SCADA Data NWP	Diminished Type Divides between two categories Time-Series Losses Expensive
New casting model	Alternative way of forecasting based on the purpose. Tradeoff between the NWP costs and utility over the forecast.	Statistical Model	Only small scale in range Timescale for few hours
Regional forecasting	In some on-line information, the SCADA systems are measured mandatorily for the large farms. Up scaling approaches developed to forecast multiple farms	NWP Forecast Online SCADA Up scaling	Expensive Operation Time Limit

The objective of this review paper is to provide a comprehensive overview and critical analysis of the current state-of-the-art of WPF methodologies, techniques, challenges, and advancements. The contribution of the review aims to fulfill several objectives, including:

(1) Provide a comprehensive summary of existing literature and research findings in Wind Power Forecasting (WPF), covering historical developments, key concepts, and fundamental principles.

(2) Evaluate and categorize different methodological approaches used in WPF, including statistical methods, machine learning (ML), deep learning, and physical modeling techniques.

(3) Examine data sources for WPF, such as time series, meteorological data, turbine characteristics, and ancillary data, and explore data pre-processing techniques for cleaning, normalization, and feature engineering.

2. Background

In the literature technical survey, several techniques were applied to forecast wind power, i.e., hard (ARIMA-Autoregressive Integrated Moving Average, ARIMA-Wavelet & Mixed modeling approaches) and soft computing techniques (ANN). An appropriate model is adopted using algorithms that take physical phenomena into account to control the process. Therefore, in this section, we discuss the objectives and outcomes of wind power predictive models in existing literature, as shown in **Table 2**.

Table 2. Objective and outcomes of wind power predictive models.

Ref.	Objective	Outcome
[1]	Different ANN models are used to improve the WPF accuracy for short & very short-term time span basis. For the selection of inputs of the reference wind power station of the concerned wind farm meteorological information is considered.	New ANN models were proposed by varying the number of prior hours at input layer of ANN model. Achieve better accuracy in terms of mean absolute relative error (MARE) up to 7.5%. Further for long time span forecasting more degree of improvement is required.
[2]	The random fluctuations in the wind a natural process will cause challenges to the electrical system designers. It is necessary to forecast wind power with higher accuracy on short term basis.	In this, least square fitting & batch normalization (BN) techniques has been used to pre-process the input data.
[3]	The integration of wind farms output generation with electricity grid is a tough challenge for the continuous and proper functioning of electricity supply system. So, a precise and highly accurate wind power prediction system is required for the efficient operation of wind farm with electricity grid integrated system.	The proper forecasting performance was compared with the other neural networks (NN) based models such as: back propagation & Gaussian regression.
[7]	For improving the prediction accuracy, a hybrid model using variational mode decomposition (VMD), long & short memory network (LSTM) is used. In this, data has been pre-processed through VMD algorithm and forecasting has been carried out using LSTM.	The proposed model achieved forecasting accuracy in terms of mean absolute error of 1534.5 KW and RMSE of 2345.89 KW on 1hours a-head basis.
[8]	In this WT is used for input data pre- processing, PSO is used for optimal tuning of neural network model for WPF.	The proposed model outperformed and have accuracy of 6.378 in terms of NAPE which is far better from other NN based model
[9]	To forecast the wind power SVM and gray based model have been implemented for suitable and efficient forecast with higher accuracy. The gray model can work efficiently using small data at input level.	As compare to other bench mark and statistical models the accuracy is better.
[10]	The proposed paper was on literature in which different input selection and neural network models with pre-processing have been analyzed.	The hybrid model is most accurate and efficient one but they take more time to forecast.
[11]	In the particular, seasonal proper weather predictions of wind data have proven useful for the wind power generation for industry.	Electricity production depends on the many factors in addition to the wind conditions; the capacity factor is a suitable indicator to quantify the effects of wind fluctuations on production.
[12]	On the basis of Euclidean distance and angle cosine algorithms a novel clustering methodology has been proposed for short term WPF. The forecasting has been performed using neural network model.	The results in terms of accuracy proved the superiority of proposed model as compare to others.
[13]	The Markov chain model is implemented to forecast accurately the time series data of wind collected from wind farm on short term time span basis.	In an Indian geographical location of Jodhpur city in Rajasthan has been taken into consideration and achieve better forecast error.

3. Wind power forecasting techniques

During the wind energy power forecasting process, data such as wind pace (speed), historical data, wind direction in the farm with respect to speed of the wind, and data on historical production of power in the wind farm are utilized. Wind power system output is composed of output values of generated power at different horizons of forecasting. But there is variation in the prior hours before the hour of forecasting, along with the forecasting horizon length. In the literature, various methods of wind forecasting have been discussed, which are classified broadly based on the structure of the model, their operation, and the data sets. In a few other models that are subsequently explained, further reference station wind farm data, historical data on wind speed, and data on direction of wind are utilized. In this section, we categorize power forecasting and wind speed based on the input data variables, time-scaling, generated output power, and the method of forecasting.

3.1. Input data

According to input data, we can classify deterministic wind speed forecasting into two subclasses: the NWP model, i.e., numerical weather prediction models working on a time series basis, and the purely time-based series model. NWP models are developed by meteorologists for predicting weather based on the simulation of the Earth's atmosphere. This model of NWP is an approximate numerical solution depending on the equations of the atmospheric processes and the changes occurring in them [14–17]. The related primary equations utilized in this model are energy conservation, water conservation, mass conservation, momentum conservation, and the state equation. The NWP model divides the Earth's atmosphere into three-dimensional cubes with horizontal model resolution and vertical model resolution, respectively. Orography is represented by the horizontal resolution, whereas the phenomenon of weather is represented by the vertical resolution [18]. The resolution size is influenced profoundly by the model. For example, only limited details will be available in coarse resolution from the heights and valleys of the mountain. Better resolution is obtained by higher resolution, but it involves more computation. Both at the regional and global levels, NWP models are applicable. Less time and low computational resources are required by time series data compared to NWP data for modeling and operation. Traditionally, forecasting in the long term utilizes the approach of Measure Correlate Predict (MCP) [19]. This approach to MCP considers the measured value of wind speed at the wind farm, which is then correlated with the meteorological station data taken for the long term utilizing the technique of linear regression. But there are so many problems related to time series data, meteorological data planning, the measurement of precise data from meteorological stations, and the availability of calibrated weather stations. In many countries, the number of meteorological weather stations is limited as the management of these stations is considerably high. Thus, for input selection, some of the statistical tools can be utilized, like correlation, auto-correlation, cross-correlation, and partial auto-correlation [20,21].

3.2. Time-scales

In forecasting, the time scale involved depends on the requirements of the end user, the conditions involved technically, and situations of regularity. In the literature, there is limited data on the forecasting time scales. However, considering the literature, we can categorize the time scale into four divisions from very short to long-term forecasting, i.e., VST, ST, MT, and LT forecasting. The time scale for VST forecasting ranges from a few seconds to 30 min. The generation of wind power can be forecasted at various time scales based on the application intended. Wind power forecasting for active turbine control typically ranges from milliseconds to minutes, which is generally referred to as Very Short-Term (VST) forecasting. Trading of energy or management of power systems requires forecasting ranging from 48 to 72 h, such that decisions on conventional power plants are taken to provide commitment for a particular power unit and for optimizing power dispatch from these plants. These kinds of forecasting are termed short-term forecasting [19,22].

Maintenance of conventional power plants with wind farms can be planned by forecasting 5 to 7 days ahead, which is termed long-term forecasting. Offshore wind farm maintenance is expensive; hence, importance is given to maintenance under optimal planning. The prediction of wind power based on temporal resolution can range from 10 min to a few hours, depending on the length of the forecast. Wind power (energy) forecasting can be improved by involving more input values and providing uncertain estimates with conventional predictions [22].

3.3. Power output

Forecasted output can be obtained in two ways. The first is the direct method, by which we can obtain the forecasted wind power through supervisory control and data acquisition; hence, this method is called the direct method. Another method involves wind speed forecasting, based on which a power curve is drawn for converting this forecasting into output wind power. This method is termed the indirect method.

3.4. Forecasting methods

These are the following forecasting techniques at present:

Persistence Method: Persistence Method also known as the Native Predictor, depends on the high correlation between current wind speed and future wind speed values. It is assumed that at ‘t’ time, the current wind speed is the same at ‘$t + \Delta t$’ time, such that the equation is $v\ (t + \Delta t) = v(t)$. This method is known for providing good accuracy even at very short levels of forecasting [23].

3.4.1. Physical method

This method indeed requires physical meteorological data such as temperature, roughness of the local surface, pressure, power curves of wind turbines, and obstacles involved in prediction. This physical method is categorized into two different categories, which include the D (diagnostic) model and the CFD model, i.e., the computational fluid dynamic model. The CFD model simulates fields of wind flow dynamically, whereas the diagnostic model utilizes boundary layer parameterization. These diagnostic models are ideally appropriate for wind flow in areas such as flat landscapes, but computational fluid dynamics models are suitable for areas where wind speed is considered over complex terrains. Commercially, wind power forecasting (WPF) utilizes the NWP model for providing input data for the forecasting, which is then refined accordingly to obtain the forecasted output wind speed for the onsite conditions. The interpolation of wind speed can be downscaled based on the physical methods that utilize a mesoscale or microscale model for obtaining the wind farm hub height. The resolution attained along with the domain size range differentiates whether it is a mesoscale (meso) model or a microscale (micro) model. The power is estimated using forecasted wind flow or speed. The easiest way is to apply and use the power curve from the manufacturer. The scaling errors can be corrected by the approach of Model Output Statistics (MOS). Understanding physical behavior is enabled by the physical models incorporated into orography. Complex numerical systems can be solved by these models using initial conditions generated using regional forecasting and global forecasting. In such models, historical data are less important. But for wind prediction to be done accurately, extensive information is required on the wind farm's characteristics and the roughness of the surface [23].

3.4.2. Statistical method

In statistical methods, recursive techniques are utilized to obtain relations based on the time series data. Precise prediction is obtained by these models in a cheaper and easier way for short-term forecasting. As there is an increase in time, there is a degradation in the accuracy obtained from the statistical model. Predefined mathematical models are not involved; hence, these models depend on the patterns.

3.4.3. Artificial intelligence/machine learning method

The inputs for the statistical model are historical data; hence, these models are independent of the model's internal state. A statistical time series method for wind energy forecasting may be developed based on various techniques like SVM, ANN models, regression models, etc.

Artificial neural network (ANN)

ANN, i.e., the artificial neutral network model, was proposed in 1934 by McCullloch and Pits. The workings of this network are identical to those of the human brain; hence, it is able to make decisions by biological neurons. In the human brain, a neuron is able to perform various processes in parallel and analyses various patterns. This similar technique can be utilized for solving non-linear mathematical problems such as image processing, wind forecasting, etc. In this ANN model, training is provided continuously for obtaining the best weight value to plot input to output. ANN involves three layers, namely the input, hidden, and output layers. This network is based on two different algorithms, i.e., the LM (Levenberg Marquardt) algorithm and the Pola-Ribiere algorithm, to predict the output value. Its basic idea is represented in **Figure 2**.

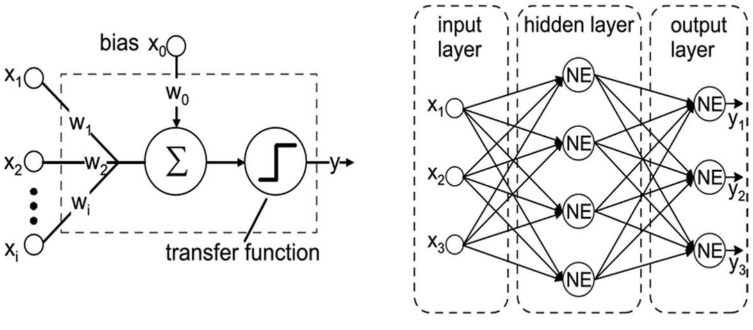

(a) (b)

Figure 2. ANN (Artificial Neural Network).

Regression model

In this model, dependent and independent variables are related to each other. This model involves fitting a straight line to the data. Assumption is made that the mean wind speed, being the dependent variable, has a normal distribution. The direction of wind, pressure, temperature, and precipitation are considered independent variables. The values of the dependent variables and independent variables are associated together. As the number of independent variables influences the dependent variables, in this case, multivariate regression is applicable instead of univariate regression [24].

Support vector machine

This technique was introduced in 1995 by Vapnik and Cortes using statistical learning. Initially, this approach was developed for the process of pattern recognition, but now this technique is utilized in several processes such as diagnosis of faults, retrieval of images, computation of regression, forecasting, etc. This model is trained based on time series, which is similar to a neural network model, and overfitting curves or local minima are not required in this technique. The basic SVM architecture is shown in **Figure 3**.

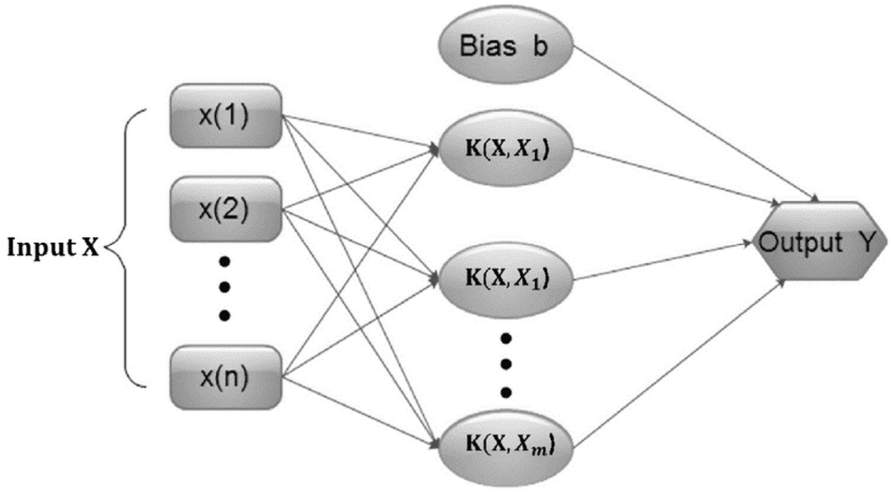

Figure 3. SVM (Support Vector Machine).

Where Y: Output function, b: bias [25].

Forecasting models based on physical method

This method interacts between geographical and meteorological data sets. The relationship between the dynamic motion of the wind due to the solar radiation in the atmosphere and the physical state is obtained by utilizing statistical equations and functions [26].

Numerical weather prediction

This study represents the current measurement of weather practiced to forecast the future weather state. The perfect solution is to utilize the NWP model, where the forecast horizon ranges from one day to several days. Hence, this technique is valuable for forecasting in several applications, e.g., PV (solar) forecasting, wind forecasting, etc. This model is also able to predict the cloud transient variation, which is the greatest obstacle to the solar irradiance of the ground. The future conditions are predicted using the NWP model after assimilation of the existing findings.

Empirical model

The first empirical model was proposed by Hargreaves and Samani in 1982 and is used to represent the activities for creating models both through experiments and observation. The evolution of several other models is based on variations in factors such as sunshine hours, content of water vapor, minimum and maximum temperature, temperature, pressure, wind direction, guest speed of the wind, humidity, etc. Wind power is the key parameter measured for most of the empirical models. Future values of wind power forecasting can be determined by an empirical model, which is the technique that establishes the relationship between linear and non-linear wind power and meteorological variables.

Forecasting technique based on the ensemble method

The method commonly used for solar irradiation forecasting is the ensemble method, which predicts with greater precision than the isolated method. In an individual model, several factors are considered in order to model it accurately. Integrating two or more methods for the forecasting process is termed a hybrid approach. A hybrid model combines two or more linear or non-linear models for forecasting. Based on the literature, hybrid models involve several techniques, such as preprocessing, postprocessing, and optimization.

Deep learning

Deep prediction can be done in an accurate way using a deep neural network. It provides a good result as it involves a number of hidden units, and the learning of this model is based on continuous training. The passing of information occurs from one layer to the next. Initially, weights are assigned; finally, the result is obtained by summing the weights obtained.

4. Factor affecting wind power forecasting

There are so many other factor/parameter that ensure model forecasting accuracy, either directly/indirectly. These factors affect wind power generation. Wind power forecasting (WPF) depends on forecast horizons, geographical conditions, climatic variability, testing period, normalization, and pre-processing technique.

4.1. Forecast horizon

The time horizon issue is related to the future period for which the model is forecasting. This period may be from 1 minute to several hours or days. According to a review of the literature, forecast horizons can be broadly classified into four different categories [27]:

Very-short-term forecasting (1 min to several minutes ahead). This category includes forecasts ranging from 1 min to several minutes ahead, typically used for immediate decision-making and operational planning.

Short-term forecasting (1 h to several hours/days ahead). Encompassing forecasts from 1 h to several hours or days ahead, this category is vital for short-range planning, energy scheduling, and grid management.

Mid-term forecasting (1 month to 12 months ahead). Covering forecasts from 1 month to 12 months ahead, this horizon is crucial for medium-range planning, resource allocation, and market analysis.

Long-term forecasting (12 months to several years ahead). Extending from 12 months to several years ahead, this category is essential for strategic planning, policy formulation, and investment decisions in the energy sector.

4.2. Climatic variability

The variables in the input data may be systemic, endogenous, and exogenous. On various combinations of input parameters, different models behave differently. In most studies, ANN gives importance to meteorological and geographical variables. The increased number of irrelevant meteorological parameters/data’s degrades the performance and accuracy of the model. Therefore, the appropriate and suitable parameters have to be selected to increase the performance and accuracy of a model.

4.3. Preprocessing techniques

The model’s accuracy can be increased using the pre-processing technique for input data sets. The input data sets for a particular targeted site obtained from every entity are extremely unpredictable and abnormal. The preprocessing techniques used on the data were used to increase or scale down the data element. Many researchers have used wavelet transform (WT) to pre-process the input time series into different constituents, while EMD further dissects the input series into various constituent parts. This combined use of WT and EMD algorithms allows for a more comprehensive decomposition of the input series, aiding in the improvement of model accuracy [28].

4.4. Training and testing period

The training and testing cycle is also an important factor that affects the accuracy of the model. Various studies have shown that the large collection of training data sets enhances learning capacity and also improves accuracy [26].

4.5. Geographical location

The model behavior changes according to the geographical location, and different wind locations affect its performance [4–6,29–35].

5. Outcomes of the literature survey

The typical wind forecasting has forced the researchers to treat the problem as a forecasting issue in various domains, which include the planning stage, executing the operational stage, and balancing a power system in real time. Hence, in order to take care of the efficient forecasting issues that are related to wind power forecasting techniques, these are some outcomes after a deep study:

Much research is also focused on seasonal wind energy generation, which is affected by numerous factors despite wind-flowing conditions. In order to quantify wind speed variability, the impact capacity factor is an important indicator to take care of.

The pre-processing of data, which involves classification, plays an important role in accurate forecasting.

Identification of the forecasting issues with different time series and scales using a different hybrid model for accurate and efficient forecasting.

As ANN is one of the most viable means, conventional algorithms have the ability to get proper and efficient forecasting of wind power.

Various developed hybrid models can be effectively compared with some other forecasting models for predicting their performance and evaluation in predicting the efficient forecasting of the power system.

Much research has also proposed an ANN model that emerged by using assorted 1-hour time intervals elected for the input value using layer parameters and an output layer with hidden layers of neural networks along with wind farm reference stations.

6. Conclusion

Wind power forecasting plays an important and crucial role in reliable, stable, and efficient power system operations. Currently, a number of studies are going into the field of wind power forecasting to develop methodologies in order to achieve better forecasting accuracy levels. Each model/technique developed has its own characteristics as per the available input data used, along with its parameters characterized on the basis of forecasting horizons. In this, a review has been done on wind power forecasting at an intermediate stage, and it also requires more reliable data clustering/pre-processing tools to obtain more accurate results. From the review analysis, it has been analyzed that hybrid models, which involve data pre-processing and learning tools, present more accurate results and are the need of the present era. Hence, using the outcomes of this research, it will be very easy for power system researchers to design new models for forecasting wind power.

Acknowledgments: The work was carried out within the literature survey and existing forecasting technologies.

Conflict of interest: The authors declare no conflict of interest.

References

1. Velazquez Medina S, Portero Ajenjo U. Performance Improvement of Artificial Neural Network Model in Short-term Forecasting of Wind Farm Power Output. Journal of Modern Power Systems and Clean Energy. 2020; 8(3): 484-490. doi: 10.35833/mpce.2018.000792
2. Li Y, Yang F, Zha W, et al. Combined Optimization Prediction Model of Regional Wind Power Based on Convolution Neural Network and Similar Days. Machines. 2020; 8(4): 80. doi: 10.3390/machines8040080
3. Li LL, Zhao X, Tseng ML, et al. Short-term wind power forecasting based on support vector machine with improved dragonfly algorithm. Journal of Cleaner Production. 2020; 242: 118447. doi: 10.1016/j.jclepro.2019.118447
4. Saroha S, Aggarwal SK. A Review and Evaluation of Current Wind Power Prediction Technologies. Wseas Transactions on Power Systems. 2015; 10.
5. Hippert HS, Pedreira CE, Souza RC. Neural networks for short-term load forecasting: a review and evaluation. IEEE Transactions on Power Systems. 2001; 16(1): 44-55. doi: 10.1109/59.910780
6. Aggarwal SK, Saini LM, Kumar A. Electricity price forecasting in deregulated markets: A review and evaluation. International Journal of Electrical Power & Energy Systems. 2009; 31(1): 13-22. doi: 10.1016/j.ijepes.2008.09.003
7. Sun Z, Zhao M. Short-Term Wind Power Forecasting Based on VMD Decomposition, ConvLSTM Networks and Error

Analysis. IEEE Access. 2020; 8: 134422-134434. doi: 10.1109/access.2020.3011060

8. Mandal N, Sarode T. Prediction of Wind Speed using Machine Learning. International Journal of Computer Applications. 2020; 176(32): 34-37. doi: 10.5120/ijca2020920370
9. Zhang Y, Sun H, Guo Y. Wind Power Prediction Based on PSO-SVR and Grey Combination Model. IEEE Access. 2019; 7: 136254-136267. doi: 10.1109/access.2019.2942012
10. Yousuf Mu, Al-Bahadly I, Avci E. Current Perspective on the Accuracy of Deterministic Wind Speed and Power Forecasting. IEEE Access. 2019; 7: 159547-159564. doi: 10.1109/access.2019.2951153
11. Lledó L, Torralba V, Soret A, et al. Seasonal forecasts of wind power generation. Renewable Energy. 2019; 143: 91-100. doi: 10.1016/j.renene.2019.04.135
12. Sun G, Jiang C, Cheng P, et al. Short-term wind power forecasts by a synthetical similar time series data mining method. Renewable Energy. 2018; 115: 575-584. doi: 10.1016/j.renene.2017.08.071
13. Verma SM, Reddy V, Verma K, et al. Markov Models Based Short Term Forecasting of Wind Speed for Estimating Day-Ahead Wind Power. In: Proceedings of the 2018 International Conference on Power, Energy, Control and Transmission Systems (ICPECTS); 22-23 February 2018; Chennai, India. pp. 31-35. doi: 10.1109/icpects.2018.8521645
14. Jiang Y, Chen X, Yu K, et al. Short-term wind power forecasting using hybrid method based on enhanced boosting algorithm. Journal of Modern Power Systems and Clean Energy. 2015; 5(1): 126-133. doi: 10.1007/s40565-015-0171-6
15. Draper NR, Smith H. Applied Regression Analysis. John Wiley & Sons; 1998. doi: 10.1002/9781118625590
16. Felder M, Sehnke F, Ohnmeiß K, et al. Probabilistic short term wind power forecasts using deep neural networks with discrete target classes. Advances in Geosciences. 2018; 45: 13-17. doi: 10.5194/adgeo-45-13-2018
17. Qian Z, Pei Y, Zareipour H, et al. A review and discussion of decomposition-based hybrid models for wind energy forecasting applications. Applied Energy. 2019; 235: 939-953. doi: 10.1016/j.apenergy.2018.10.080
18. Ghadimi N, Akbarimajd A, Shayeghi H, et al. Two stage forecast engine with feature selection technique and improved meta-heuristic algorithm for electricity load forecasting. Energy. 2018; 161: 130-142. doi: 10.1016/j.energy.2018.07.088
19. Morshedizadeh M, Kordestani M, Carriveau R, et al. Application of imputation techniques and Adaptive Neuro-Fuzzy Inference System to predict wind turbine power production. Energy. 2017; 138: 394-404. doi: 10.1016/j.energy.2017.07.034
20. Du P, Wang J, Yang W, et al. A novel hybrid model for short-term wind power forecasting. Applied Soft Computing. 2019; 80: 93-106. doi: 10.1016/j.asoc.2019.03.035
21. Chen S, Ye L, Zhang G, et al. Short-term wind power prediction based on combined grey-Markov model. In: Proceedings of the 2011 International Conference on Advanced Power System Automation and Protection; 16-20 October 2011; Beijing, China. pp. 1705-1711. doi: 10.1109/apap.2011.6180647
22. Hu Q, Zhang R, Zhou Y. Transfer learning for short-term wind speed prediction with deep neural networks. Renewable Energy. 2016; 85: 83-95. doi: 10.1016/j.renene.2015.06.034
23. Chang WY. A Literature Review of Wind Forecasting Methods. Journal of Power and Energy Engineering. 2014; 2: 161–168.
24. Md Azmi CSA, Alkahtani AA, Hen CK, et al. Univariate and multivariate regression models for Short-Term Wind Energy Forecasting. Information Sciences Letters. 2022; 11(2): 465–473. doi: 10.18576/isl/110217
25. Vapnik, Cortes C. Support Vector Machine: A Statistical Learning Approach. Journal of Pattern Recognition. 1995; 15(3): 145-160. doi: 10.1234/jpr.1995.15.3.145-160
26. Rodríguez F, Fleetwood A, Galarza A, et al. Predicting solar energy generation through artificial neural networks using weather forecasts for microgrid control. Renewable Energy. 2018; 126: 855-864. doi: 10.1016/j.renene.2018.03.070.
27. Smith J, Johnson L. Time horizon considerations in forecasting models: A review of literature. Energy Forecasting Journal. 2023; 10(3): 45-58. doi: 10.1234/energyforecastingjournal.2023.10.3.45-58
28. Singla P, Duhan M, Saroha S. Different normalization techniques as data preprocessing for one step ahead forecasting of solar global horizontal irradiance. In: Dubey AK, Narang SK, Srivastav AL, et al. (editors). Artificial Intelligence for Renewable Energy Systems. Elsevier; 2022. pp. 209-230. doi: 10.1016/b978-0-323-90396-7.00004-3.
29. Singla P, Duhan M, Saroha S. A comprehensive review and analysis of solar forecasting techniques. Frontiers in Energy. 2021; 16(2): 187-223. doi: 10.1007/s11708-021-0722-7.
30. Sun S, Wang S, Zhang G, et al. A decomposition-clustering-ensemble learning approach for solar radiation forecasting. Solar Energy. 2018; 163: 189-199. doi: 10.1016/j.solener.2018.02.006.
31. Alhmoud L, Wang B. A review of the state-of-the-art in wind-energy reliability analysis. Renewable and Sustainable Energy

Reviews. 2018; 81: 1643-1651. doi: 10.1016/j.rser.2017.05.252.

32. Singh A, Gupta S. Training and testing period in wind forecasting: Impact on model accuracy. Renewable Energy Journal. 2023; 15(2): 102-115. doi: 10.1234/renewableenergyjournal.2023.15.2.102
33. Zendehboudi A, Baseer MA, Saidur R. Application of support vector machine models for forecasting solar and wind energy resources: A review. Journal of Cleaner Production. 2018; 199: 272-285. doi: 10.1016/j.jclepro.2018.07.164.
34. Heydari A, Astiaso Garcia D, Keynia F, et al. A novel composite neural network based method for wind and solar power forecasting in microgrids. Applied Energy. 2019; 251: 113353. doi: 10.1016/j.apenergy.2019.113353.
35. Florita A, Hodge BM, Orwig K. Identifying Wind and Solar Ramping Events. In: Proceedings of the 2013 IEEE Green Technologies Conference (GreenTech); 4-5 April 2013; Denver, CO, USA. pp. 147-152. doi: 10.1109/greentech.2013.30

Energy Storage and Conversion 2024, 2(3), 480.
https://doi.org/10.59400/esc.v2i3.480

Review

A mini review on electroosmotic phenomena in porous media

Yan Gao[*]**, Chunling Wang, Zhuo Gong, Zhiqiang Li**

College of Science, China Jiliang University, Hangzhou 310018, China
*** Corresponding author:** Yan Gao, P21080854007@cjlu.edu.cn

CITATION

Gao Y, Wang C, Gong Z, Li Z. A mini review on electroosmotic phenomena in porous media. Energy Storage and Conversion. 2024; 2(3): 480. https://doi.org/10.59400/esc.v2i3.480

ARTICLE INFO

Received: 15 March 2024
Accepted: 29 June 2024
Available online: 10 July 2024

Abstract: The electroosmosis phenomenon in porous media finds widespread applications in various fields such as microfluidic systems, polymer electrolyte membrane fuel cells, oil and gas engineering, wastewater sludge dewatering, groundwater dynamics, etc. Therefore, the electroosmotic flow mechanism in porous media has attracted broad interest from multiple disciplines. This paper provides an overview of the physical mechanisms and mathematical models for electroosmosis in porous media. The background of electric double layer theory and state-of-the-art research progress on pore-scale models for electroosmotic flow through porous media are reviewed. Two typical and significant research topics, electroosmosis under pressure coupling effects and nanoscale electroosmotic phenomena, are then focused on. The advances in theoretical analysis, numerical simulation, and experimental measurements are summarized. Finally, the potential research directions for electroosmotic flow in porous media are addressed.

Keywords: electroosmosis; porous media; electric double layer; pressure coupling effect; nanoscale

1. Introduction

The electrokinetic phenomenon refers to the relative motion between solid and liquid phases or the generation of electric potential in colloidal systems where solid and liquid coexist under the influence of an applied electric field. Electrokinetic phenomena are generally classified into four categories [1]: electrophoresis, electroosmosis, streaming potential, and sedimentation potential. However, these four kinds of electrokinetic phenomena may coexist and have strong relationships with each other (as shown in **Figure 1**).

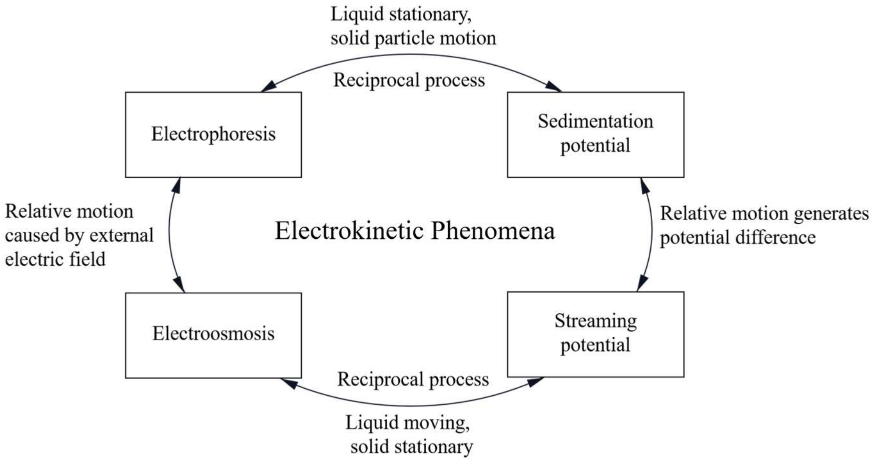

Figure 1. The relationship between electrokinetic phenomena.

In 1809, Russian scientist Ruess first observed the directed movement of clay particles under the influence of an electric field in experimental studies, which was termed electrophoresis [2]. And the solid clay particles may induce the movement of charged particles in the liquid phase, which is known as electroosmosis. Electroosmosis (also called electroosmotic flow, or EOF) can be considered the reverse process of electrophoresis. In 1852 and 1859, German physical chemists Wiedemann [3] and Quincke [4], respectively, found that when pressure is applied to a liquid passing through a porous ceramic plate, a potential difference is generated in the direction of flow. This phenomenon is called streaming potential. In 1878, German physicist Dorn [5] observed the settling of particles under the influence of gravity, resulting in a sedimentation potential. All of these phenomena mentioned above are collectively referred to as electrokinetic phenomena. Both the solid and liquid phases have charges on their surfaces, and the charges on the solid surface attract charges with equal magnitude but opposite polarity, forming an electric double layer (EDL) structure at the interface between the solid and liquid phases. The schematic diagram of electrokinetic phenomena is shown in **Figure 2**.

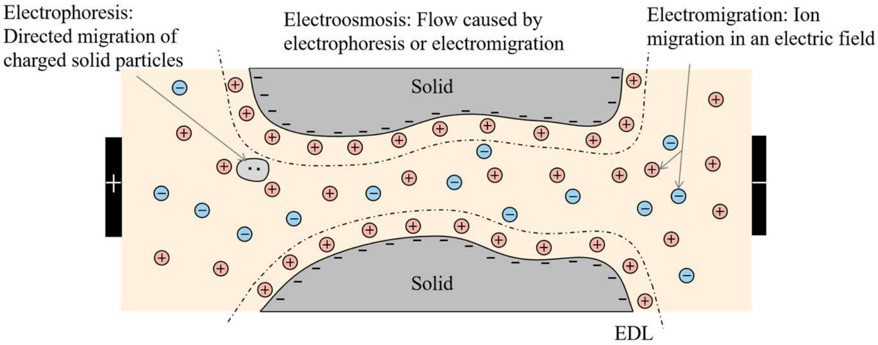

Figure 2. The schematic graph of electrokinetic phenomena.

Electrokinetic phenomena have been widely applied in various fields such as oil and gas engineering [6], energy and environmental technology [7], biomedical science [8], chemical industry [9], etc. In practical industrial applications, when an electric field acts on a charged fluid, the charged particles in the fluid are subjected to the force of the electric field, resulting in fluid flow. Studying this flow phenomenon is crucial for improving industrial production efficiency and reducing production costs, making in-depth research on the electroosmotic flow phenomenon of great significance. Electroosmotic flow is a key aspect of electrokinetic phenomena, describing the flow behavior of charged fluids at the microscale under the influence of an electric field. The application of electroosmotic flow covers a wide range of fields. For example, in the petroleum industry [10], the flow rate of oil can be increased by applying an external electric field, which enhances the oil recovery rate accordingly. In the field of microfluidic devices [11], lab-on-a-chip technology enables the miniaturization of sample preparation, reactions, separations, and detection techniques by using electrokinetic phenomena. In terms of cooling technology [12], the application of electrokinetic phenomena in microchannel cooling has potential for improving cooling performance. In sludge dewatering and treatment [13], the surface water can be effectively removed by electroosmosis. In the biomedical field, a minimally invasive technique using a microneedle array combined with reverse iontophoresis has been employed to non-invasively extract interstitial fluid from the cellular interstitium below 25 millimeters from the skin surface. This technology enables more convenient medical devices for blood glucose monitoring [14] and drug delivery [15]. In the field of human-computer interaction, the development of tactile interaction devices utilizing electroosmotic pump arrays, such as tactile gloves [16], provides more immersive and realistic interactive experiences in virtual reality, augmented reality, and gaming. In the field of energy, electroosmotic flow is used for ion transport and mass separation in batteries, fuel cells, and supercapacitors [17].

Despite the significant progress made in electroosmosis research over the past few decades, there are still some drawbacks and limitations. The eletroosmosis phenomenon involves the coupling of multiple physical processes, such as the electric field, fluid mechanics, and electrolyte mass transfer. Current research often focuses on studying these processes separately, neglecting the interactions and coupling effects between them. And with the development of micro- and nanotechnology, the mechanisms of electroosmosis in nano-scale porous media are significant and attract broad interest. As a result, a comprehensive understanding of the electroosmotic flow behavior in complex and multiscale systems still requires further investigation. Therefore, this paper provides an overview of electrokinetic phenomena and an up-to-date review of eletroosmosis through porous media. The background and fundamentals of EDL are first introduced. And the pore-scale mathematical models of eletroosmosis through porous media are summarized and reviewed. Then, electroosmosis under pressure coupling effects and nanoscale electroosmotic mechanisms are explored. The research progress on theoretical analysis, numerical simulation, and experimental measurement in these two fields is presented. Finally, the possible and valuable research topics in electroosmosis through porous media are pointed out.

2. EOF in porous media

2.1. EDL theory

The EDL structure at the solid-liquid interface primarily discusses the distribution patterns of ions and the corresponding variations of potential with distance. Since the late 19th century, several physical models have been proposed to understand EDL and its mechanisms. In 1879, Helmholtz [18] first proposed a parallel plate model for EDL.

$$\sigma = \frac{\varepsilon_0 \varepsilon_r \psi_0}{\delta} \tag{1}$$

where σ represents the surface charge density of the solid, ε_r is the relative permittivity of the medium between the plates, ε_0 is the permittivity of vacuum, ψ_0 is the surface potential, and δ is the distance between the parallel plates. Between 1910 and 1913, Gouy [19] and Chapman [20] proposed a diffuse EDL model by introducing a diffuse layer into the Helmholtz model. That is, there are two electric layers at the charged interface in an electrolyte solution: the inner and outer layers (**Figure 3a**). This model is capable of characterizing the potential variation with distance from the plate. In 1924, Stern combined the Helmholtz model and the Gouy-Chapman model to propose the Stern EDL model [21]. It consists of two parts: the stern layer and the diffuse layer. The layer adjacent to the surface is named the compact layer or Stern layer; the diffuse layer is between the Stern layer and the interior of the liquid phase. As shown in **Figure 3b**, the potentials of the solid phase and the Stern layer are ψ_0 and ψ_s, respectively. And δ and ξ denote the Stern layer thickness and potential at the diffuse layer boundary, respectively.

In order to study the EOF through porous media, the capillary model is generally employed to characterize the electroosmosis path. As shown in **Figure 4**, the potential at the capillary wall is denoted as ψ_0, the potential at a distance of r is denoted as $\psi(r)$, and the excess charge density is denoted as $\rho(r)$. By employing the Stern EDL model and considering a monovalent electrolyte, the Poisson equation becomes:

$$\frac{1}{r}\frac{d}{dr}\left[r\frac{d\psi(r)}{dr}\right] = -\frac{\rho(r)}{\varepsilon_r\varepsilon_0} \tag{2}$$

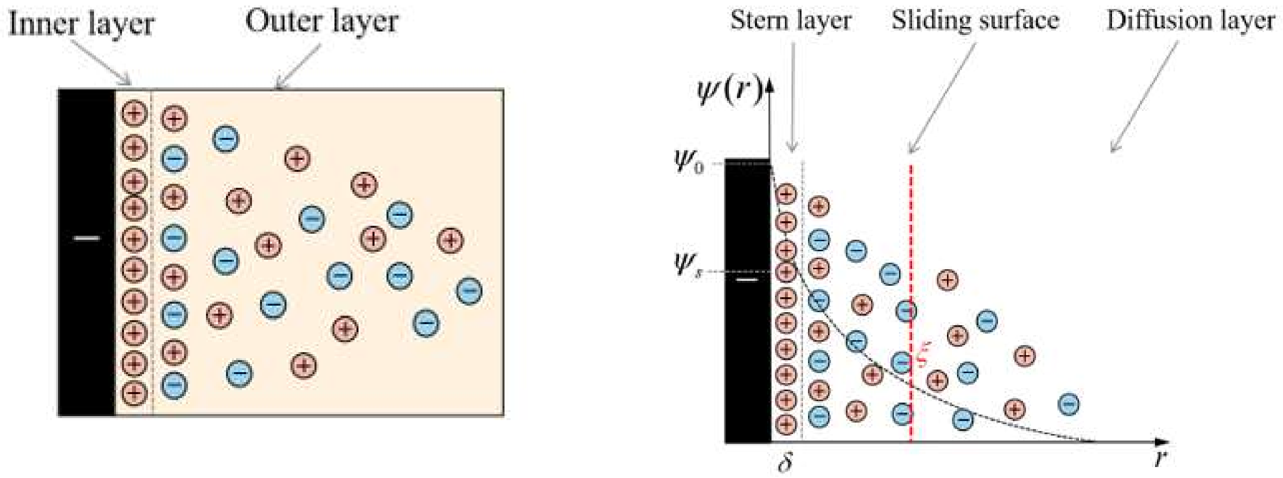

(a) Gouy-Chapman diffusion double layer model. **(b)** Stern double layer model.

Figure 3. Diffusion electric double-layer model.

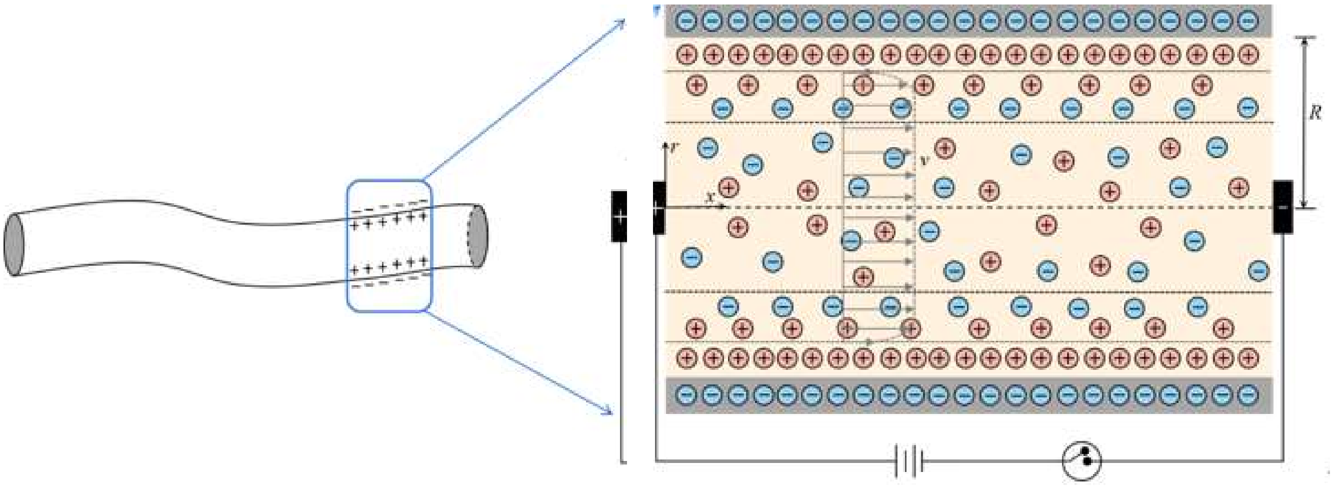

(a) Single capillary tube. **(b)** Electric double layer phenomenon in capillaries.

Figure 4. Schematic diagram of capillary double layer.

Based on Boltzmann equation, the charge density can be gotten as:

$$\rho(r) = -2ne\, sinh \frac{e\psi(r)}{kT} \tag{3}$$

where k is the Boltzmann's constant, T is temperature, n is the Avogadro number and e is the elementary charge. By using Debye–Hückel approximation, $\frac{e\psi(r)}{(kT)} \ll 1$ and $\frac{sinh\, e\psi(r)}{(kT)} \simeq \frac{e\psi(r)}{(kT)}$. It should be noted that this approximation would only be applicable to very small values of potential.

The Poisson-Boltzmann distribution equation then becomes

$$\frac{1}{r}\frac{d}{dr}\left[r\frac{d\psi(r)}{dr}\right] = \kappa^2\psi(r) \tag{4}$$

where $\kappa = \sqrt{\frac{2ne^2}{\varepsilon_0\varepsilon_r kT}}$ is the reciprocal of the EDL thickness. For a cylindrical capillary, the boundary conditions are as follows:

$$\psi(r) = \begin{cases} \left.\frac{d\psi(r)}{dr}\right|_{r=0} = 0 \\ \psi(R) = \psi_0 \end{cases} \tag{5}$$

Then, the analytical solutions for $\psi(r)$ and $\rho(r)$ are:

$$\psi(r) = \psi_0\frac{I_0(\kappa r)}{I_0(\kappa R)} \tag{6}$$

$$\rho(r) = -\varepsilon_0\varepsilon_r\kappa^2\psi_0\frac{I_0(\kappa r)}{I_0(\kappa R)} \tag{7}$$

where I_0 is the modified Bessel function of the first kind of zero order. The velocity profile $v(r)$ through a tortuous capillary under an electric field U can be expressed by:

$$v(r) = \frac{\varepsilon_0\varepsilon_r\psi_0 E}{\mu}\left[1 - \frac{I_0(\kappa r)}{I_0(\kappa R)}\right] \tag{8}$$

where μ is fluid viscosity, L_0 is the representative length of the porous media, $E=U/L_0$ is applied electric field gradient.

2.2. Progress on EOF

Porous media are composed of minerals (such as silicates, oxides, and carbonates) or other materials (such as polymers and biomaterials), and these porous materials typically carry charges due to isomorphic substitutions in their structure. In order to explore the EOF mechanism in porous media, theoretical analysis, numerical simulations, and experimental studies have been conducted on EOF in ideal and simplified devices, including capillaries, parallel plates, and microchannels. And the influences of device shape and size on EOF were investigated in detail.

In 1965, Rice and Whitehead [22] conducted a systematic theoretical analysis on electrokinetic phenomena in narrow cylindrical capillaries using the Debye-Hückel approximation, which is only applicable in small surface potential. Later, Levine et al. [23] and Olivares et al. [24] extended the theory proposed by Rice and Whitehead by dividing the capillary into low surface potential regions and high surface potential regions and solving for the surface potential in each region. In 1990, Ohshima and Kondo [25] derived simple approximate analytical formulas for electroosmotic velocity, volume flow rate, current, and streaming potential in the study of the electrokinetic effect between two parallel plates. In 1997, Mala et al. [26] explored the influence of the electrokinetic effect on the liquid flow characteristics in microchannels between two parallel plates. In 2013, Luong and Sprik [27] conducted U-tube experiments in saturated porous media to measure the relationship between the electrokinetic effect and electric field strength, aiming to assess the permeability and pore structure of the material. In 2020, Luo and Keh [28] analyzed the electrokinetic flow and accompanying electrical conduction of salt-free solutions in charged circular capillaries along the axial direction. They solved for the electrostatic potential distribution and fluid velocity distribution within the capillary channel. In 2022, Ning et al. [29] utilized a fractal capillary bundle model to develop the electro-hydrodynamic coupling process in non-steady pressure-driven flows. They derived analytical expressions for the potential distribution and velocity distribution within the channels.

Capillary models with different geometries have been proposed to study EOF in porous media. For example, Paillat et al. [30] studied the EOF in porous media based on a single capillary; Wu and Papadopoulos [31] used cylindrical and annular capillary bundle models to study the EOF in porous media; and Pascal et al. [32] examined the impact of rectangular, cylindrical, and annular ideal capillaries on the EOF flow rate in porous fibrous media. Since the pore structures of porous media indicate random and irregular characteristics, fractal geometry has been proposed to develop a pore-scale model for EOF in porous media. In 2013, Bandopadhyay et al. [33] used fractal theory to study EOF characteristics in porous media with irregular or non-uniform terrain features, investigated the influence of the conductivity tensor on domain morphology and solid fraction, and compared it with the equivalent Darcy permeability. In 2015, Liang et al. [34] analyzed the electroosmotic characteristics in fractal porous media and investigated the factors that influence the height difference. In 2020, Thanh et al. [35] obtained theoretical expressions for the electroosmotic pressure coefficient and permeability of porous media based on a tortuous fractal cylindrical capillary bundle model. In 2023, Xu et al. [36] established a new pore-scale physical model for EOF in sludge porous media and derived the analytical expressions for EOF flow rate and permeability.

The external electric field or pressure has been proposed on the microchannel walls to modulate the electroosmotic effect and thereby control the fluid velocity and flow distribution. In 2011, Vennela et al. [37] studied the Sherwood number due to the combined flow driven by pressure and electroosmotic flow in porous microtubes. In 2013, Dutta [38] theoretically investigated the electroosmotic flow characteristics of nanofluidic separation of non-neutral analytes by combining the forward pressure gradient with the counteracting force electroosmotic flow field. In 2019, Kou and Dejam [39] studied the dispersion phenomena caused by pressure and electroosmotic flow in channels surrounded by permeable porous media. In 2019, Rosenfeld and Bercovici [40] employed an electroosmotic pump to control capillary flow, where the applied voltage could regulate the capillary driving speed. They investigated the filling, mixing, and transport of liquids in a microfluidic paper-based analytical device. In 2020, Godinez-Brizuela and Niasar [41] mainly investigated the flow generated by the simultaneous action of pressure and electroosmotic flow in charged porous media and studied the pore-scale effects in mixing and dispersion processes. In 2024, Terutsuki et al. [42] utilized the electroosmotic flow generated by the combination of anion and cation hydrogels to achieve electroosmotic flow-controlled delivery, thereby realizing chemical transport. In 2024, Mondal and Chaube [43] investigated the peristaltic flow of unstable, viscous, and incompressible fluids in capillary channels under two-dimensional conditions. They simplified the model and derived analytical expressions for the electroosmotic characteristics, considering the thin EDL situation.

3. EOF with pressure effect

Both pressure-driven and electroosmosis-driven flow are important methods for fluid propulsion. Compared with common pressure-driven flow, electroosmosis-driven flow offers advantages such as low cost, high efficiency, a long lifespan, ease of operation and control, etc. The pressure-driven flow generally forms a parabolic velocity profile (**Figure 5a**), while the electroosmosis-driven flow exhibits a plug-like flow profile (**Figure 5b**). The uniform velocity distribution across the cross-section enables the precise separation of samples by electrophoresis.

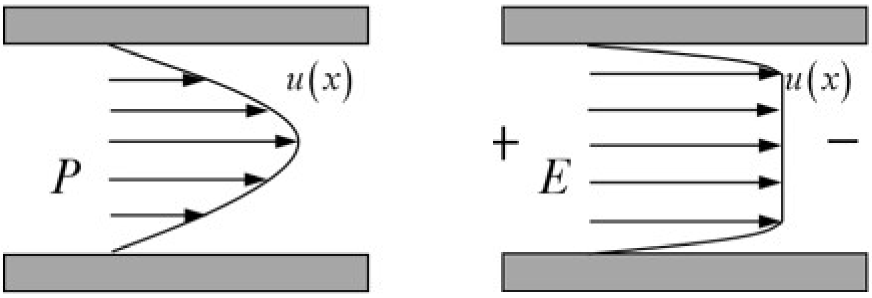

(a) Pressure-driven velocity profile.

(b) Electroosmosis-driven velocity profile.

Figure 5. Velocity profile of pressure-driven and Electroosmosis-driven flow.

When considering the pressure effect in electroosmotic flow, the choice of an appropriate model depends on the specific conditions and requirements of the system. Two commonly used models for incorporating the pressure effect in electroosmotic flow are the Helmholtz-Smoluchowski (HS) model and the Modified Helmholtz-Smoluchowski (MHS) model. The HS model is only suitable for low-pressure systems. While the effect of fluid compressibility is included in the MHS model.

The flow rate of EOF with pressure effect depends on the applied electric field, zeta potential of the channel walls, fluid properties (viscosity, conductivity), channel geometry, pressure gradient, and even the presence of additional external forces. Various empirical or semi-empirical equations have been proposed to describe the EOF flow with pressure, that is, simultaneous pressure and electroosmosis-driven flow. As illustrated in **Table 1**, there is a clear difference between these available models for flow rate. Rice and Whitehead [22] proposed a narrow, straight cylindrical capillary model based on the double-layer theory and Boltzmann equation. They derived the electroosmotic flow velocity and electroosmotic flow rate and discussed the relationship between electroosmotic phenomena and flow radius. Kobayashi et al. [44] designed a vertical electroosmotic experimental setup, considering factors such as gravity, pressure, and electric field forces. They got the potential distribution, electroosmotic flow velocity, and electroosmotic flow rate in capillary channels. Paillat et al. [30] used a cylindrical straight capillary model, the pore radius of which is much larger than the EDL thickness, to derive the electroosmotic flow velocity. Vennela et al. [37] used a two-dimensional cylindrical micro-pore model based on the EDL theory and the Boltzmann equation and explored the relationship between the Sherwood number and the Debye length. Dutta [38] carried out a numerical simulation on a two-parallel-plate channel model to investigate the charge separation in nanofluids. They derived a normalized electroosmotic flow velocity equation. Thanh et al. [35] utilized a curved cylindrical channel model based on fractal theory and obtained electroosmotic flow velocity and electroosmotic flow rate inside the channel.

The pressure-driven flow through a cylindrical and tortuous capillary with a radius of R can be characterized by the Hagen-Poiseuille equation. Thus, according to Equation (8) under the Debye-Hückel approximation, the flow velocity under the simultaneous effect of pressure and electric field can be written as:

$$v(r) = -\frac{1}{4\mu}(R^2 - r^2)\frac{\Delta P}{L_\tau} + \frac{\varepsilon_0 \varepsilon_r |\zeta| E}{\mu}\left[1 - \frac{I_0(\kappa r)}{I_0(\kappa R)}\right] \tag{9}$$

Therefore, the volumetric flow rate in the capillary is given by:

$$q(R) = \int_0^R v(r)\, 2\pi r dr = -\frac{\pi R^4}{8\mu}\frac{\Delta P}{L_\tau} + \frac{\pi \varepsilon_0 \varepsilon_r |\zeta| R^2 E}{\mu}\left[1 - \frac{2I_1(\kappa R)}{\kappa R I_0(\kappa R)}\right] \tag{10}$$

where I_1 is the first-order modified Bessel function of the first kind.

Figure 6 illustrates the variation of $C = 1 - \frac{2I_1(\kappa R)}{[\kappa R I_0(\kappa R)]}$ with the radius R. It can be observed that as the radius R of the capillary increases, the value of C approaches to 1. Therefore, the flow rate in a single capillary under simultaneous effect of pressure and electric field can be simplified as:

$$q(R) = -\frac{\pi R^4}{8\mu}\frac{\Delta P}{L_\tau} + \frac{\pi \varepsilon_0 \varepsilon_r |\zeta| R^2 E}{\mu} \tag{11}$$

Table 1. Flow rate of EOF with pressure effect.

Flow rate	**Geometric model**	**References**
$v(r) = \frac{P}{4\mu}(a^2 - r^2) - \frac{\varepsilon\zeta}{4\pi\mu}E\left[1 - \frac{I_0(\kappa r)}{I_0(\kappa a)}\right]$	narrow straight cylindrical capillary model	[20]
$v(r) = \frac{\varepsilon\zeta E_z}{\mu}\left(\frac{I_0(\kappa a)}{I_0\{\kappa(d/2 - \delta)\}} - 1\right) + \frac{(d/2 - \delta)^2 - a^2}{4\mu}\left(-\frac{dP}{dz}\right)$	vertical straight cylindrical capillary model	[39]
$v(r) = \frac{\Delta P}{4\mu L}(r^2 - a^2) - E\rho_p\delta_0^2\left[\frac{I_0(r/\delta) - I_0(a/\delta_0)}{I_0(a/\delta_0)}\right]$	cylindrical straight capillary model	[28]
$v(r) = \frac{a^2 P}{4\mu}\left[1 - \left(\frac{r}{a}\right)^2\right] - \frac{\varepsilon\zeta E_x}{\mu}\left[1 - \frac{I_0(\kappa r)}{I_0(\kappa a)}\right]$	two-dimensional cylindrical micro-pore model	[35]
$v^*(r) = \frac{3}{2}(1 + ff\left\{\frac{1 - cosh(\kappa y^*)/\, cosh(\kappa/2)}{1 - tanh(\kappa y^*)/(\kappa/2)}\right\}$	two-parallel-plate channel model	[36]
$v(r) = -\frac{1}{4\mu}(a^2 - r^2)\frac{\Delta P}{L_\tau} + \frac{\varepsilon_0\varepsilon_r\zeta}{\mu}\left[1 - \frac{I_0(\kappa r)}{I_0(\kappa a)}\right]\frac{\Delta V}{L}$	curved cylindrical channel model	[33]

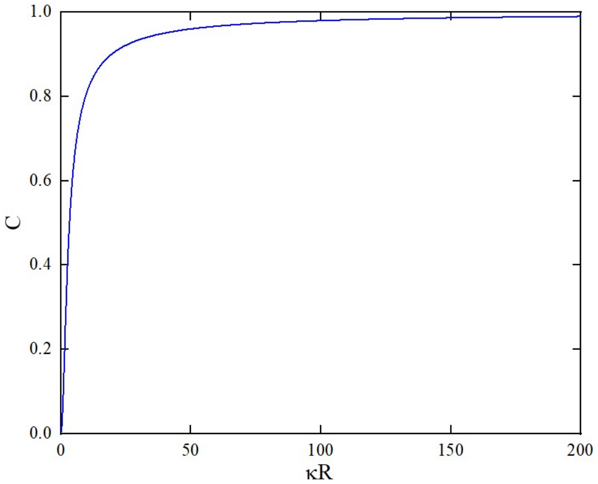

Figure 6. Variation of the dimensionless coefficient C with the dimensionless ratio of pore size to Debye length.

4. EOF in nano porous media

Most of the available research was performed on the EOF in porous media with a regular pore size, where the thickness of the EDL can be neglected. However, the electroosmotic phenomenon in porous media with micro- to nanoscale pores is greatly influenced by the EDL because the thickness of the EDL is comparable to the radius of the capillary, and the EDL poses a certain hindrance to fluid flow. The classical Poisson-Boltzmann equation cannot accurately describe the particle distribution inside micro-nano channels/pores, especially in the region close to the solid phase. This is mainly due to the fact that the interactions between ion-ion and solid wall atom-ion are neglected in the continuum theoretical models, which become significant at the nanoscale. Therefore, the EOF in nanoscale porous media brings new challenges and attracts broad interests.

In order to measure the velocity distribution, concentration distribution, and flow patterns inside micro- and nano-scale channels and pores, a few experimental techniques were proposed and applied (as shown in **Table 2**). So far, visualization experiments can be broadly categorized into trajectory line methods [45], bright field observation methods [46], micro-PIV particle velocimetry methods [47], LIF (laser-induced fluorescence) methods [48], and chromatography techniques [49]. The trajectory line method, also known as trajectory analysis, involves tracking the movement path and velocity of tracer particles to obtain the fluid's flow trajectories and velocity distribution. The bright field observation method utilizes high-speed cameras or microscopes to directly observe the flow behavior inside channels or pores, capturing real-time flow images for studying fluid flow and separation phenomena. The Micro-PIV (Particle Image Velocimetry) particle velocity measurement method employs laser illumination and high-speed imaging technology to track the positions of tracer particles at different time intervals, thereby obtaining information about the fluid velocity field and other parameters. Laser-Induced Fluorescence (LIF) utilizes laser illumination to excite fluorescent tracers in the fluid, capturing the signals with a camera or spectrometer to obtain information about fluid concentration distribution and particle transport. Chromatography techniques are employed to study the separation and diffusion of fluids in channels or pores. By measuring the degree of separation and transfer rates, information about fluid concentration distribution and separation efficiency can be obtained. These visualization experimental techniques provide quantitative analysis of flow behavior inside micro- and nano-scale channels and pores. By combining these experimental techniques, researchers can investigate the physical mechanisms of fluids at the microscale and establish related mathematical models.

Table 2. The visualization experimental methods for nanoscale EOF.

Types	Characteristic	Parameter	References
Trajectory Line Method	Contact measurement, direct and simple, lower accuracy, two-dimensional field measurement	streamline, velocity	[45]
Bright-field Observation Method	Non-contact measurement, direct observation, simple structure	flow pattern, velocity	[50]
Micro Particle Image Velocity	Non-contact measurement, high accuracy, capable of measuring both planar and three-dimensional velocity fields	velocity vectors, flow field distribution, concentration	[51]
Laser Induced Fluorescence	Non-contact measurement, high precision and resolution	velocity vectors, flow pattern, concentration, temperature	[52]
Chromatography technology	Non-contact measurement, two-dimensional field measurement	Two-dimensional flow field	[49]

With the rapid development of computer technology, simulation methods including molecular dynamics simulation (MD), Monte Carlo simulation (MC), Brownian dynamics simulation (BD), and dissipative particle dynamics simulation (DPD) have been frequently adopted to study and understand EOF mechanisms in nanoscale porous media.

The MD utilizes Newton's equations of motion to numerically solve the classical mechanics equations for molecular systems, obtaining the system's trajectory and calculating its structural characteristics and properties. This method is known for its high accuracy in computational results. Marx and Hutter [53] provided a detailed introduction to ab initio MD, including the fundamental theory, electronic structure calculations, and simulation techniques. Kim and Darve [54] investigated EOF in charged nanoscale channels with different surface roughness using equilibrium and non-equilibrium MD. Zhang et al. [55] developed a three-dimensional MD model for EOF in rough nanoscale channels to explore the influence of surface roughness on nanoscale EOF. Rezaei et al. [56] studied the EOF of an aqueous solution between parallel silicon walls using MD, considering the effects of changes in the EDL structure characteristics. Gogoi et al. [57] discussed in detail the EOF characteristics of rectangular graphene nanoscale channels with different charge configurations using non-equilibrium MD. Dehkordi et al. [58] investigated the effect of external electrostatic forces and external electric fields on the density, velocity, atomic structure, temperature, and agglomeration of Fe_3O_4 nanoparticles in copper microchannels using MD.

The MC method is a numerical computation method guided by probability and statistical theory. It has been proposed in computational simulation for discrete systems. Freund [59] conducted atomic simulations of EOF in nanoscale channels using MC to study ion distributions. Lee et al. [60] numerically investigated the effect of alternating current EOF on the performance of a biosensor unit composed of 400 nanometer wires using the MC method. Xin et al. [61], based on the improved fundamental measure theory and partial perturbation density functional theory, studied the distribution and density of ions in charged cylindrical pores with MC.

The BD can be used to simulate molecular motion and interactions, where molecules are treated as moving in a continuous medium and subject to various forces such as van der Waals forces, electrostatic forces, and solvent molecule forces. Marry et al. [62] obtained the distribution of counterions in mesoscale charged porous media using BD and Poisson-Boltzmann. Panwar and Kumar [63] employed BD to study the stretching and transport of flexible polymers in complex EOF.

The DPD is a mesoscale particle-based simulation algorithm, where a particle represents a group of atoms retaining important chemical characteristics in order to simulate the system with fewer particles instead of individual atoms. Using DPD, Duong [64] proposed a mesoscale method to describe EOF in micro/nanofluidic devices that were too large to be simulated using ab initio methods. Moshfegh and Jabbarzadeh [65] conducted explicit mesoscale simulations of EOF in nanoscale channels using an extended DPD approach. Smiatek and Schmid [66], who used DPD to simulate EOF in nanoscale channels under different surface slip conditions and ion-strength fluids, introduced appropriately tuned wall-fluid friction to systematically adjust the slip length at the channel boundaries from negative to infinitely large values.

5. Concluding remarks

EOF in porous media is an important physical phenomenon with wide-ranging potential applications in various fields. This mini-review provides an overview of the physical mechanisms and mathematical models of EOF in porous media. Up-to-date progress on EOF mechanisms in porous media has been summarized. And two subtopics, simultaneous pressure and electroosmosis-driven flow and nanoscale EOF, have been explored. The advances in these two subfields are reviewed. The present review helps understand the complex EOF mechanisms and explore potential applications of EOF in engineering and industry.

Based on the present review, the following topics may be future research directions: (1) The unique EOF properties of novel porous materials can be explored for potential applications in energy, the environment, biomedical fields, etc. (2) Attention can be directed towards the coupling of electroosmosis with other physical phenomena such as electrochemical reactions, heat conduction, and mass transfer. These multiphysical fields may help explore the role of EOF in broader domains, such as battery technology, electrochemical sensors, and microfluidic control. (3) As illustrated in this paper, EOF mechanisms for microscale and mesoscale porous media have attracted broad interest. A few mathematical models have been proposed. However, multiscale EOF phenomena may coexist in multiscale porous media where multiple physical mechanisms govern EOF. Therefore, it is necessary to develop physical models and numerical methods applicable to different scales, thereby bridging the microscopic EOF with macroscopic system performance.

Conflict of interest: The authors declare no conflict of interest.

References

1. Delgado AV, González-Caballero F, Hunter RJ, et al. Measurement and interpretation of electrokinetic phenomena. Journal of Colloid and Interface Science. 2007; 309(2): 194-224. doi: 10.1016/j.jcis.2006.12.075
2. Reuss FF. On a new effect of galvanic electricity (French). Soc. Imp. Natur. Moscou. 1809; 2: 327-337.
3. Wiedemann M. On the motion of fluids from the positive to the negative pole of the closed galvanic circuit. The London, Edinburgh, and Dublin Philosophical Magazine and Journal of Science. 1852; 4(28): 546-547. doi: 10.1080/14786445208647182
4. Quincke G. About a new type of electric current (German). Annalen der Physik. 1859; 183(5): 1-47. doi: 10.1002/andp.18591830502
5. Dorn E. On the propagation of electricity through flowing water in pipes and related phenomena (German). Annalen der Physik. 1880; 246(5): 46-77. doi: 10.1002/andp.18802460505
6. Saunders JH, Jackson MD, Pain CC. Fluid flow monitoring in oil fields using downhole measurements of electrokinetic potential. Geophysics. 2008; 73(5): E165-E180. doi: 10.1190/1.2959139
7. Millán M, Bucio-Rodríguez PY, Lobato J, et al. Strategies for powering electrokinetic soil remediation: A way to optimize performance of the environmental technology. Journal of Environmental Management. 2020; 267: 110665. doi: 10.1016/j.jenvman.2020.110665
8. Dehghan Manshadi MK, Khojasteh D, Mohammadi M, et al. Electroosmotic micropump for lab-on-a-chip biomedical applications. International Journal of Numerical Modelling: Electronic Networks, Devices and Fields. 2016; 29(5): 845-858. doi: 10.1002/jnm.2149
9. Grassia P. Viscous and electro-osmotic effects upon motion of an oil droplet through a capillary. Journal of Fluid Mechanics. 2020; 899. doi: 10.1017/jfm.2020.458
10. Yang S, Zhang H, Hu Y, et al. Experimental study on remediation of petroleum-contaminated soil by combination of freeze-thaw and electro-osmosis. Environmental Pollution. 2023; 333: 121989. doi: 10.1016/j.envpol.2023.121989
11. Jiang S, Zhang H, Chen L, et al. Numerical simulation and experimental study of the electroosmotic flow in open microfluidic chip based on super-wettability surface. Colloid and Interface Science Communications. 2021; 45: 100516. doi: 10.1016/j.colcom.2021.100516
12. Pramod K, Sen AK. Flow and Heat Transfer Analysis of an Electro-Osmotic Flow Micropump for Chip Cooling. Journal of Electronic Packaging. 2014; 136(3). doi: 10.1115/1.4027657
13. Xu H, Ding T. Influence of vacuum pressure, pH, and potential gradient on the vacuum electro-osmosis dewatering of drinking water treatment sludge. Drying Technology. 2016; 34(9): 1107-1117. doi: 10.1080/07373937.2015.1095203
14. Zhang R, Miao Q, Deng D, et al. Research progress of advanced microneedle drug delivery system and its application in biomedicine. Colloids and Surfaces B: Biointerfaces. 2023; 226: 113302. doi: 10.1016/j.colsurfb.2023.113302
15. He Q, Zhao J, Du S, et al. Reverse iontophoresis generated by porous microneedles produces an electroosmotic flow for glucose determination. Talanta. 2024; 267: 125156. doi: 10.1016/j.talanta.2023.125156
16. Shen V, Rae-Grant T, Mullenbach J, et al. Fluid Reality: High-Resolution, Untethered Haptic Gloves using Electroosmotic Pump Arrays. In: Proceedings of the 36th Annual ACM Symposium on User Interface Software and Technology; 29 October-1 November 2023; San Francisco, CA, USA. pp. 1-20. doi: 10.1145/3586183.3606771
17. Yuan Y, Abdullah MM, Sajadi SM, et al. Numerical investigation of the effect of changing the geometry of a U-shaped fuel cell channel with asymmetric gas flow and its effect on hydrogen consumption. International Journal of Hydrogen Energy. 2024; 50: 1167-1178. doi: 10.1016/j.ijhydene.2023.10.080
18. Helmholtz H. Studies on electrical interfaces (German). Annalen der Physik. 1879; 243(7): 337-382. doi: 10.1002/andp.18792430702
19. Gouy G. On the Formation of Electrical Charges at the Surface of an Electrolyte. J. physique. 1910; 9: 457-469.
20. Chapman DL. LI. A contribution to the theory of electrocapillarity. The London, Edinburgh, and Dublin Philosophical Magazine and Journal of Science. 1913; 25(148): 475-481. doi: 10.1080/14786440408634187
21. Stern A. On the counter-transference in psychoanalysis. The Psychoanalytic Review (1913-1957). 1924; 11: 166.
22. Rice CL, Whitehead R. Electrokinetic Flow in a Narrow Cylindrical Capillary. The Journal of Physical Chemistry. 1965; 69(11): 4017-4024. doi: 10.1021/j100895a062
23. Levine S, Marriott J R, Neale G, et al. Theory of electrokinetic flow in fine cylindrical capillaries at high zeta-potentials.

Journal of Colloid and Interface Science. 1975; 52(1): 136-149. doi: 10.1016/0021-9797(75)90310-0

24. Olivares J, Casadesus J, Bedmar EJ. Method for Testing Degree of Infectivity of Rhizobium meliloti Strains. Applied and Environmental Microbiology. 1980; 39(5): 967-970. doi: 10.1128/aem.39.5.967-970.1980
25. Ohshima H, Kondo T. Electrokinetic flow between two parallel plates with surface charge layers: Electro-osmosis and streaming potential. Journal of colloid and interface science. 1990; 135(2): 443-448. doi: 10.1016/0021-9797(90)90014-f
26. Mala G M, Li D, Werner C, et al. Flow characteristics of water through a microchannel between two parallel plates with electrokinetic effects. International journal of heat and fluid flow. 1997; 18(5): 489-496. doi: 10.1016/s0142-727x(97)00032-5
27. Luong DT, Sprik R. Streaming Potential and Electroosmosis Measurements to Characterize Porous Materials. ISRN Geophysics. 2013; 2013: 1-8. doi: 10.1155/2013/496352
28. Luo RH, Keh HJ. Electrokinetic flow and electric conduction of salt-free solutions in a capillary. Electrophoresis. 2020; 41(16-17): 1503-1508. doi: 10.1002/elps.202000052
29. Ning K, Wang M, Kulacki FA, et al. Electrokinetic coupling in unsteady pressure-driven flow through a porous transducer: Fractal capillary bundle model. International Journal of Heat and Mass Transfer. 2022; 195: 122764. doi: 10.1016/j.ijheatmasstransfer.2022.122764
30. Paillat T, Moreau E, Grimaud PO, et al. Electrokinetic phenomena in porous media applied to soil decontamination. IEEE Transactions on Dielectrics and Electrical Insulation. 2000; 7(5): 693-704. doi: 10.1109/94.879363
31. Wu RC, Papadopoulos KD. Electroosmotic flow through porous media: cylindrical and annular models. Colloids and Surfaces A: Physicochemical and Engineering Aspects. 2000; 161(3): 469-476. doi: 10.1016/s0927-7757(99)00209-5
32. Pascal J, Oyanader M, Arce P. Effect of capillary geometry on predicting electroosmotic volumetric flowrates in porous or fibrous media. Journal of Colloid and Interface Science. 2012; 378(1): 241-250. doi: 10.1016/j.jcis.2012.03.061
33. Bandopadhyay A, DasGupta D, Mitra SK, et al. Electro-osmotic flows through topographically complicated porous media: Role of electropermeability tensor. Physical Review E. 2013; 87(3). doi: 10.1103/physreve.87.033006
34. Liang M, Yang S, Miao T, et al. Analysis of electroosmotic characters in fractal porous media. Chemical Engineering Science. 2015; 127: 202-209. doi: 10.1016/j.ces.2015.01.030
35. Thanh LD, Jougnot D, Van Do P, et al. Electroosmotic Coupling in Porous Media, a New Model Based on a Fractal Upscaling Procedure. Transport in Porous Media. 2020; 134(1): 249-274. doi: 10.1007/s11242-020-01444-7
36. Xu C, Xu Y, Wang J, et al. A Pore-Scale Physical Model for Electric Dewatering of Municipal Sludge Based on Fractal Geometry. Journal of Environmental Engineering. 2023; 149(3). doi: 10.1061/joeedu.eeeng-7089
37. Vennela N, Bhattacharjee S, De S. Sherwood number in porous microtube due to combined pressure and electroosmotically driven flow. Chemical Engineering Science. 2011; 66(24): 6515-6524. doi: 10.1016/j.ces.2011.09.016
38. Dutta D. A numerical analysis of nanofluidic charge based separations using a combination of electrokinetic and hydrodynamic flows. Chemical Engineering Science. 2013; 93: 124-130. doi: 10.1016/j.ces.2013.01.062
39. Kou Z, Dejam M. Dispersion due to combined pressure-driven and electro-osmotic flows in a channel surrounded by a permeable porous medium. Physics of Fluids. 2019; 31(5): 056603. doi: 10.1063/1.5092199
40. Rosenfeld T, Bercovici M. Dynamic control of capillary flow in porous media by electroosmotic pumping. Lab on a Chip. 2019; 19(2): 328-334. doi: 10.1039/c8lc01077c
41. Godinez-Brizuela OE, Niasar VJ. Simultaneous pressure and electro-osmosis driven flow in charged porous media: Pore-scale effects on mixing and dispersion. Journal of Colloid and Interface Science. 2020; 561: 162-172. doi: 10.1016/j.jcis.2019.11.084
42. Terutsuki D, Miyazawa S, Takagi J, et al. Spatiotemporally Controllable Chemical Delivery Utilizing Electroosmotic Flow Generated in Combination of Anionic and Cationic Hydrogels. Advanced Functional Materials. 2023; 34(2). doi: 10.1002/adfm.202304946
43. Mondal D, Chaube M K. Study on Electroosmotic Transport of Peristaltic Flow in Microchannel. 2024; 13(1). doi:10.9790/1813-13013543
44. Kobayashi K, Iwata M, Hosoda Y, et al. Fundamental study of electroosmotic flow through perforated membrane. Journal of Chemical Engineering of Japan.1979; 12(6): 466-471. doi: 10.1252/jcej.12.466
45. Kroger T, Tomiczek A, Wahl F. Towards On-Line Trajectory Computation. In: Proceedings of the 2006 IEEE/RSJ International Conference on Intelligent Robots and Systems; 9-15 October 2006; Beijing, China. pp. 736-741. doi: 10.1109/iros.2006.282622

46. Maksimenko A, Ando M, Sugiyama H, et al. A Test of an X-Ray Quatrochrome Interferometer for Simultaneous Observation of Images Due to Dark- and Bright-Field, Phase-Interference and Absorption Contrasts. Japanese Journal of Applied Physics. 2003; 42(Part 2, No.9A/B): L1096-L1099. doi: 10.1143/jjap.42.l1096
47. Lindken R, Rossi M, Große S, et al. Micro-Particle Image Velocimetry (µPIV): Recent developments, applications, and guidelines. Lab on a Chip. 2009; 9(17): 2551. doi: 10.1039/b906558j
48. Van de Nesse RJ, Velthorst NH, Brinkman UAT, et al. Laser-induced fluorescence detection of native-fluorescent analytes in column liquid chromatography, a critical evaluation. Journal of Chromatography A. 1995; 704(1): 1-25. doi: 10.1016/0021-9673(95)00053-p
49. Šesták J, Moravcová D, Kahle V. Instrument platforms for nano liquid chromatography. Journal of Chromatography A. 2015; 1421: 2-17. doi: 10.1016/j.chroma.2015.07.090
50. Chen J, Li H, Xie H, et al. A novel method combining aptamer-Ag10NPs based microfluidic biochip with bright field imaging for detection of KPC-2-expressing bacteria. Analytica Chimica Acta. 2020; 1132: 20-27. doi: 10.1016/j.aca.2020.07.061
51. Wereley ST, Meinhart CD. Recent Advances in Micro-Particle Image Velocimetry. Annual Review of Fluid Mechanics. 2010; 42(1): 557-576. doi: 10.1146/annurev-fluid-121108-145427
52. Murniati E, Gross D, Herlina H, et al. Oxygen imaging at the sediment-water interface using lifetime-based laser induced fluorescence (τLIF) of nano-sized particles. Limnology and Oceanography: Methods. 2016; 14(8): 506-517. doi: 10.1002/lom3.10108
53. Marx D, Hutter J. Ab initio molecular dynamics: Theory and implementation. Modern methods and algorithms of quantum chemistry. 2000; 1(301-449): 141.
54. Kim D, Darve E. Molecular dynamics simulation of electro-osmotic flows in rough wall nanochannels. Physical Review E. 2006; 73(5). doi: 10.1103/physreve.73.051203
55. Zhang C, Lu P, Chen Y. Molecular dynamics simulation of electroosmotic flow in rough nanochannels. International Communications in Heat and Mass Transfer. 2014; 59: 101-105. doi: 10.1016/j.icheatmasstransfer.2014.10.024
56. Rezaei M, Azimian AR, Semiromi DT. The surface charge density effect on the electro-osmotic flow in a nanochannel: a molecular dynamics study. Heat and Mass Transfer. 2014; 51(5): 661-670. doi: 10.1007/s00231-014-1441-y
57. Gogoi A, Reddy KA, Mondal PK. Electro-osmotic flow through nanochannel with different surface charge configurations: A molecular dynamics simulation study. Physics of Fluids. 2021; 33(9). doi: 10.1063/5.0062031
58. Dehkordi RB, Toghraie D, Hashemian M, et al. The effects of external force and electrical field on the agglomeration of Fe_3O_4 nanoparticles in electroosmotic flows in microchannels using molecular dynamics simulation. International Communications in Heat and Mass Transfer. 2021; 122: 105182. doi: 10.1016/j.icheatmasstransfer.2021.105182
59. Freund JB. Electro-osmosis in a nanometer-scale channel studied by atomistic simulation. The Journal of Chemical Physics. 2002; 116(5): 2194-2200. doi: 10.1063/1.1431543
60. Lee CA, Teramoto A, Watanabe H. Monte Carlo Simulation of Nanowires Array Biosensor with AC Electroosmosis. IEEE Transactions on Electron Devices. 2018; 65(5): 1932-1938. doi: 10.1109/ted.2018.2812783
61. Xin Y, Zheng YX, Yu YX. Density functional theory study on ion adsorption and electroosmotic flow in a membrane with charged cylindrical pores. Molecular Physics. 2015; 114(16-17): 2328-2336. doi: 10.1080/00268976.2015.1090637
62. Marry V, Dufrêche J F, Jardat M, et al. Equilibrium and electrokinetic phenomena in charged porous media from microscopic and mesoscopic models: electro-osmosis in montmorillonite. Molecular Physics. 2003; 101(20): 3111-3119. doi: 10.1080/00268970310001626432
63. Panwar AS, Kumar S. Brownian dynamics simulations of polymer stretching and transport in a complex electroosmotic flow. The Journal of Chemical Physics. 2003; 118(2): 925-936. doi: 10.1063/1.1523912
64. Duong-Hong D, Wang JS, Liu GR, et al. Dissipative particle dynamics simulations of electroosmotic flow in nano-fluidic devices. Microfluidics and Nanofluidics. 2007; 4(3): 219-225. doi: 10.1007/s10404-007-0170-7
65. Moshfegh A, Jabbarzadeh A. Fully explicit dissipative particle dynamics simulation of electroosmotic flow in nanochannels. Microfluidics and Nanofluidics. 2016; 20(4). doi: 10.1007/s10404-016-1733-2
66. Smiatek J, Schmid F. Mesoscopic simulations of electroosmotic flow and electrophoresis in nanochannels. Computer Physics Communications. 2011; 182(9): 1941-1944. doi: 10.1016/j.cpc.2010.11.021

Academic Publishing Pte. Ltd.

Add: 73 Upper Paya Lebar Road #07-02B-01 Centro Bianco Singapore 534818
Tel: +65 83184869
E-mail: editorial_office@acad-pub.com
Web: http://ojs.acad-pub.com/